Advances in Electric Drive Vehicle Modeling

with Subsequent Experimentation and Analysis

By

Austin Joseph Hausmann

Submitted to the graduate degree program in Mechanical Engineering and the Graduate Faculty of the University of Kansas in partial fulfillment of the requirements for the degree of Master of Science.

Chair: Dr. Christopher Depcik

Dr. Ronald L. Dougherty

Dr. Terry Faddis

Defended: July 24, 2012

The Thesis Committee for Austin Hausmann certifies that this is the approved version of the following thesis:

Advances in Electric Drive Vehicle Modeling

with Subsequent Experimentation and Analysis

By

Austin Joseph Hausmann

Chair: Dr. Christopher Depcik

Date approved: July 26, 2012

Abstract

A combination of stricter emissions regulatory standards and rising oil prices is leading many automotive manufacturers to explore alternative energy vehicles. In an effort to achieve zero tail pipe emissions, many of these manufacturers are investigating electric drive vehicle technology. In an effort to provide University of Kansas students and researchers with a stand-alone tool for predicting electric vehicle performance, this work covers the development and validation of various models and techniques.

Chapter 2 investigates the practicality of vehicle coast down testing as a suitable replacement to moving floor wind tunnel experimentation. The recent implementation of full-scale moving floor wind tunnels is forcing a re-estimation of previous coefficient of drag determinations. Moreover, these wind tunnels are relatively expensive to build and operate and may not capture concepts such as linear and quadratic velocity dependency along with the influence of tire pressure on rolling resistance. The testing method explained here improves the accuracy of the fundamental vehicle modeling equations while remaining relatively affordable.

The third chapter outlines various models used to predict battery capacity. The authors investigate the effectiveness of Peukert's Law and its application in lithium-based batteries. The work then presents the various effects of battery temperature on capacity and outlines previous work in the field. This paper then expands upon Peukert's equation in order to include both variable current and temperature effects. The method proposed captures these requirements based on a relative maximum capacity criterion. Experimental methods presented in the paper provide an economical testing procedure capable of producing the required coefficients in order to build a high-

level, yet accurate state of charge prediction model. Moreover, this work utilizes automotive grade lithium-based batteries for realistic outcomes in the electrified vehicle realm.

The fourth chapter describes an advanced numerical model for computing vehicle energy usage performance. This work demonstrates the physical and mathematical theories involved, while building on the principles of Newton's second law of motion. Moreover, this chapter covers the equipment, software, and processes necessary for collecting the required data. Furthermore, a real world, on-road driving cycle provides for a quantification of accuracy. Multiple University of Kansas student project vehicles are then studied using parametric studies applicable to the operating requirements of the vehicles. Further investigation demonstrates the accuracy and trends associated with the advanced models presented in Chapters 2 and 3.

Lastly, chapter 5 investigates the design and building of a graphical user interface (GUI) for controlling the models created in the previous three chapters. The chapter continues to outline the creation of a stand-alone GUI as well as instructions for implementation, usage, and data analysis.

Words: 427

Table of Contents

Table of Figures

1.1 Introduction

CHAPTER 2: A Cost-Effective Alternative to Moving Floor Wind Tunnels in Order to Calculate Rolling Resistance and Aerodynamic Drag Coefficients

CHAPTER 3: Expanding the Peukert Equation for Battery Capacity Modeling Through Inclusion of a Temperature Dependency

Table of Tables

1.1 Introduction

CHAPTER 2: A cost-effective alternative to moving floor wind tunnels in order to calculate rolling resistance and aerodynamic drag coefficients

CHAPTER 3: Expanding the Peukert Equation for Battery Capacity Modeling Through Inclusion of a Temperature Dependency

CHAPTER 4: An Advanced Electric Vehicle Duty Cycle Simulation Model Derived from Newton's Second Law of Motion

1. Introduction

Recent legislation by the Environmental Protection Agency (EPA), California Air Resources Board (CARB), and other emissions regulatory commissions has required automotive manufacturers to reduce exhaust emissions to miniscule levels. Meeting these requirements is becoming increasingly difficult for traditional internal combustion engine (ICE) technology. The increased pollution concerns coupled with ever-rising oil prices has led many automotive manufacturers to investigate the use of electric drive technology. Electric drive vehicles are any vehicles that "*use one or more electric motors or traction motors for propulsion*" [1]. Many consumers relate electric vehicles (EV) with the typical battery electric vehicle (BEV); however, electric drive vehicles also include hybrid electric vehicles (HEV), plug-in hybrid electric vehicles (PHEV), extended-range electric vehicles (EREV), and fuel cell electric vehicles (FCEV) [2]. Each of these platforms provides a different level of electrification with its own advantages and disadvantages, which will be covered later. For full-scale deployment of electric drive vehicles, many key vehicle logistics parameters require investigation.

Electric drive motors typically possess much higher effective conversion efficiencies (70-90%) than traditional ICEs (30-45%) while offering zero tailpipe emissions [3]. However, the limited range of such vehicles is a concern for many drivers. While a BEV offers a pure electric vehicle powertrain platform with batteries as a storage medium and 100% of the drive power being delivered through an electrical generation source, many intermediate steps between ICE vehicles and BEVs exist. Most of these options aim to overcome current anxieties. The most subtle step, which avoids this issue, is the EREV. This powertrain operates as a BEV for certain, limited

distances and then switches over to a traditional ICE powertrain for a range more typical of a traditional vehicle. The automotive field sees this hybrid configuration as a stepping-stone between current ICE vehicles and BEVs while electric drive and battery technology improves. This is because it provides the benefits of electric drive without the range issues.

The linkage of the engine and the motor in these and other electrified vehicles occurs in either a series or parallel hybrid configuration. In a series hybrid, there is no direct physical coupling of the ICE to the drivetrain. Instead, the ICE merely recharges the energy storage mechanism that powers the electric drive. A parallel hybrid configuration utilizes both electric drive technology and an ICE to power the drivetrain of the vehicle. Complex hybrids such as the Chevrolet Volt can operate in multiple configurations. Figure 1 illustrates many different options that bridge the gap between ICE vehicles and BEVs.

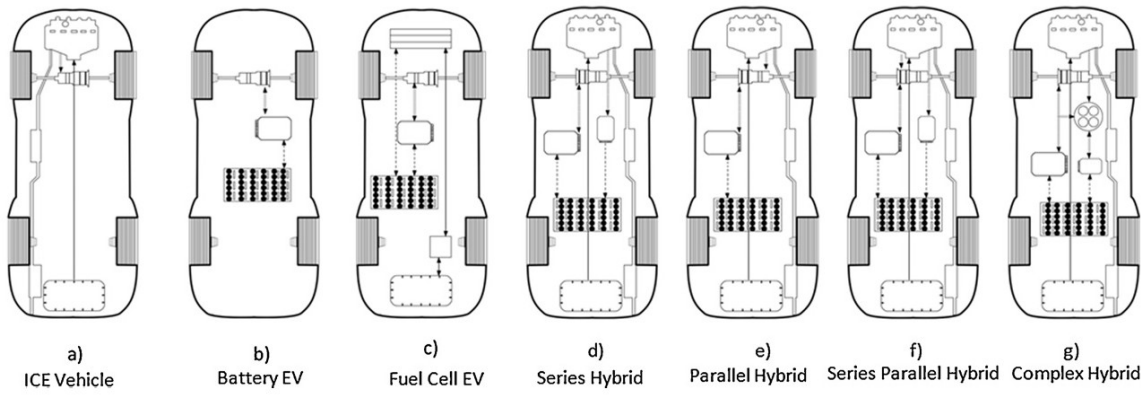

Figure 1: Typical vehicle powertrain options [3].

Another alternative to BEVs is through use of a fuel cell as the onboard energy or power source. FCEVs operate with many of the same features as BEVs (pure electric drive, electronic controllers, auxiliary inverters, etc…); however, the energy source is

considerably different. The most popular fuel cell system is based on hydrogen fuel storage which is converted to electricity in order to power an electric traction motor. While fuel cells provide a higher energy density and ultimately higher range capacity than battery based energy storage, the price, infrastructure, and safety concerns currently outweigh the benefits resulting in consideration of FCEVs as the most ambitious of the alternative powertrain options [3].

The most common reluctance towards the purchasing of an electric vehicle is the limited range [3-5]. While many hybrid configurations can bridge the gap and provide additional range, the ultimate goal is a sustainable fuel source with zero tailpipe emissions. The primary disadvantage to range is the bulky and expensive energy storage source required to provide a range equivalent to that of an ICE vehicle [4]. While actual numbers vary based on the study, initial range requirement studies are promising. For example, in 2006, Denholm and Short determined that 75% of daily driving is less than 60 miles [4]. In the following year, Gondor found that 95% of daily driving in the United States is less than 100 miles [4]. Both of these figures are well within the feasible range of current electric vehicles; however, the concern is typically not an issue in day-to-day driving habits, but more a result of the occasional long distance trips that are required. The long range traveling issue has currently available solutions such as car rental and multiple vehicle ownership. As of 2001, the average household owned 1.9 vehicles [4]. Nearly all households with multiple vehicles could easily implement a limited range electric vehicle into their current driving habits with little or no disruption as long as the family or individual maintains a second vehicle with extended range. Pearre et al. found that that if drivers were willing to make alternate

driving arrangements on a mere six days per year, 32% of drivers would be otherwise unaffected by the limited range aspects of solely owning an electric vehicle [4].

With range and price at the top of the list of concerns for electric vehicles, the primary challenge and limiting factor for electric drive vehicles has historically been the price and size of energy storage [6]. Nearly all electric drive vehicles use a battery pack to some degree in order to store the energy required for the electric drive motor. The size and design of the pack varies greatly based on the powertrain of the vehicle. In BEVs, the battery pack acts as the sole energy source onboard the vehicle. In a series-hybrid, the battery pack not only acts as energy storage medium, but also as a buffer between the onboard generator and the electric drive. As a comparison, traditional ICE vehicles possess roughly 700 watt-hours of battery energy in the 12-volt system and the typical consumer battery electric vehicle utilizes around 25,000 watt-hours of battery energy [7]. It quickly becomes obvious that the volume and weight of the battery become a significant factor in the vehicle design.

The first BEVs were powered by lead-acid battery modules [8]. While lead-acid batteries have a long-standing history of being forgiving and economical, they are among the heaviest of all batteries (35 watt-hours per kilogram) and are nearly impractical for large scale electric vehicle applications. In the early days of electric vehicle commercialization, nickel-metal-hydride batteries became desirable for their improved energy density characteristics (75 watt-hours per kilogram) over lead-acid cells [3]. However, nickel-based batteries often suffer from a “memory” function that can quickly degrade the working capacity of the battery pack if usage occurs before being fully charged. Most recently, lithium battery technology has been at the forefront

of electric vehicle energy storage and appears to be the most viable option moving forward. While lithium battery cells are more volatile than traditional battery designs, they provide a significantly larger energy density (180 watt-hours per kilogram) than most other battery technologies. The largest concern with lithium based technology is the cost (~$1000/kWh versus ~$150/kWh for lead-acid) as it is the most expensive of the readily available rechargeable battery cells [3]. However, lithium battery technology has only been around for about 20 years (as opposed to the lead acid battery which was invented in 1859), and many experts predict the cost will decline rapidly and the lithium battery to become the least expensive of the rechargeable batteries by 2025 [3, 7]. Other concerns revolve around the availability of lithium. While lithium scarcity should be a concern over full-scale deployment of large electric vehicle packs, it is worth noting that lithium batteries are typically less than one-percent lithium by weight and possess desirable recyclability characteristics [6].

While battery technology has been proven to an extent in automobiles since the early 1900's [8], fuel cell technology has always been seen as a future possibility for vehicle energy storage. With more desirable discharge times (up to 300 hours versus 12 hours), life cycles (10,000 versus 3,000), and energy densities (up to 3,000 watt-hours per kg), fuel cell technology offers many advantages over battery energy storage [3]. While hydrogen possesses an extremely high energy density by weight, volumetric energy efficiency is a prime concern. Hydrogen is nearly five times denser than gasoline by weight, but 3,000 times less dense than gasoline by volume, which presents immediate storage concerns. To achieve a feasible storage factor, hydrogen must be highly compressed, sometimes exceeding 10,000 psi [3]. It quickly becomes obvious

that on-vehicle hydrogen storage not only has spatial concerns, but elevated safety concerns as well that must be well developed and tested before full-deployment.

While electric vehicle onboard energy sources are the primary concern with electric drive vehicles, the energy distribution lines are also at the forefront of the alternative energy vehicle discussion. In 2008, President Obama set a goal of having one million PHEVs on the road in the United States by 2015 [9]. While the existing grid does provide for a quicker implementation than the development of an entire infrastructure (such as natural gas or fuel cell vehicles), the potential for localized brown-outs due to this large number of PHEVs being connected to the grid has been a primary concern of utility companies for many years. The energy grid in the United States is relatively aged and the added demand from millions of electric vehicles will cause an unprecedented strain on local infrastructure [10, 11]. Studies have shown that much of this strain can be reduced or completely eliminated through the use of smart metering and smart grid technology as well as intelligently choosing charge times [11-13]. A smart grid would allow electric companies to monitor the current grid loads and the number of electrified vehicles plugged into the grid while not only charging these vehicles during non-peak hours, but also using the electricity remaining in the battery packs to shave peak loads (known as vehicle-to-grid technology). This not only provides a benefit to the electric companies, but the vehicle owners can also benefit from the selling the energy back to the utility company at increased rates. While the peak-rate times are of the largest concern, alternatives exist by taking advantage of opportunistic charging. Weiller estimates that 4% of all the vehicles driven in the United States are on the road at any given time [14]. This leaves a significant amount of time

available for opportunistic charging to maintain vehicle battery levels as high as possible during off-peak hours and reduce on-peak charging.

While the challenges facing electrified vehicles definitely appear surmountable, the road to fuel cells and hydrogen distribution is not as obvious. Hydrogen currently requires transportation via tanker in gaseous form which presents large volumetric concerns, or via compressed liquid which requires cryogenic storage to maintain the -253°C temperature required [3]. Once transported to a distribution site, on-site storage and refueling stations would require construction to allow for the transfer of the hydrogen from the tanker vehicles to the consumer vehicles. It is estimated that nearly 19,000 additional hydrogen refueling stations would be required to support wide scale usage of hydrogen fuel cell vehicles [3]. These distribution concerns coupled with on-vehicle storage concerns have led to the assumption that fuel cell technology is still very much a work in progress.

Many of the storage issues associated with battery energy prices and sizing are avoidable to a certain extent if charge times improve. Numerous consumers worry about the situation in which the vehicle is approaching a minimum state of charge and their route is not yet complete, known more commonly as range anxiety. For existing ICE vehicles, this problem is trivial, as refueling often takes no longer than five to ten minutes. With the technological status of electrified vehicles, it can take many hours to recharge fully the battery pack. For most drivers this is unacceptable, requiring manufacturers to size the battery pack to be large enough to complete the longest of the drivers routes. Experts have set an ultimate target time of ten minutes to recharge the battery from an empty state and have set a variety of acceptable charge times and

conditions for everyday situations [10]. A variety of rapid charging levels and target charging times based on certain state of charge (SOC) are available as seen in Table 1.

Table 1: Electric vehicle target charging levels [10].

Level of Charge	Charger Power Level [kW]		
	Heavy Duty	SUV/Sedan	Small Sedan
1. Quick Charge, 60 minutes, 70% SOC	75	35	20
2. Rapid Charge, 15 minutes, 60% SOC	250	125	60
3. Fast Charge, 10 minutes, 100% SOC	500	250	125
Plug-In Hybrid, 30 minutes	40	20	10

Each of these charging levels has an associated infrastructure requirement. Level one charging, which many consumers will possess in their homes requires a regular 120 VAC wall outlet. Level two charging is possible with 120 VAC, although 240 VAC provides for much lower current draw. Level three charging will require extensive power delivery capabilities and is only considered possible through a 600 volt 550 amp direct current system [10]. While level three “Fast Charge” could alleviate many of the range anxiety concerns of drivers, the cost and availability of these stations remains a concern. These faster charge times will also introduce life cycle concerns for the battery pack. As the charging power and frequency of charging increases, the operation life cycles of the battery pack will decrease. This will become a balancing act for consumers, as the battery pack is often the most expensive component of an electrified vehicle [10].

Electric drive vehicles provide a powerplant and driveline conversion efficiency that is typically twice that of the traditional internal combustion engine drivetrain. While this advantage is clear, there are numerous concerns with wide scale implementation of electric vehicles, many of which relate directly to the energy storage capabilities and cost of such vehicles. A variety of aspects relating to electric drive vehicles worry consumers and have effectively slowed adoption rates; however, nearly all of these

obstacles have clear, practical, and relatively short-term solutions. The largest obstacle is likely convincing consumers to change their perceptions and habits to adapt to a new age of vehicles. The public is often reluctant to change and Americans' dependence on personal vehicles for transportation is extremely high. Electric drive vehicles will obviously not work for everyone, but they do have their place and can provide significant benefits to their users and the environment.

2. Past Efforts in Electrified Vehicles at the University of Kansas

In 2008, Assistant Professor Dr. Christopher Depcik started the EcoHawks senior design project in an effort to bring a sustainable approach for the automotive industry to the University of Kansas [15]. By focusing on the five core principles of sustainability (energy, economy, education, environment, and ethics), a holistic approach is applied to the automotive design problem. This program has resulted in the construction of two unique student designed electric drive vehicles. The first of which, a 1974 Volkswagen Super Beetle has been converted to a plug-in series hybrid that can be recharged using a generator operating on 100% biodiesel. This vehicle has been road worthy since the spring of 2010 and provides a medium for ongoing research and efficiency optimization. The second vehicle is a 1997 GMC Jimmy SUV in the process of conversion to a modern BEV, for the University of Kansas Libraries in order to aid in daily deliveries around campus.

Through the design process of these two vehicles, a significant requirement exists to predict the overall performance of the vehicles. With the lack of a standalone model to estimate these performance characteristics, design work can often prove tedious. To improve on past efforts, as well as provide a design tool, requires

investigation of previous work in the field. In an effort to understand the holistic problem, the work covers vehicle dynamics, battery capacity modeling, and overall on-road vehicle performance with a focus on vehicle powertrain.

3. Thesis Focus

A vehicle dynamics literature review indicates the importance of modeling vehicle drag and rolling resistance values. In the absence of a rolling floor wind tunnel, on-road coast down testing often proves as a viable replacement to gather the necessary data set. While many authors outline this process, most neglect advanced modeling terms such as linear and quadratic velocity dependency, the influence of tire pressure on rolling resistance along with a dynamic coefficient of aerodynamic drag. Of the authors that accomplish this task [16-19], the results are a product of controlled laboratory testing as opposed to physical road testing. These methods can often prove too costly or difficult to utilize. As a result, Chapter 2 contains the findings associated with the development of an advanced on-road coastdown method and model.

As previously mentioned, the vehicle battery pack tends to be one of the most important powertrain components of electric drive vehicles. The most accurate battery models involve the of electro-chemical modeling to predict battery performance. While these methods provide a high level of accuracy, they are also difficult to develop and calibrate [20]. Based on a relative maximum capacity criterion, Chapter 3 presents a battery state of charge model capturing both current and temperature effects on battery capacity. The authors also demonstrate a straightforward testing method for capturing the required dataset. By retaining a small dataset requirement, the model lends itself to onboard vehicle diagnostic and state of charge calculation routines.

To provide a method for calculating various on-road vehicle performance criteria, the presentation of a vehicle dynamics model structured around Newton's Second Law of motion occurs in Chapter 4. The basis for the model revolves around requiring a minimal data set from the vehicle route. This methodology allows the user to focus on the importance of the vehicular data set. The model improves upon previous work through inclusion of the two models in the preceding chapters. The chapter outlines the accuracy of the model as well as parametric studies using the two previously mentioned vehicles.

Chapter 5 focuses on improving usability of the model by presenting the creation of a graphical user interface (GUI) for the model. The chapter begins by demonstrating the fundamentals of GUI creation using MATLAB. The authors then present the final design along with instructions for implementation, usage, and data analysis.

As some of the work mentioned here is intended to be submitted as journal or conference papers, the formatting for each chapter is written accordingly with all authors mentioned.

References

1. Faiz, A., C.S. Weaver, and M.P. Walsh, *Air pollution from motor vehicles: standards and technologies for controlling emissions* 1996: World Bank Publications.
2. *Electric Drive Transportation Association*. 2012; Available from: http://www.electricdrive.org/.
3. Pollet, B.G., I. Staffell, and J.L. Shang, *Current status of hybrid, battery and fuel cell electric vehicles: From electrochemistry to market prospects.* Electrochimica Acta, (0).
4. Pearre, N.S., et al., *Electric vehicles: How much range is required for a day's driving?* Transportation Research Part C: Emerging Technologies, 2011.
5. Graham-Rowe, E., et al., *Mainstream consumers driving plug-in battery-electric and plug-in hybrid electric cars: A qualitative analysis of responses and evaluations.* Transportation Research Part A: Policy and Practice, 2012. **46**(1): p. 140-153.
6. Anderson, D.L., *An Evaluation of current and future costs for lithium-ion batteries for use in electrified vehicle powertrains*, 2009, Duke University.
7. Buchmann, I., *Battery university*, 2003, July.
8. Powell, B., K. Bailey, and S. Cikanek, *Dynamic modeling and control of hybrid electric vehicle powertrain systems.* Control Systems Magazine, IEEE, 1998. **18**(5): p. 17-33.
9. Obama, B., *Remarks by the President in State of the Union Address.* January, 2011. **27**: p. 200.
10. Botsford, C. and A. Szczepanek, *Fast charging vs. slow charging: Pros and cons for the new age of electric vehicles.* EVS24, Stavanger, Norway, 2009.
11. Kintner-Meyer, M., K. Schneider, and R. Pratt, *Impacts assessment of plug-in hybrid vehicles on electric utilities and regional US power grids, Part 1: Technical analysis.* Pacific Northwest National Laboratory (a), 2007.
12. Ipakchi, A. and F. Albuyeh, *Grid of the future.* Power and Energy Magazine, IEEE, 2009. **7**(2): p. 52-62.
13. Clement-Nyns, K., E. Haesen, and J. Driesen, *The impact of charging plug-in hybrid electric vehicles on a residential distribution grid.* Power Systems, IEEE Transactions on, 2010. **25**(1): p. 371-380.
14. Weiller, C., *Plug-in hybrid electric vehicle impacts on hourly electricity demand in the United States.* Energy Policy, 2011.
15. *KU EcoHawks: A Sustainable Approach to Automobiles and Energy Infrastructure* 2012; Available from: http://groups.ku.edu/~ecohawks/.
16. Swift, A., *Calculation of vehicle aerodynamic drag coefficients from velocity fitting of coastdown data.* Journal of Wind Engineering and Industrial Aerodynamics, 1991. **37**(2): p. 167-185.
17. Lucas, G. and A. Emtage, *A new look at the analysis of coast down test results.* ARCHIVE: Proceedings of the Institution of Mechanical Engineers, Part D: Transport Engineering 1984-1988 (vols 198-202), 1987. **201**(24): p. 91-97.
18. Grover, P., *Modeling of rolling resistance test data.* 1998.

19. Grover, P.S. and S.H. Bordelon, *New Parameters for Comparing Tire Rolling Resistance.* 1999.
20. Lahiri, K., et al. *Battery-driven system design: A new frontier in low power design*. in *Design Automation Conference, 15th International Conference on VLSI Design* 2002. IEEE Computer Society.

Chapter 2: A Cost-Effective Alternative to Moving Floor Wind Tunnels in Order to Calculate Rolling Resistance and Aerodynamic Drag Coefficients

Austin Hausmann[1] and Christopher Depcik

Department of Mechanical Engineering - University of Kansas, Lawrence, Kansas (United States)

Abstract

This study investigates the practicality of vehicle coast down testing as a suitable replacement to moving floor wind tunnel experimentation. The recent implementation of full-scale moving floor wind tunnels is forcing a re-estimation of previous coefficient of drag determinations. Moreover, these wind tunnels are relatively expensive to build and operate and may not capture concepts such as linear and quadratic velocity dependency along with the influence of tire pressure on rolling resistance. As a result, the method elucidated here improves the accuracy of the fundamental vehicle modeling equations while remaining relatively affordable. The trends produced by incorporating on road test data into the model fit the values indicated by laboratory tests. This research chose equipment based on a balance between affordability and accuracy while illustrating that higher resolution frequency equipment would further enhance the model accuracy.

Keywords: aerodynamic drag; rolling resistance; wind tunnel; coast down testing; vehicle modeling;

Keywords: 136

[1] Corresponding author. Tel.: +1 785 840 7693; E-mail address: hausmann@ku.edu
1501 W. 15th St. 3138 Learned Hall Lawrence, KS 66045 USA

Nomenclature

Variable	Description	Units
a_d, k_d	Unitless aerodynamic drag coefficients	[-]
b_d	Linear velocity aerodynamic drag coefficient	[m/s]
a_L	Linear velocity aerodynamic lift coefficient	[1/(m/s)]
b_L, k_L	Unitless aerodynamic lift coefficients	[-]
c_L	Linear velocity aerodynamic lift coefficient	[m/s]
$C_{L,yaw}$	Aerodynamic yaw lift coefficient	[-]
A_f	Vehicle frontal area	[m^2]
A_P	Vehicle planform area	[m^2]
a_{rr}	Static rolling resistance coefficient	[N]
b_{rr}	Linear velocity rolling resistance coefficient	[N/(m/s)]
d_{rr}	Quadratic velocity rolling resistance coefficient	[N/(m^2/s^2)]
C_D	Standard aerodynamic drag coefficient	[-]
$C_{D,yaw}$	Aerodynamic yaw drag coefficient	[-]
C_L	Standard aerodynamic lift coefficient	[-]
F_D	Aerodynamic drag force	[N]
F'_D	Pseudo-normalized drag force	[m^2/s^2]
F_{GR}	Force of road gradation	[N]
F_L	Aerodynamic lift force	[N]
F'_L	Pseudo-normalized lift force	[m^2/s^2]
F_{LA}	Linear acceleration force	[N]
F_{RR}	Rolling resistance force	[N]
F_{TE}	Total tractive effort force	[N]
g	Acceleration due to gravity	[m/s^2]
m	Vehicle mass	[kg]
P_{ref}	Reference tire pressure	[kPa]
p_{tire}	Tire pressure	[kPa]
R	Model velocity error residual	[m/s]
t	Time	[s]
V	Absolute vehicle velocity	[m/s]
V_{eff}	Relative vehicle velocity	[m/s]
V_{wind}	Velocity of wind during testing	[m/s]
Z	Vertical vehicle load	[N]
Z_{ref}	Reference vertical vehicle load	[N]
α, β	Rolling resistance exponents	[-]
μ_{RR}	Standard coefficient of rolling resistance	[-]
ψ	Yaw angle	[deg]
φ	Wind angle relative to direction of motion	[deg]
ρ	Density of air	[kg/m^3]
θ	Road gradation angle	[deg]

1. Introduction

Many forces act on a vehicle during operation with its total tractive force (F_{TE}) a sum of the linear acceleration (F_{LA}), aerodynamic drag (F_D), rolling resistance (F_{RR}) and road gradation forces (F_{GR}):

$$F_{TE} = F_{LA} + F_D + F_{RR} + F_{GR} \quad (1)$$

where linear acceleration acts to propel the vehicle forward and the other forces work in opposition to vehicle motion. In this Eqn. 1, the two key forces of interest influenced by vehicle design and associated components are the aerodynamic drag and rolling resistance. One method for measuring these forces for a particular automobile is to record vehicle velocity verses time data during a coast down experiment [1-5].

A coast down test is an experiment in which an operator drives a vehicle at a high speed and then coasts to a near stop while the drive components are disengaged. Since these drive components are uncoupled, it is reasonable to neglect the linear acceleration force. Moreover, researchers often neglect the efficiency of these elements along with losses such as transmission friction and brake drag due to their relatively small magnitudes and measurement difficulty [2]. Furthermore, drive component drag forces are vehicle dependent and require measurement for each test vehicle. While estimation of these items could occur, the amount of induced error associated with such approximations is difficult to quantify.

In the absence of a perfectly horizontal road, the analysis must consider elevation through the road gradation force. In addition, wind direction and magnitude can have an impact on the coast down experiment through the drag force. While its effect is minimal at lower speeds, it can become a significant factor at higher speeds (e.g., highway driving) due to the quadratic velocity component dependency in the drag

force, discussed later. Ideally, measurement of vehicle elevation and wind velocity occurs at the same intervals as the velocity and time of the vehicle under study.

Of importance for this paper, vehicular modeling efforts often neglect concepts such as linear and quadratic velocity dependency, the influence of tire pressure on rolling resistance along with a dynamic coefficient of aerodynamic drag in the force balance [6]. While some researchers do incorporate these effects [2, 4, 5, 7], they often do not include all of previously mentioned concepts at the same time; e.g., enhanced rolling resistance but simple coefficient of drag. Another concern with these models is the lack of physical field validation. While the models may perform well in a laboratory environment, the lack of true road testing hinders the application of these models for real world scenarios. Achieving the desired "on road" values in a controlled setting requires the use of a large moving floor wind tunnel. For example, Krajnović and Davidson find that the motion of the floor reduces aerodynamic drag by 8% for a full scale automobile [8]. Geropp and Odenthal arrive at similar results using a one-fifth scale two-dimensional body [9] and Fago discovers that road simulation via moving floor wind tunnels reduces the aerodynamic drag coefficient by as much as 40% at various velocities in comparison to a stationary floor [10].

However, full size moving floor wind tunnels are relatively uncommon and testing is expensive. Moreover, these testing methods can prove to be cost prohibitive for smaller automotive manufacturers, college and experimental car teams such as those that compete in Formula SAE, Xprize Foundation, and solar challenge events. Even stationary floor wind tunnel testing can be too expensive for some situations. In comparison, the primary expense of a coast down test is a function of the data

acquisition equipment. Unlike the cost of a wind tunnel where companies charge based on an hourly rate, once the researcher purchases the needed data acquisition equipment, they can perform numerous coast down tests for multiple vehicles or testing environments with minimal additional expense. Given the advancement in vehicle data logging technology, Global Positioning Systems (GPS), and the addition of the On-Board Diagnostic (OBD) ports, commercially available data logging and acquisition equipment has become relatively inexpensive. The data collection equipment for this analysis was purchased for less than the cost of two hours of local stationary wind tunnel testing (less than 500 USD). In the following sections, this paper first describes all pertinent model parameters followed by its calibration via vehicle data logging equipment and a coast down test.

2. Model and Data Collection

In order to understand vehicle dynamics, the basic fundamental methods are first considered. Then, the authors improve upon these methods to determine the data set required from testing. The following sections present the proposed model and data collection methods.

2.1 Theoretical Vehicle Dynamics Model

The first item in the force balance of Eqn. (1) to consider during a coast down test is the drag force on a moving automobile. Typical fluid mechanics books illustrate that this equation often uses a constant drag coefficient (C_D) [11]:

$$F_D = \frac{1}{2}\rho A_f C_D V^2 \quad (2)$$

where ρ is the density of the medium, A_f is the frontal area and V is the velocity of the vehicle. While this generally accepted equation works well for a principal understanding

of vehicle dynamics, it neglects key aspects necessary for a high-level model. In a real world setting, unlike a wind tunnel that simulates vehicle motion in a stagnant environment, wind and pitch of the vehicle can act to hinder or help the resultant drag force. As illustrated in Figure 1, the effective velocity of a vehicle (V_{eff}) is a function of its actual velocity (V), the wind speed (V_{wind}), the angle of wind relative to the direction of motion (φ) and the yaw (ψ) of the vehicle:

$V_{eff}\cos\psi = V - V_{wind}\cos\varphi$	(3)

Note that the wind speed is positive if assisting and negative if hindering as the figure shows. Proper consideration of the yaw angle must account for the direction of the wind effects. As a result, measurement of the yaw angle is according to the relative angle of the wind in reference to the heading of the vehicle.

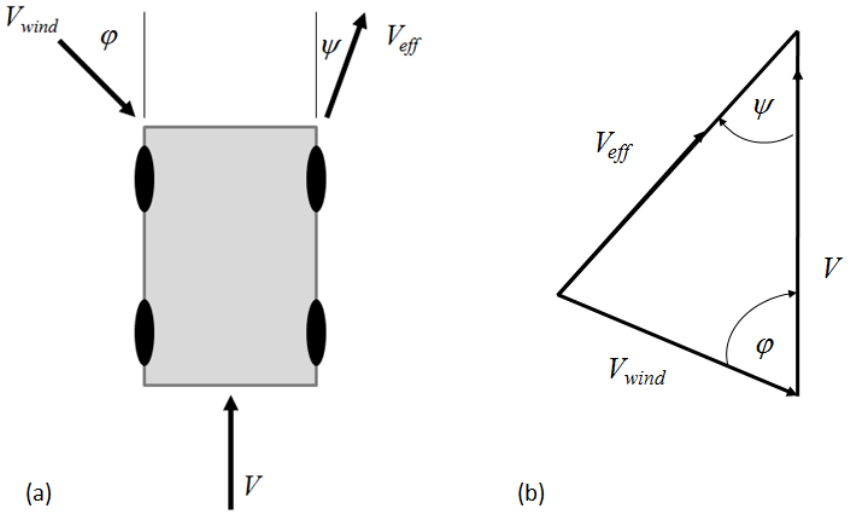

Figure 1: Diagram of influence of wind speed (a) upon relative velocity of the vehicle and (b) the resulting velocity triangle.

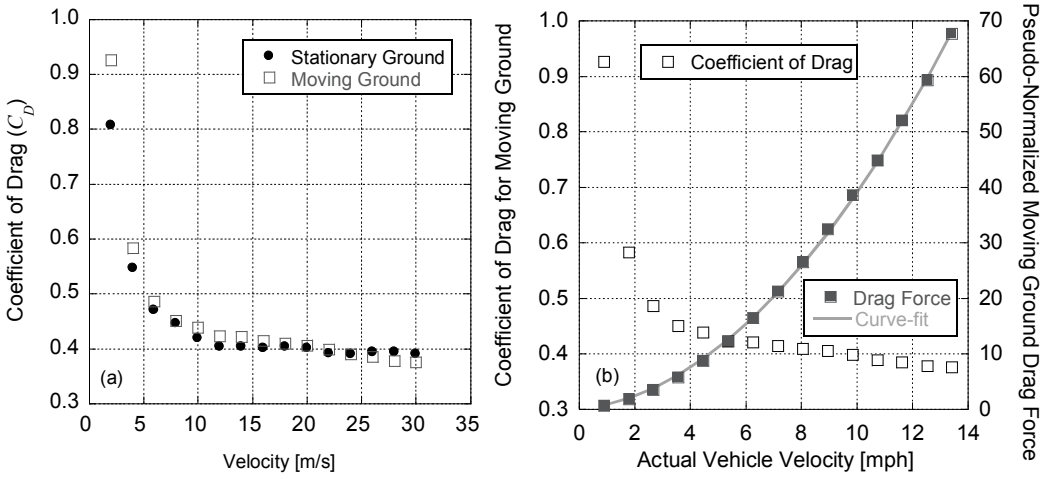

Figure 2: Geropp and Odenthal data of (a) coefficient of drag for stationary and moving grounds [9] and (b) normalization by the authors in order to determine C_D functionality.

In addition, the fundamental coefficient of drag does not necessarily have a singular value. It is a function of the Reynolds, Froude and Mach numbers describing velocity, free-surface and compressibility effects, respectively [11]. This is evident in the work of Geropp and Odenthal who endeavor to find the coefficient of drag in Figure 2a as a function of stationary and moving ground [9]. Geropp and Odenthal find that the effect of a moving ground slightly reduces the coefficient of drag. This variance is generally less than five percent but is more evident at lower velocities.

Combining the density and frontal area components (since Geropp and Odenthal omitted these values from their paper), creates a pseudo-normalized drag force that provides further investigation of the coefficient of drag:

$F_D' = \frac{F_D}{0.5\rho A_f} = C_D V^2$	(4)

From this equation, fitting the data of Geropp and Odenthal in Figure 2b to a second-order polynomial curve-fit, while incorporating the 1/5th scaling of their model finds the following:

$$F_D' = 0.3384V^2 + 0.5299V \quad (5)$$

with an R^2 value of 0.9997 between the curve-fit and data. Since the basic fundamental derivation of the drag force requires that it must have a squared dependency on velocity, this result indicates that the coefficient of drag can include an additional velocity component for increased accuracy.

Another factor influencing vehicle drag is the yaw drag that can have varying effects on the effective coefficient of drag depending on the body design of the vehicle:

$$C_{D,yaw} = k_D\left(1-\cos 6\psi\right) \quad (6)$$

Where k_D, the yaw drag coefficient, ranges from 0.02 for well streamlined vehicles to 0.053 for less streamlined sedans with sharp corners and square front ends [12]. While the traditional drag coefficient, C_D proves useful for modeling zero yaw-effect drag in straight-line and low wind conditions, the yaw drag coefficient allows for a better understanding of drag effects when the vehicle experiences non-zero yaw conditions.

As a result, a complete model of the coefficient of drag while incorporating wind effects is:

$$C_D = a_D + \frac{b_D}{V_{eff}\cos\psi} + k_D\left(1-\cos 6\psi\right) \quad (7)$$

and the resultant drag force becomes:

$$F_D = \frac{1}{2}\rho A_f\left[a_D + \frac{b_D}{V_{eff}\cos\psi} + k_D\left(1-\cos 6\psi\right)\right]\left(V_{eff}\cos\psi\right)^2 \quad (8)$$

with the traditional (zero yaw angle) value of C_D present in the form of a_D, the increased dependency on velocity included in b_D and the yaw effect of drag captured in the k_D term.

In addition to drag, the body of a vehicle can provide a lift force as a function of the planform area (A_p) of the vehicle:

$$F_L = \frac{1}{2}\rho A_p C_L \left(V_{eff}\cos\psi\right)^2 \quad (9)$$

where C_L is the coefficient of lift. However, the planform area is difficult to measure for a vehicle; hence, typical convention is to use the frontal area (A_f) for both the drag and lift forces [13]. The lift of a vehicle can effectively change the dynamic weight of the vehicle as follows:

$$Z = mg\cos(\theta) - F_L \quad (10)$$

This will factor into the rolling resistance and road gradation forces instead of being included directly in the force balance of Eqn. (1). Note that the slope of the road (θ) is included in the effective weight of the vehicle in order to provide the correct normal force to the road. Its derivation will be discussed later in this chapter.

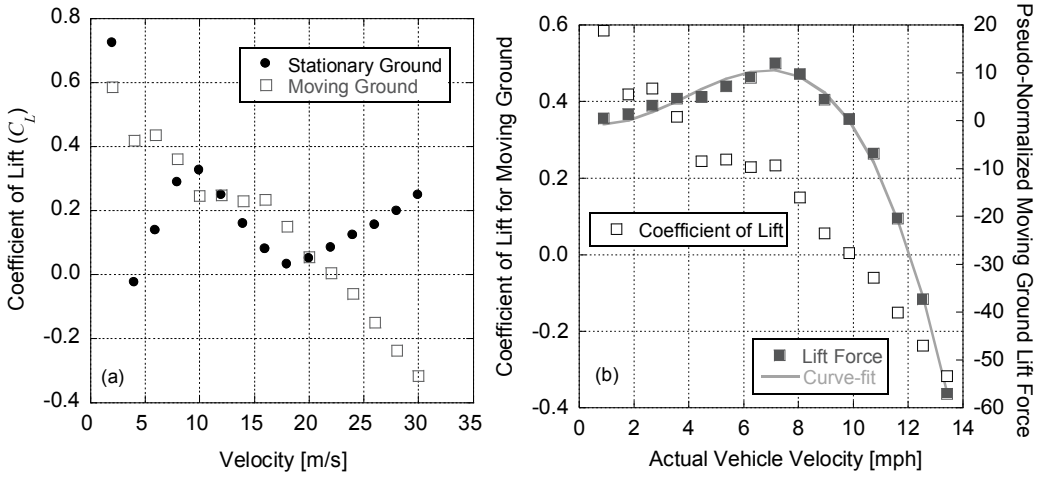

Figure 3: Geropp and Odenthal data of (a) coefficient of lift for stationary and moving grounds [9] and (b) normalization by the authors in order to determine C_L functionality.

In the same work of Geropp and Odenthal [9], they measure the lift force on a scale vehicle as a function of stationary and moving ground in Figure 3a. Unlike drag force where the moving ground has a small effect, for lift, the influence of a moving ground significantly changes the trend with respect to velocity. While not explicitly stated in their paper, the authors infer that this is a result of a large increase in the pressure forces on the underbody of the vehicle. Following the earlier example, a pseudo-normalized lift force provides investigation into the coefficient of lift:

$$F_L' = \frac{F_L}{0.5\rho A_p} = C_L V^2 \quad (11)$$

From this equation, fitting the data of Geropp and Odenthal in Figure 3b to a third-order polynomial curve-fit, while incorporating the 1/5th scaling of their model finds the following:

$$F_L' = -0.1016V_{eff}^3 + 1.1813V_{eff}^2 - 1.7851V_{eff} \quad (12)$$

with an R^2 value of 0.9961 between the curve-fit and data. Since the basic fundamental derivation of the lift force requires a squared dependency on velocity, this result indicates that the coefficient of lift can include two velocity components for increased accuracy.

Another factor on the lift force of the vehicle is the increase in lift forces due to the yaw moment:

$$C_{L,yaw} = k_L \sin^2 3\psi \quad (13)$$

where k_L ranges from 0.25 for well streamlined vehicles to 0.52 for non-streamlined sedans [12]. Similar to drag, C_L proves useful for modeling zero yaw-effect lift in straight-line and low wind conditions; however, the yaw lift coefficient allows for a better understanding of lift effects when the vehicle experiences non-zero yaw conditions

As a result, a complete model of the coefficient of lift while incorporating wind influence equals:

$$C_L = a_L\left(V_{eff}\cos\psi\right) + b_L + \frac{c_L}{V_{eff}\cos\psi} + k_L \sin^2 3\psi \quad (14)$$

and the resultant drag force becomes:

$$F_L = \frac{1}{2}\rho A_p\left[a_L\left(V_{eff}\cos\psi\right) + b_L + \frac{c_L}{V_{eff}\cos\psi} + k_L \sin^2 3\psi\right]\left(V_{eff}\cos\psi\right)^2 \quad (15)$$

with the traditional value of C_L present in the form of b_L.

Modeling the interaction between vehicle tires and driving surfaces requires consideration of the rolling resistance force. Often, research represents this force through a constant coefficient of rolling resistance (μ_{RR}) multiplied by the vehicle weight:

$$F_{RR} = \mu_{RR} mg \quad (16)$$

This model again works well for a fundamental understanding of rolling resistance; however, it lacks additional considerations due to velocity and tire pressure. As velocity

increases, the contact area of the tire decreases due to centrifugal effects. The tire diameter increases, effectively narrowing the tire and reducing the area of contact between the tire and the road. The same concept holds true for an increase in tire pressure. As the tire pressure increases, the tire diameter increases reducing the contact area and the overall rolling resistance of the vehicle.

Taking into account these influences, Grover proposed a model of rolling resistance that includes load, tire pressure (p_{tire}) and speed. While Grover made no mention of units, the only means for preventing a unit imbalance is to provide a reference pressure (p_{ref}) of one kilopascal and reference vertical load (Z_{ref}) of one newton [7]:

$$F_{RR} = \left(\frac{p_{tire}}{p_{ref}}\right)^{\alpha} \left(\frac{z}{z_{ref}}\right)^{\beta} \left(a_{rr} + b_{rr}V + d_{rr}V^2\right) \quad (17)$$

Through the subsequent validation of this model, Grover enhanced the force due to rolling resistance by representing the effect of velocity and tire pressure changes without the need for auxiliary models. Note that this model does include the effective weight of the vehicle due to lift. Swift determined that the lift forces on automobiles are relatively small in comparison to the overall mass of the vehicle and generally recommended neglecting these effects; e.g., F_L = 0 [2]. This paper follows this assumption; however, the lift force discussion is included previously for completeness as high-speed vehicles (e.g., formula one) will require inclusion of this term.

Calculation of the road gradation force includes the road angle based on the change in elevation:

$$F_{GR} = mg\sin\theta \quad (18)$$

where the slope of the road is equal to:

$$\theta = \tan^{-1}\left\{\frac{\text{elevation}(t_1) - \text{elevation}(t_0)}{0.5\left[\text{velocity}(t_1) + \text{velocity}(t_0)\right](t_1 - t_0)}\right\} \quad (19)$$

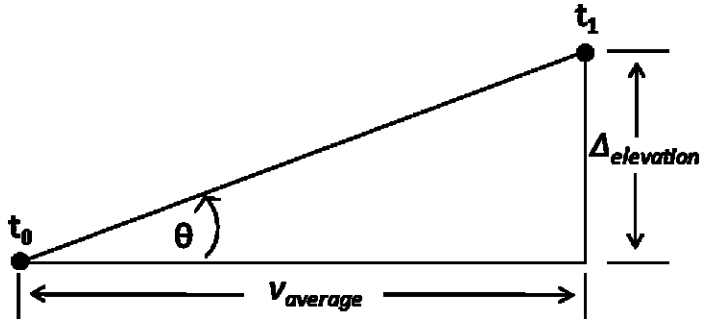

Figure 4. Illustration of elevation change over a distance using average velocity.

Evaluation of the angle of the road occurs using the change in elevation and horizontal distance as indicated in Figure 4. The average velocity and difference in time between two data points provides an estimate for the variation in horizontal distance.

The combination of all of the above individual forces results in the following force balance during a coast down test:

$$F_{TE} = F_D + F_{RR} + F_{GR} \quad (20)$$

In order to model the deceleration of the vehicle, the force balance is more useful in derivative format:

$$-m\frac{\partial V}{\partial t} = F_D + F_{RR} + F_{GR} \quad (21)$$

After performing a coast down experiment, analysis of the test data occurs in order to create a velocity versus time profile. The model is run using all of the components in an Explicit Euler method and compared to the actual velocity profile as described further in a section 4.2.1.

2.2 Equipment

The scope of this project involves model calibration using equipment with reasonable accuracy while remaining economically feasible in comparison to wind

tunnel testing. As the previous section elucidates, the model requires recording the vehicle elevation, vehicle velocity, and wind speed with respect to time. For dynamic vehicle parameters, on board data collection utilizes an Auterra DashDyno OBD-II port data logger. The vehicle provides diagnostic information to the port via a high-speed controller area network (CAN). The DashDyno then interprets the CAN strings and converts the information to text and graphical displays available to the user. It can log up to 280 available parameters from the OBD-II port at a data frequency of 2 Hz. A Secure Digital (SD) card then stores this data in a universal comma separated value (CSV) format. The use of an OBD style data logger also allows for the measurement of fuel used during testing. This provides the ability to correct weight adjustments based on calculations of the fuel consumed.

Four analog inputs on the DashDyno allow implementation of external sensors for vehicle data not available through the CAN network. For this paper, the authors implement a Global Positioning Sensor (GPS) in order to measure vehicle velocity and elevation. The Garmin GPS 18x puck style receiver chosen is able to perform serial communication with the DashDyno and maintains a small overall volume (less than 600 cm^3); essential to ensure minimal effects on aerodynamic drag when placed on the exterior of the vehicle. The downfall of this particular receiver is the lack of ability to communicate elevation data to the DashDyno. To overcome this, the authors post-process the data using a free software program (GPSvisualizer) in order to query multiple geological survey databases in order to provide elevation data using the geographic coordinate data provided by the system. This method is rudimentary, but allows for the use of an inexpensive GPS receiver.

To account for the effect of wind, it is necessary to measure both magnitude and direction. Many of the cost effective units are capable of data logging at a minimum of one-minute intervals. However, coast down testing requires a significantly higher sampling rate given the short amount of time required for a typical trial. The Wind Works wind data logging system from Inspeed stores both wind direction and magnitude data in any fraction of a minute interval. Logging of the wind information to a computer makes the system capable of storing large amounts of data with no additional storage medium. The Wind Works kit measures speeds from 5 km/h to 250 km/h with a 1 Hz sampling rate.

To calculate changes in vehicle mass, this work employs a set of Longacre four-wheel scales. This particular set of scales provides weight measurements accurate to 0.1 percent. The utilization of four-wheel scales allows a maintenance of front to rear and corner weight ratios while changing the vehicle weight. Lead-acid batteries added to the vehicle during testing provided for the addition of vehicle weight in order to alter rolling resistance. Batteries provide a high mass density and allow for quick vehicle weight adjustments during testing.

The equipment set described is capable of recording all of the required parameters and retails for less than $600 US dollars. While more sophisticated devices record data at higher precision and sampling rates, the aforementioned equipment is capable of logging the required information, and it is cost-effective while maintaining multiple vehicle versatility.

2.3 Test Location and Conditions

While a closed test track is an ideal research facility for performing coast down trials; such a facility is not always available and commonly includes fees associated with usage. As a replacement, a straight and horizontally flat public road with minimal traffic is used here as an acceptable alternative. For this reason, this work utilizes a public highway service road to perform the coast down tests. The test road is nearly three kilometers long with less than a two degree heading variance and includes an additional two kilometers of acceleration area. Overall elevation varies by less than three meters from beginning to end (average 0.1% grade); however, localized variation can be much higher. All testing occurs at night in an effort to reduce traffic related effects. The road surface consists of uniform chip seal asphalt with intermediate sized mixed aggregate.

Table 1: Coast down test conditions for model calibration.

Test	Barometric Pressure [kPa]	Temp [C]	Humidity [%]	Avg. Wind Speed [m/s]	Peak Gust [m/s]	Avg. Wind Direction [deg]
0	101.3	9.4	70	-	-	-
1	101.2	10.1	70	0.5	1.3	114
2	101.3	9.8	70	2.1	2.7	189
3	101.4	10.7	70	1.5	2.6	192
4	101.3	11.2	70	1.6	2.2	192

During testing, temperatures varied from 9°C to 11°C. Atmospheric pressure and humidity remained constant at 101.3 kPa and 70% respectively. Wind speeds were relatively constant at 1.5 to 2 m/s for most of the testing period with minimal gusting as indicated in Table 1.

2.4 Test Method

Testing is performed using a small two door sports car with a relatively low manufacturer provided aerodynamic drag coefficient of C_D=0.29. The vehicle is equipped with an all-season, low aspect ratio tire common for the automobile type. This tire design has typical rolling resistance coefficient of μ_{RR}=0.013-0.016 on the given road surface [14]. In addition, the vehicle is fitted with a manual transmission, which ensures quick and complete disengagement of drive systems during coast down trials.

For consistency, the authors follow the SAE recommended vehicle coast down procedure. For each trial, the driver brings the vehicle up to the maximum allowable velocity for the test road (27 m/s) and holds it constant for a minimum of three seconds in order to stabilize the vehicle. Simultaneous disengagement of the throttle and transmission occur and the vehicle allowed to the coast down until absolute velocity is less than 10 m/s. This test procedure is fully described by Petrushov [3] and Morelli and Nuccio [1].

Four different loads and four different tire pressures used during testing allow for the ability to model tire pressure and load changes. Load is varied linearly in four increments from the base weight of the vehicle with driver and all equipment installed (1622 kg) to the Gross Vehicle Weight Rating (GVWR) of the vehicle (1831 kg). Linear variation of the tire pressure occurs from the minimum recommended operating pressure (138 kPa) to the maximum recommended operating pressure (345 kPa). Tire pressure is measured using an Omega DPG5500 Series digital pressure gauge. The digital display coupled with hundredth pounds per square inch (PSI) resolution allowed for accurate tire pressure changes. Of importance, Grover implemented this method for

testing tire rolling resistance in a test rig; however, the above method expands on the suggested ranges to further allow for exponent calculations over the entire operating range of the vehicle [7]. As a result, 64 trials transpire with four trials executed at each load-pressure combination. For consistency, testing of each combination occurs using two runs in the Northern direction and two runs in the Southern direction.

Elimination of the influence of the wind-measuring equipment on the aerodynamic drag force of the vehicle occurs by placing the device at the midpoint of the test track. This is because Swift found placing an anemometer on the roof of the automobile is capable of causing a 22% increase in the aerodynamic drag force [2]. Moreover, the efforts involve placing this device a suitable distance from the test track in order to ensure minimal effects from the passing vehicle.

3. Model Computation and Optimization

For calculation of the coefficients and exponents, optimization follows the method of a non-linear least squares curve fit. This method finds the best curve by minimizing the residuals between the actual data and the curve at each data point. The non-linear least squares method estimates the best curve by minimizing the vertical residuals between the data points. Generally, this is a downfall of the method since the “best-fit” is modeled by minimizing the perpendicular residuals. However, the minimization of the vertical residuals provides the desired reduction between actual speed and modeled speed residuals. For the proposed model, application of this method to the velocity versus time profile happens for each of the coast down trials. Each time step compares the modeled speed to the actual speed from the test data while squaring and summing the difference between the two values over the entire data set:

$R^2 = \sum_{t=0}^{n} \left(V_{\text{actual},i} - V_{\text{model},i} \right)^2$	(22)

Optimization transpires by changing the model variables until minimizing the summation to a set tolerance (1×10^{-6}). Ideally, this tolerance should be zero:

$\frac{\partial R^2}{\partial V_i} = 0$	(23)

To compute the least squares fit, the model is coded in MATLAB. MATLAB allows custom computing scripts to be created and executed utilizing a simplistic programming language with optimization toolboxes available to perform the needed analysis. The specific routine utilized for optimization in MATLAB involves the Gauss-Newton method to minimize the sum of the residuals. Other methods are acceptable; however, since the Gauss-Newton method does not require the calculation of the second derivatives of the function, selection of this routine retains computational efficiency.

The authors first employed the model with a constant aerodynamic drag coefficient and a constant, velocity independent coefficient of rolling resistance. Application of the least squares fit for this method provides an estimate of the magnitude of each of the variables for the proposed model. Utilizing the results from this method as initial values, optimization of each variable then occurs while holding all other variables constant. The resulting values then become a new set of initial values, and all variables are allowed to vary one standard deviation in either direction for the final optimization routine. This systematic approach reduces the probability of the least-squares fit curve settling on local minimums.

4. Results and Discussion

Upon completion of the computation and optimization routines, comparison of the proposed model and its accuracy occurs with respect to the alternative methods previously mentioned. The results of this comparison and a discussion of the results follow in this section.

4.1 General Model Results

In order to understand the effects of increasing model sophistication, optimization of the model first was performed using traditional constant drag and rolling resistance coefficients. It is important to note that the authors omit three of the runs in this analysis since they contain erroneous data mostly likely caused by the influence of passing vehicles as noted in the logbook during testing. Optimization of the model in this manner results in an average value of C_D=0.396±0.00976, nearly 37% larger than the manufacturer claimed value of C_D=0.29 and well outside the 95% confidence interval. A significant source of error associated with this method is the fitting of test data from a multifaceted situation to only two variables. It appears that the data is too complex to be fit to a simplistic coast down model. Geropp and Odenthall also noticed similar effects when comparing the effects of moving ground against wind tunnel testing [9].

The calculated estimate of μ_{RR}=0.0122±0.000368 is slightly lower than the expected value of 0.013 to 0.016, but not enough to disregard the model in this manner as erroneous. While the coefficient of rolling resistance (μ_{RR}) remains relatively constant across all trials, the rolling resistance forces due to changes in load and

pressure do follow the expected trend and grow with increasing load and decreasing pressure as seen via the linear curve-fits in Figure 5.

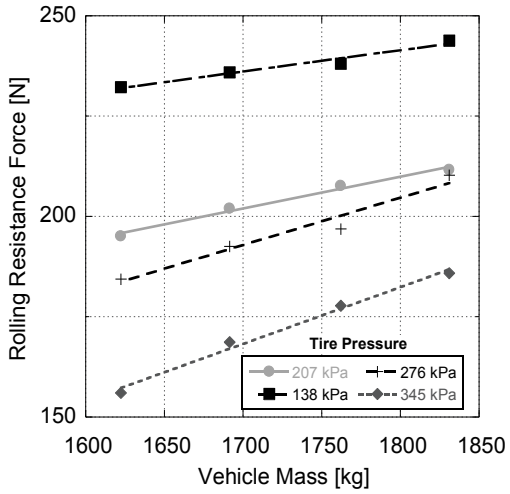

Figure 5: Pressure and load effects on constant rolling resistance force.

While the rolling resistance values are near the expected range, the lack of velocity effects limits the application of these values. The trends are as expected, but the accuracy of the results cannot be determined without an acceptable benchmark. Rolling resistance is dependent on a variety of factors such as exact load, tire design, tire wear, road surface, ambient weather, and vehicle design. An estimate of the rolling resistance for the exact testing conditions is unavailable, and the authors utilize an estimated range found in the literature. The overall accuracy of a model can generally be determined by analyzing the residuals of the least squares fit; however, the errors in aerodynamic drag modeling using this method likely have an observable effect on rolling resistance modeling as well.

4.2.1 Proposed Model Coefficient Results

The results from the standard model provide the magnitudes and initial starting points for variables of the proposed model. In order to avoid using an excessive

amount of variables essentially creating a highly flexible curve-fit, this work neglects forces deemed to have little effect on the vehicle dynamics through the literature review. These forces include the vehicle lift and yaw coefficient k_D. Implementation occurs for each trial individually first, followed by the entire set of data in order to compute average values. Because of the non-linearity involved and the potential to skew results, initial values used for the rolling resistance exponents are α=-0.3 and β=0.9. These are average values determined by Grover for the given tire design and size [7]. Since Grover indicates other values vary only slightly from these average values, in order to minimize any potential errors induced by allowing these variables to vary significantly during optimization, this work holds these values constant for the initial optimization effort. A subsequent run then occurs allowing full variability when finalizing the best fits for all values. Determination of the error bounds requires least squares fit for each of the trials with a subsequent statistical analysis on the results of each trial. Table 2 lists the average computed coefficients and exponents along with error bounds for the results of the proposed model. Computation of the statistical limits happens by weighting the coefficients of each trial equally. The use of this method allows determination of statistical data without needed evaluation of the second-order derivatives of the function.

Table 2: Proposed model statistical values when each trial is optimized.

Parameter	$\bar{x}$	Σ	95% Confidence Limit
a_d	0.285	0.00329	0.285 ± 0.0008
b_d	0.0913	0.00238	0.0913 ± 0.0006
a_{rr}	0.119	0.0256	0.119 ± 0.006
b_{rr}	0.00388	0.00152	0.00388 ± 0.0004
d_{rr}	0.0000204	0.0000119	0.0000204 ± 0.00001
α	-0.286	0.0537	-0.286 ± 0.0135
β	0.856	0.0189	0.856 ± 0.0048

While the first optimization gives the best understanding of the overall bounds and statistical accuracy of the model, the coefficients may not provide the best universal fit for all trials. Each data set is subject to a weighted average as the number of data points varies by trial; e.g., some coast down procedures take slightly longer to accomplish. In order to determine the best fit for the entire data set, the authors employ a least squares fit by minimizing the residuals of all data points across all trials. This method presents a set of coefficients and exponents representative of the actual operating conditions of the vehicle. Table 3 presents the results of this exercise with Figure 6 illustrating a comparison between a modeled coast down profile and the actual test data.

Table 3: All trials least-square fit results.

Parameter	$\bar{x}$
a_d	0.283
b_d	0.0891
a_{rr}	0.119
b_{rr}	0.00388
d_{rr}	0.0000204
α	-0.292
β	0.895

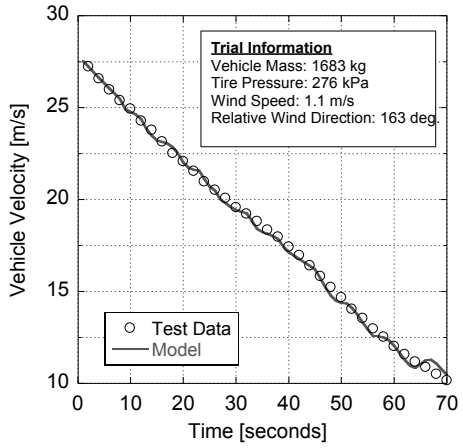

Figure 6: Example of typical coast down profile compared with model.

Both the modeled and actual deceleration rates fluctuate throughout the entirety of the trial with this effect evident for all tests. Since this appears to negate the deceleration forces of the vehicle and aid in maintaining velocity, this is likely caused by local changes in elevation.

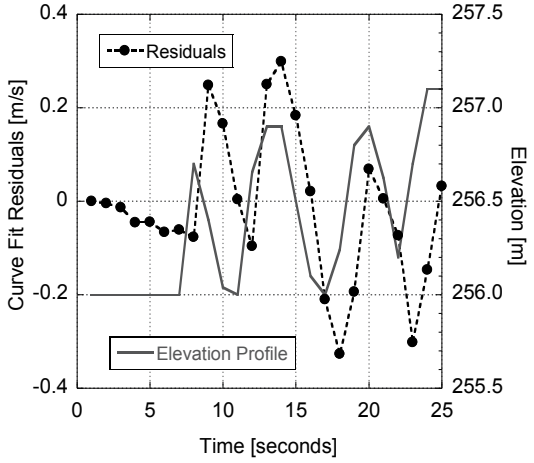

Figure 7: Elevation change influence on model error.

In order to investigate the local elevation change on the error fluctuation, Figure 7 plots the model residuals against the elevation profile at the beginning of the trial presented in Figure 6. Since the error occurs over the entire length of the test, this figure only

presents the beginning of the experiment. The resulting Pearson correlation coefficient of 0.899 between the vehicle's elevation and the model error indicates a strong linear relationship between the model residuals and elevation data. Given the moderate resolution and limited sampling rate of the GPS system, this error is to be expected. In particular, GPS Visualizer uses whole values for elevation that require interpolation in order to provide estimates for elevation at each time step. Given that the local fluctuations in elevation are generally less than one meter; the resolution of the error measurement is likely the root of this issue.

4.2.2 Proposed Model Aerodynamics

As previously mentioned, the work of Geropp and Odenthal indicates the aerodynamic drag coefficient is velocity dependent [9]. Using Eqn. (7) and the average model coefficients of Table 3, Figure 8 provides the dynamic aerodynamic drag coefficient for the typical operating range of the vehicle. The drag coefficient decreases exponentially as velocity increases up to about 10 m/s and eventually converges on C_D=0.286, near the manufacturer provided coefficient of C_D=0.29. As the velocity increases, b_D tends towards to zero and the drag coefficient becomes a function of only a_D.

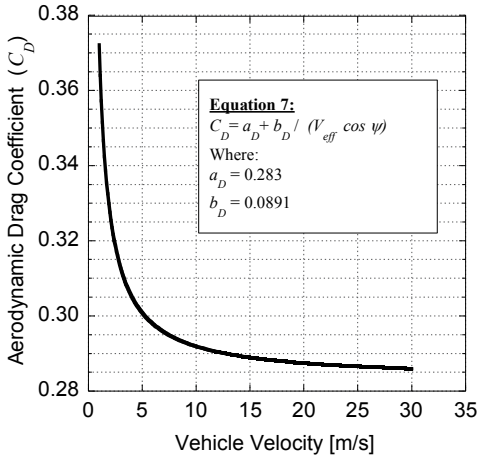

Figure 8: Aerodynamic drag coefficient velocity profile as computed by the model.

4.2.3 Proposed Model Rolling Resistance

The proposed model rolling resistance force has constant, linear and quadratic velocity dependent terms in its representation. Using the coefficients and exponents in Table 3, Figure 9 plots the rolling resistance force using the manufacturer suggested tire pressure (207 kPa) and minimal loading (1623 kg). The plot shows strong linear and slight quadratic velocity dependence. A linear curve-fit plotted in this figure demonstrates the magnitude of this quadratic term; and, since it is relatively small, it may be feasible to remove this component of the model in future efforts.

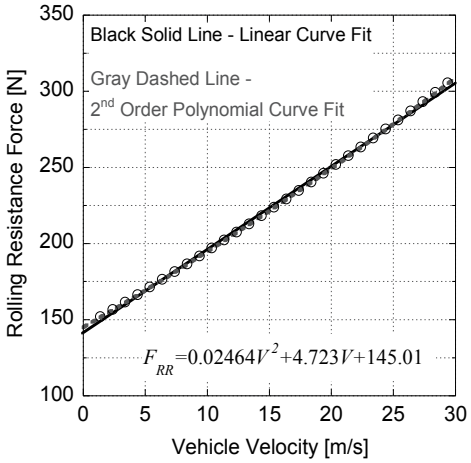

Figure 9: Rolling resistance force velocity profile.

Comparing the results with the standard constant coefficient model (μ_{RR}) first requires fitting Figure 9 to a second-order polynomial:

$$F_{RR} = 0.02464V^2 + 4.723V + 145.01 \quad (24)$$

This quadratic curve-fit generated mimics the previous work of Geropp, Krajnovic, and Swift [2, 8, 9]. Then, the authors make a comparison between Eqn. (16) and (17), as follows:

$$F_{RR} = \mu_{RR} mg = p_{tire}^{\alpha} Z^{\beta} \left(a_{rr} + b_{rr} V + d_{rr} V^2 \right) \quad (25)$$

Solution of the proposed model for the constant coefficient requires integration of Eqn. (24) in order to determine the average rolling resistance force followed by dividing each side by the total load:

$$\mu_{RR} = \frac{\frac{1}{30}\int_0^{30} \left(145.01 + 4.723V + 0.02464V^2\right) dV}{1623 \times 9.81} \cdot \frac{[N]}{[kg] \cdot \left[m/s^2\right]} = 0.0141 \quad (26)$$

The resulting value fits well within the expected range of Wong (0.013-0.016) for the given tire design and road surface [14]. Moreover, this outcome is an improvement over

the simple model result of μ_{RR}=0.0122 while additionally considering rolling resistance dependency on tire pressure and velocity.

The larger magnitudes associated with the 95% confidence limit of α and β indicate that these parameters do not capture all factors affecting the rolling resistance coastdown performance of the vehicle. These factors could be related to tire and road surface temperature changes, as well as the relatively limited number of tire pressure and vehicle loading experiments analyzed. Future work by the authors will explore this dependency in more detail.

5. Recommendations

The primary limiting factor in the accuracy of the proposed model is the equipment utilized. In particular, the use of a GPS system with a higher sampling rate and elevation measurement would significantly improve the data collection and, in turn, the model. Such a system would require a more expensive data logging unit and GPS components. The use of a similar GPS device with the addition of elevation measurement would allow for improving the primary component of the data collection system at a minimal cost; however, the data set would still be limited to the 1.5 Hz maximum sampling rate of the DashDyno.

Moreover, the use of a wireless anemometer capable of synchronizing to the same time stamp as the primary data logging system would allow for the benefits of off-vehicle anemometry while eliminating the ambiguity of aligning time stamps from multiple devices. However, its design and integration into the on-board data logger would be somewhat expensive and time consuming. The test data would also benefit from the use of a weather station capable of directly measuring air density (or pressure

and temperature) at the testing location throughout the experimental period. A local weather station (within five miles of test site) was used for temperature and humidity effects during the testing; however, local deviations may have impacted the results.

The use of a closed test track would allow higher initial velocities, thus improving the sample data set. The elimination of grade change would also improve the ability to assess model accuracy. These items are necessary before the inclusion of further effects like tire and road surface temperature influence on rolling resistance. Finally, the difficulty associated with measuring the lift parameters and the relatively small magnitudes of the lift forces were ignored in this analysis. This assumption is likely a portion of the remaining error associated with the analysis. However, the aforementioned issues associated with measuring actual lift coefficients for road vehicles can introduce other sources of error that can be larger than omitting the lift forces in the first place.

6. Conclusions

The proposed force equations increase the accuracy of a general coast down model by including dynamic terms in both rolling resistance forces and the aerodynamic drag coefficient while adding the flexibility necessary to incorporate changes in tire pressure and load. The accuracy of the model is highly dependent on the resolution and sampling rate of the data acquisition equipment used. Given the relatively small overall effect of the quadratic velocity dependent term in the rolling resistance model, it may be appropriate to ignore this term when using low-resolution equipment.

The model is calibrated using consumer grade data logging equipment and an easily attainable public testing facility. A large portion of the cost associated with the

testing relates to the equipment used to collect data. As a result, after purchasing the equipment, repetition of testing and modeling can occur for numerous vehicles and design changes with minimal associated costs. An inexpensive testing procedure coupled to an accurate model can prove to be a highly advantageous alternative to both traditional and moving floor wind tunnel testing when the lack of available funds and facilities limit such testing. In particular, the cost of the equipment purchased was equivalent to less than two hours of stationary wind tunnel testing illustrating the cost effectiveness of the methodology presented.

Acknowledgements

This work was supported by Smith Electric Vehicles and the University of Kansas Transportation Research Institute [grant number IND 0066912].

References

1. Morelli, A., et al., *Automobile aerodynamic drag on the road compared with wind tunnel tests*1981: Society of Automotive Engineers, Inc.
2. Swift, A., *Calculation of vehicle aerodynamic drag coefficients from velocity fitting of coastdown data.* Journal of Wind Engineering and Industrial Aerodynamics, 1991. **37**(2): p. 167-185.
3. Petrushov, V., *Coast down method in time-distance variables.* SAE transactions, 1997. **106**: p. 663-685.
4. Lucas, G. and A. Emtage, *A new look at the analysis of coast down test results.* ARCHIVE: Proceedings of the Institution of Mechanical Engineers, Part D: Transport Engineering 1984-1988 (vols 198-202), 1987. **201**(24): p. 91-97.
5. Grover, P.S. and S.H. Bordelon, *New Parameters for Comparing Tire Rolling Resistance.* 1999.
6. Larminie, J. and J. Lowry, *Electric vehicle technology explained*2003: Wiley.
7. Grover, P., *Modeling of rolling resistance test data.* 1998.
8. Krajnovic, S. and L. Davidson, *Influence of floor motions in wind tunnels on the aerodynamics of road vehicles.* Journal of Wind Engineering and Industrial Aerodynamics, 2005. **93**(9): p. 677-696.
9. Geropp, D. and H.J. Odenthal, *Drag reduction of motor vehicles by active flow control using the Coanda effect.* Experiments in Fluids, 2000. **28**(1): p. 74-85.
10. Fago, B., H. Lindner, and O. Mahrenholtz, *The effect of ground simulation on the flow around vehicles in wind tunnel testing.* Journal of Wind Engineering and Industrial Aerodynamics, 1991. **38**(1): p. 47-57.
11. Fox, R.W. and A.T. Mc Donald, *Introduction to fluid mechanics.* 1985.
12. Bowman, W.D., *Generalizations on the Aerodynamic Characteristics of Sedan Type Automobile Bodies.* Soc. Automot. Eng., Paper SAE, 1966. **660389**.
13. McBeath, S., *Competition Car Downforce: A Practical Guide*1998: GT Foulis.
14. Wong, J., *Theory of ground vehicles*2001: Wiley-Interscience.

CHAPTER 3: Expanding the Peukert Equation for Battery Capacity Modeling Through Inclusion of a Temperature Dependency

Austin Hausmann[1] and Christopher Depcik

Department of Mechanical Engineering - University of Kansas, Lawrence, Kansas (United States)

Abstract

The accuracy of Peukert's equation for battery capacity lessens under dynamic loading and varying temperature conditions. Previous attempts by others endeavor to overcome the current shortfall; however, many still neglect the inclusion of a temperature dependency. This paper investigates the feasibility of Peukert's equation for practical automotive situations and expands upon the equation in order to include both variable current and temperature effects. The method proposed captures these requirements based on the theory that a battery contains a relative maximum absolute capacity, different from manufacturer 20-hr specifications, and the specific discharge conditions determine the rate at which to remove this capacity. Experimental methods presented in the paper provide an economical testing procedure capable of producing the required coefficients in order to build a high-level, yet accurate state of charge prediction model. Moreover, this work utilizes automotive grade lithium-based batteries for realistic outcomes in the electrified vehicle realm.

Keywords: Peukert's equation; battery testing; capacity modeling; state of charge;

Words: 147

Nomenclature

Variable	Description	Units
C	Rated capacity at specified discharge rate	[ampere.hour]
C_d	Discharged capacity	[ampere.hour]
C_n	Nominal capacity	[ampere.hour]
C_P	Peukert capacity	[ampere.hour]
C_r	Capacity remaining	[ampere.hour]
ΔC_r	Change in capacity remaining	[ampere.hour]
H	Rated discharge Time	[hours]
I	Current draw	[amperes]
I_{eff}	Effective current draw	[amperes]
I_{nom}	Nominal current draw	[amperes]
I_{ref}	Reference current	[amperes]
k	Peukert's constant	[-]
R	Resistance	[ohms]
T	Battery temperature	[K]
T_{ref}	Reference temperature	[K]
t	Time	[s,hr]
Δt	Change in time	[s,hr]
V	Battery voltage	[volts]
α,γ	Current coefficients	[-]
β	Temperature coefficient	[-]

1. Introduction

In 1897, Wilhelm Peukert tested lead-acid batteries at a constant current and determined that a single equation could be used to relate the capacity of the battery, C_P in ampere-hours, to its discharge rate [1, 2]:

$$C_P = I^k \cdot t \quad (1)$$

where t is the time in hours, I is based on the constant discharge rate relative to one-ampere, and k is a calibrated, dimensionless constant. It is worth noting that in this form, Peukert's Law presents a unit imbalance. The intent of this equation is to account for the intrinsic losses associated with discharging batteries at elevated currents. In

particular, when a battery is discharged at increasingly higher currents, the internal cell resistance increases and the recovery rate of cells decreases [1, 3]. Later efforts by Pavlov demonstrated that the decrease in recovery rate is due a degradation in the number of active sites in the positive active material, as well as an increase in the resistance between the positive active material and the electrolyte [4]. The exponent, k, became known as Peukert's constant and is designed to account for these losses [5]. A value close to one represents a well-performing, efficient battery and will increase as the cell efficiency decreases [1].

It is often useful to look at Peukert's equation in terms of discharge time relative to the rated discharge time (H) [5]. Reformulation to a known capacity and discharge condition yields:

$t = H\left(\frac{C}{IH}\right)^{k}$	(2)

where the battery capacity, C, is generally specified as a 20-hour rate from the manufacturer. This provides a better indication of estimated run time; however, the equation continues to require a constant discharge current. This C nomenclature will be used later in this effort when describing the experimental tests employed.

Doerffel and Sharkh explain that the Peukert equation cannot be used to predict remaining capacity accurately unless the battery is discharged at a constant current and constant temperature [5]. In many real world situations, batteries discharge at varying currents and experience a wide array of temperatures. This is particularly true of electrified (hybrid, plug-in hybrid and battery electric) vehicles, a primary interest of the authors. Quite often, the Peukert equation is used in power monitoring and supply systems [6, 7]; however, the drawbacks associated with more dynamic discharge

environments present challenges for this model. The error introduced by attempting to model a dynamic load can be quite substantial, as the average discharge current does not accurately represent the discharge profile. For example, Rakhmatov et al. found the error associated with this runtime calculation is often more than 20% and even as high as 100% [8]. In addition, it has been documented that a battery undergoing high discharge currents can be modeled as empty using Peukert's equation, but still have energy remaining at lower discharge currents [1, 5, 9, 10].

When considering an application such as an electrified vehicle, the discharge time is typically much shorter (one to eight hours) than power monitoring or power backup systems. An alternative method of using Peukert's equation for varying current is based on a rolling average technique in order to calculate the average discharge current over a previous time span and assume this value as constant over the same given time span [11, 12]. However, this method can result in a simulated current draw even though no energy is physically being removed [5]. Another generally accepted form for improving Peukert's equation utilizes variable current calculated as an pseudo, effective current (I_{eff}) [13-15]:

$$I_{eff} = I\left(\frac{I}{I_{nom}}\right)^{k-1} \quad (3)$$

where I is the actual discharge current and I_{nom} is the nominal current relating to the manufacturer supplied capacity (typically the 20-hour discharge rate).

In both alternative methods, use of the effective discharge current allows calculation of the total capacity removed from the battery:

$$C_d = \sum\left(I_{eff} \cdot \Delta t\right) \quad (4)$$

where the capacity discharged (C_d) is the total capacity removed from the battery based on the effective current over time. Thus, the capacity remaining (C_r) is equal to the nominal capacity (C_n), given by the manufacturer as a 20-hour discharge rate, minus the capacity discharged:

$C_r = C_n - C_d$	(5)

Both methods have been known to show improved estimation of discharge capacity for varying current discharge [5, 6]; however, both solutions also neglect temperature effects.

Of interest for this work, lithium based batteries typically demonstrate higher ion transport between the electrode and electrolyte as compared to other battery technologies such as lead-acid [16]. This rate increase allows lithium based batteries to be discharged at relatively higher rates with less loss of performance, resulting in higher cell efficiencies and, thus, reduced values for *k* (closer to one). Another interesting aspect of lithium batteries is the relatively flat voltage profile throughout the discharge profile. While this aspect provides a more constant power source than a typical lead-acid battery, it hinders the ability to measure battery State of Charge (SOC) using voltage. Current methods for state of charge modeling use a combination of Coulomb counting (measuring the current at each time step and summing the values to achieve capacity) and voltage profiles to achieve a state of charge profile. However, this method makes accounting for losses difficult and has known accuracy issues [1].

Batteries of all chemistries demonstrate varying available capacities for different temperature profiles [1, 3, 17-19]. As the battery temperature decreases, the available capacity decreases due to retardation of the chemical metabolism of the cells effectively hindering the chemical reaction rate [1]. This aspect is completely disregarded in

Peukert's equation and can lead to significant errors for even slight changes in environmental conditions or battery self-heating effects [5, 20]. For example, Gao et al. [19] demonstrates this temperature relationship for lithium-ion battery cells as illustrated in Figure 1. As a result, Peukert's equation only holds valid at room temperature while also assuming a constant discharge rate.

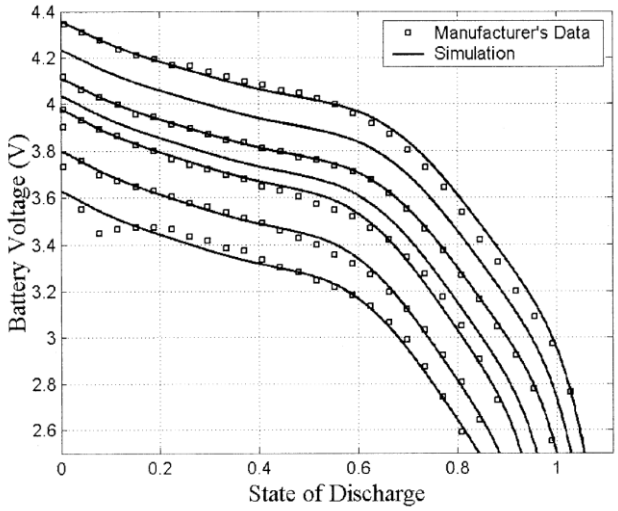

Figure 1: Gao et. al data for Lithium-Ion capacity and temperature relationship, at temperatures of (top to bottom) 45 °C, 34 °C, 23 °C, 10 °C, 0 °C, -10 °C, -20 °C [19].

While several authors demonstrate empirical test results [21-24], there is a relatively limited amount of information within the literature for dynamic battery capacity temperature modeling using automotive grade batteries. The most accurate models include electro-chemical processes in order to define battery performance [25]. The use of such a model can correctly encompass numerous battery phenomena like electrode geometries, concentration of the electrolyte, diffusion coefficients, transfer coefficients, reaction rate coefficients, and other lower-level phenomena [25-32]. Hence, while the creation of an electro-chemical model is likely more exact in its predictions and can provide better results, the creation, calibration, and implementation of such models

requires significant computational capabilities. This makes these simulations less suitable for on-road vehicular battery prediction. Additionally, the extensive effort spent on such models can quickly become inapplicable if the system in question requires a change in cell chemistry or configuration since the models are often calibrated to a specific battery and pack configuration. As a result, the majority of these models requires either widespread calibration, exhaustive computational resources, or fails to tune the models for dynamic discharge conditions limiting their effectiveness in mobile applications.

As an alternative to electro-chemical endeavors, analytical, physically-based simulations often provide the necessary accuracy without the calibration and chemical kinetic modeling [25]. The work of Gao et al. [19] accurately models not only temperature effects through analytical methods, but also dynamic current and cell resistance. However, this effort requires data storage of multiple measurements throughout the time-history of a discharge cycle, as well as numerical integration using numerous variables at each time-step. While analytical methods of this magnitude are simpler and more adaptable than electro-chemical models, they remain computationally intensive and require the use of an auxiliary computing system beyond that of a typical smart battery system or battery management system [25]. Furthermore, even simpler analytical models calibrated by cell chemistry also exist [33-36]. Often these models are calibrated by testing cells over a large matrix of constant current and constant temperature discharge conditions [33]. For example, Gold produced a macromodel that accounts for thermal capacity effects through cell resistance, ambient temperature, and heat capacity. However, of the three, only ambient temperature is modeled as dynamic

[35]. While both of these approaches can often be appropriate for controlled condition discharging, they do not necessarily apply to the highly dynamic world of electrified automobiles.

In an effort to facilitate a numerically efficient model for battery capacity estimation at different currents and temperatures, the following sections describe and validate an update to Peukert's equation. First, this work presents the derivation of the model illustrating the current and temperature dependencies. Then, the next section describes the experimental tests performed using commercial, automotive-grade lithium battery chemistries. Finally, simulation of these batteries based on dynamic current draw and battery temperature demonstrates the capability of the model.

2. Improved Model

In order to improve Peukert's equation, this work proposes an alternative definition of available capacity. Traditionally, manufacturers define the capacity of the battery for various discharge times, such as the 20-hour rate (e.g., Eqn. (2)). This concept proves confusing as it provides different values for battery capacity based on the usage profile [5]. Under high loading conditions, a battery may demonstrate empty conditions via the low voltage cutoff. However, this battery still has capacity that may be utilized at lower discharge rates [1, 3, 5, 9]. This characteristic can lead to ambiguity as to how much capacity actually remains. As a result, this effort assumes that a battery will always contain a remaining maximum available capacity (C_r). This capacity remains uniform regardless of the discharge conditions; however, the specific conditions during discharge influence the rate of discharge. Since the assumption involves an absolute maximum capacity remaining, capacity reaches zero at 100 percent depth of

discharge and can never fall below this zero value. In order to account for various discharge criteria effects, the conditions of the discharge routine are assumed to affect the discharge rate as follows:

$$C_r^{t+1} = C_r^t - \Delta C_r \quad (6)$$

where C_r^0 is an absolute capacity of a fully charged battery (zero percent depth of discharge) at time equal to zero.

As previously mentioned, this discharge rate is primarily dependent on the discharge current (I) and battery temperature (T) at each time t:

$$\Delta C_r = f(I, T) \quad (7)$$

When battery temperature decreases and load increases, the rate at which the capacity is reduced also increases. A constant (α), analogous to Peukert's constant, models the dynamic current (I_t) in amperes relative to a reference current (I_{ref}):

$$f(I) = \left(\frac{I_t}{I_{ref}}\right)^{\alpha} \quad (8)$$

Conditions similar to Peukert's law should control this exponent, as long as one uses a one-ampere reference current as the authors have done.

In order to account for temperature dependency in Kelvins, a similar term is used:

$$f(T) = \left(\frac{T_{ref}}{T_t}\right)^{\beta} \quad (9)$$

The exponent (β) drives the temperature relationship and is reliant on the battery chemistry and the physical specifications of the battery. In this form, β will provide an indication of how well the battery responds to thermal changes on either side of the reference temperature. Based on the work by Gao et. al. (Figure 1), the temperature-capacity relationship for lithium-Ion cells appears to be reasonably linear for higher temperatures, but it is non-linear at lower temperatures. Furthermore, Buchmann

explains that this relationship can be approximated as linear [1] and Gold states that the relationship is non-linear throughout the entire operating range [35].

Since these formulations are dimensionless and the capacity removed from the battery at time t is in *ampere-hours*, a constant (γ) in *ampere-hours* relates the capacity removed to the non-dimensional discharge current and temperature components. As a result, the final form for instantaneous capacity removed is:

$$\Delta C_r = \gamma \cdot \left(\frac{I_t}{I_{ref}}\right)^{\alpha} \cdot \left(\frac{T_{ref}}{T_t}\right)^{\beta} \quad (10)$$

This equation illustrates from a physical standpoint that, as the discharge current increases, the effective capacity removed will increase. This correlation is in accordance with the commonly used Peukert equation reasoning. However, the model now demonstrates that, as the temperature of the battery decreases, the effective capacity removed also increases. The literature in this area illustrates this relationship; however, the exact order of the correlation is debatable and requires verification experimentally.

3. Experimental Work

Electric drive vehicles undergo relatively dynamic operating situations in which the discharge current and operating conditions can change dramatically over the course of a cycle. From an application standpoint, electrified vehicles would be a primary benefactor of an improved battery capacity model. The typically limited onboard computing abilities associated with vehicular computing would benefit from a model with low memory and processing requirements. Due to the status of lithium based battery technology, this study investigates testing of this chemistry in various forms of

automotive grade battery packaging [1, 37, 38]. In specific, this effort tests the following chemistries, cell designs, and manufacturer-specified 20-hr capacities:

- CALB NSA 100 Lithium Iron Phosphate ($LiFePO_4$), 100Ah prismatic cell
- ThunderSky LFP90 Lithium Iron Phosphate ($LiFePO_4$), 90Ah prismatic cell
- Headway 38140S Lithium Iron Phosphate ($LiFePO_4$), 100Ah cylindrical cell package (1S10P)
- Kokam SLPB96255255 Lithium Polymer (LiPO), 60Ah pouch cell

The cells chosen provide the ability to investigate the effects of the cell design, specific chemistry, and nominal capacity on overall cell performance. While all cells are representative of typical automotive batteries, the physical design varies from cell to cell, most noticeably in weight and surface area as seen in Table 1.

Table 1: Physical specifications of investigated automotive grade lithium battery cells.

Manufacturer & Chemistry	Surface Area [cm^2]	Mass [g]
CALB $LiFePO_4$	1098	3256
ThunderSky $LiFePO_4$	1040	3018
Headway $LiFePO_4$	1433	3700
Kokam LiPO	1445	1301

Tests are run for over two cells of each type in order to account for the possibility of individual cell performance variation. Moreover, in order to capture the effects of varying current and temperature, the following test conditions are used:

- $0.5C$ discharge current at chilled, room, and hot conditions
- $1.0C$ discharge current at chilled, room, and hot conditions
- $3.0C$ discharge current at chilled, room, and hot conditions

with the discharge current ratings (C-ratings) based on the manufacturer specified 20-hr capacity that will be discussed later in more depth. These conditions are representative of the operating ranges typically provided by cell manufacturers and provide a normalized approach to discharged currents with varying cell capacity. The given testing matrix effectively tests four unique lithium based battery designs against nine separate test criteria.

Cells are electrically loaded using a custom-built resistive load bank presented in Figure 2. The load bank consists of five resistors (300-Watt Power Series from Milwaukee Resistor) wired in parallel with the ability to add each one individually using knife switches.

Figure 2: Variable resistive load bank constructed to discharge batteries under adjustable currents.

When applied to a 3.3-volt cell, this provides for the ability to test various currents from 6-330 amps over the resistor range of 0.01 to 0.5 ohm. As a result, this resistive load bank provides a variable loading experiment by virtue of Ohm's Law:

$I = \frac{V}{R}$	(11)

where V is the cell voltage and R is the resistance of the setup employed during the test.

Due to the high accuracy (> 99%) and excellent thermal capabilities ($\leq 3x10^{-6}\,\Omega/°C$) of the resistors, the applied resistance remains relatively constant throughout the duration of the test. As a result, when the battery voltage drops under load, the applied current additionally drops providing a dynamically varying loading situation which Peukert's equation cannot handle. This aspect requires that the proposed model account for a varying current in order to predict the battery SOC accurately at any point during the discharge cycle.

It is important to note that use of constant resistive loads makes defining the discharge currents relative to the nominal manufacturer capacity of the cells difficult. As expressed via Ohm's law, when the voltage of the cell drops due to loading, the current draw through the resistive load bank also decreases. This makes it problematic to apply the exact resistance that will result in a $0.5C$, $1C$, or $3C$ average load since the process of choosing the appropriate resistor would be circular (as the resistance changes, the current also changes; therefore, this changes the voltage drop under load requiring another resistor change) and the load will change throughout the course of the test. To maintain simplicity, the authors chose specific resistances for the $0.5C$, $1C$, and $3C$ loads that apply the desired load under open-circuit voltage conditions assuming no voltage drop when loaded. While this does not result in true $0.5C$, $1C$, and $3C$ loads, it maintains relative discharge criteria consistent for all of the cells.

Chilled testing occurs by placing the battery in a small medical grade freezer (Summit FS20L7) while allowing it to soak overnight to approximately -20°C. This is typically the lower operating limit of most lithium cells, as well as the lower limit of the

freezer. The freezer door includes contact terminals in order to allow for connection of the load bank and voltage sensors without compromising the enclosure seal (Figure 3):

Figure 3: Cold chamber picture of CALB 90Ah prismatic battery inside chamber and connections on outside of chamber.

The battery remains in the freezer with the compressor running for the entire duration of the test. As the test progresses, the battery temperature increases due to ohmic heating, heat generation due to entropy change, phase change, heat capacity change, and other phenomena [39]. A portion of this heat generation transfers convectively to the environment raising the temperature of the test chamber. This functionality allows the test to be performed using dynamically changing temperature similar to that of a real would situation. From a vehicular application standpoint, this test is representative of the battery pack initially cold soaked from being parked outside for

the evening with subsequent self-heating as the driver starts and completes his or her route.

To perform heated testing, the battery is placed in a fiberglass insulated, electrical enclosure with a TEMPCO EHT00038 500-watt enclosure heater (Figure 4). The heater is equipped with a thermostat that allows the internal temperature to cycle between 37°C and 41°C. As the test progresses, the battery not only experiences the cyclic temperature changes due to the thermostat's characteristics, but also sees the magnitude of these cycles increasing due to heat released by the battery. Similar to the chilled testing, this allows the test to be performed using dynamically changing temperature similar to that of a real would situation. Figure 5 provides example temperature profiles for the heated and chilled test chambers. Finally, ambient temperature testing is performed at roughly 25°C in an open-air environment. Thermal changes for this test are simply a result of the battery temperature rise due to loading conditions.

Figure 4: Heated test enclosure with ThunderSky 90Ah prismatic cell.

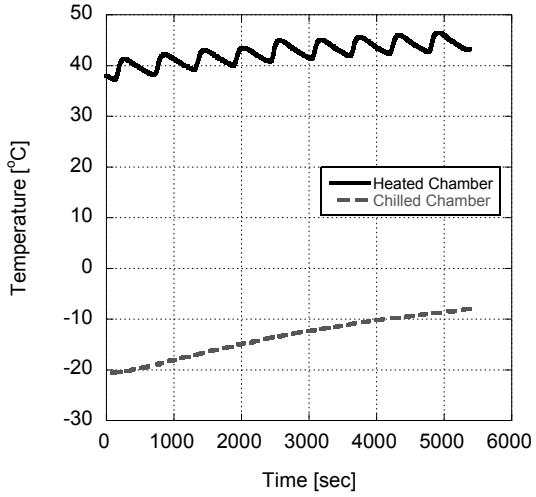

Figure 5: Example test profiles for the chilled and heated chambers.

This work utilizes a Vencon UBA-5 commercial battery analyzer for capture of experimental test data. The UBA-5 operates via a personal computer while monitoring and logging the results of the test at one-second intervals. Voltage measurement accuracy is in thousandths of a volt and acts as the termination criteria for the test at the manufacturer-specified low voltage cutoff of the battery. Results files containing the entire test data are output as comma separated values (CSV) format for input into data analysis programs. Each of the cells tested utilize a custom-built battery analysis routine in order to ensure proper test termination. Battery analysis routines (BARs) are set up using graphical representations of the testing algorithm applied by the UBA-5. These algorithms produce the necessary commands for the UBA-5 throughout the progression of a test based on a variety of set parameters and limits (Figure 6).

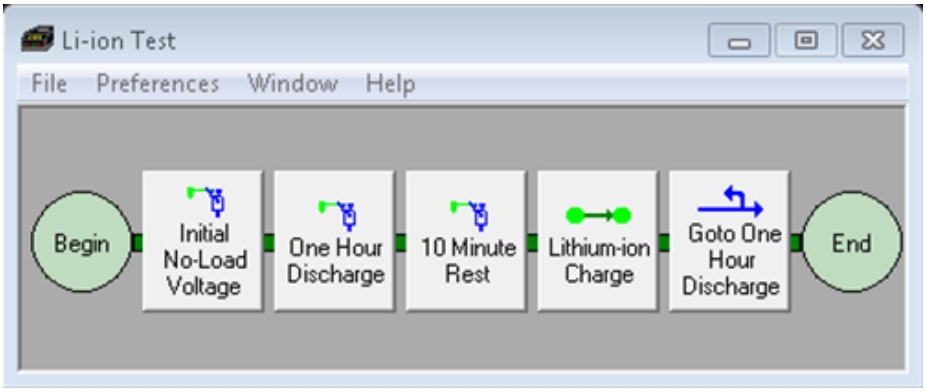

Figure 6: Sample battery analysis routine (BAR) graphical representation for Vencon UBA-5.

For this study, simplistic battery analysis routines were set up using only discharge criteria with the appropriate low-voltage cutoff (Table 2). This allows the UBA-5 to begin collecting data as soon as the test is started by the user and automatically terminates the load and data collection once the termination criteria is reached. Specific BARs are created for each cell type by changing the test termination condition in the default lithium discharge BAR. While the UBA-5 is capable of charging the cells after test completion, this is performed using separate chargers (discussed later) to free up the UBA-5 for additional testing.

Monitoring of temperature data transpires via two calibrated Philips SN74LS04 model thermistors and is time-aligned at the same time stamps as all battery performance data. In its commercially available form, the UBA-5 only allows temperature monitoring above 0°C. While the thermistors are capable of monitoring down to -30°C, Vencon calibrates their range using a specified pull down resistor for temperatures varying from 0°C to 100°C in order to maintain linearity between voltage and temperature. With the technical assistance of Vencon [40], this pull down resistor was replaced with the appropriate resistor that allows one of the thermistors to be used

at temperatures as low as -30°C. This required changing the required UBA-5 calibration file in order to match the new resistance value. The remaining thermistor kept its original configuration for the room and elevated temperature tests.

The direct current measuring capabilities of the UBA-5 are limited to three amps per channel. In order to measure higher current values accurately, a Tamura model L03S300 hall-effect current transducer is used. This current transducer outputs the system current to one of the 0-5 volt analog inputs on the UBA-5 device. This conversion occurs in the data analysis script in order to refer the voltage readings back to the corresponding current draw.

Table 2: Voltage operational limits of the investigated cells as specified by the manufacturer.

Manufacturer & Chemistry	Low Voltage Cut-off [V]	Upper Voltage Limit [V]
CALB $LiFePO_4$	2.50	3.60
ThunderSky $LiFePO_4$	2.50	4.25
Headway $LiFePO_4$	2.00	4.65
Kokam LiPO	2.70	4.20

After testing, the battery returns to room temperature and is subsequently charged according to manufacturer's specifications using an intelligent charger in order to ensure appropriate and consistent charging conditions. A Venom model 0660 charger is used and it allows for charging multiple cell chemistries using a constant-current, constant-voltage algorithm. This permits unattended charging while ensuring fully charged cells without overcharging. Table 2 lists the upper and lower voltages used for testing and charging.

4. Results and Discussion

After collecting the data, the results are compiled and analyzed using MATLAB. Recording of data signals happens at a 1-Hertz rate with the exception of current that was limited to 0.25 hertz because of the update rate of the Hall-effect current sensor. In order to ensure the data is aligned properly and to reduce the noise effects of the signals, a 1-D digital filter is applied using MATLAB (from MATLAB manual: direct form II transposed implementation of standard difference equation [41]). Use of the filter outside of an iterative loop allows for a running average of the data set along with estimation of the pack current on a per second basis. Moreover, while the intent was to test all cells at three temperature conditions for all discharge profiles, the performance of all four cells prohibited testing under cold, 3C discharge conditions. In this case, when the cell was loaded, its voltage dropped below the low-voltage cut-off of the respective cell. As a result, the authors did not perform these tests in order to prevent cell damage.

The basic principle of the proposed model is the ability to calculate capacity effects for varying temperature and current during the discharge cycle of a battery. As an example of the dynamic conditions the cells encounter during testing, the current and temperature for all eight individual tests of Headway cell #1 are provided in Figure 7. Moreover, in an effort to expand upon the basic Peukert model, the proposed model must capture the effects of temperature on the available capacity of the cell. Figure 8 demonstrates the effects of cell temperature on discharge capacity.

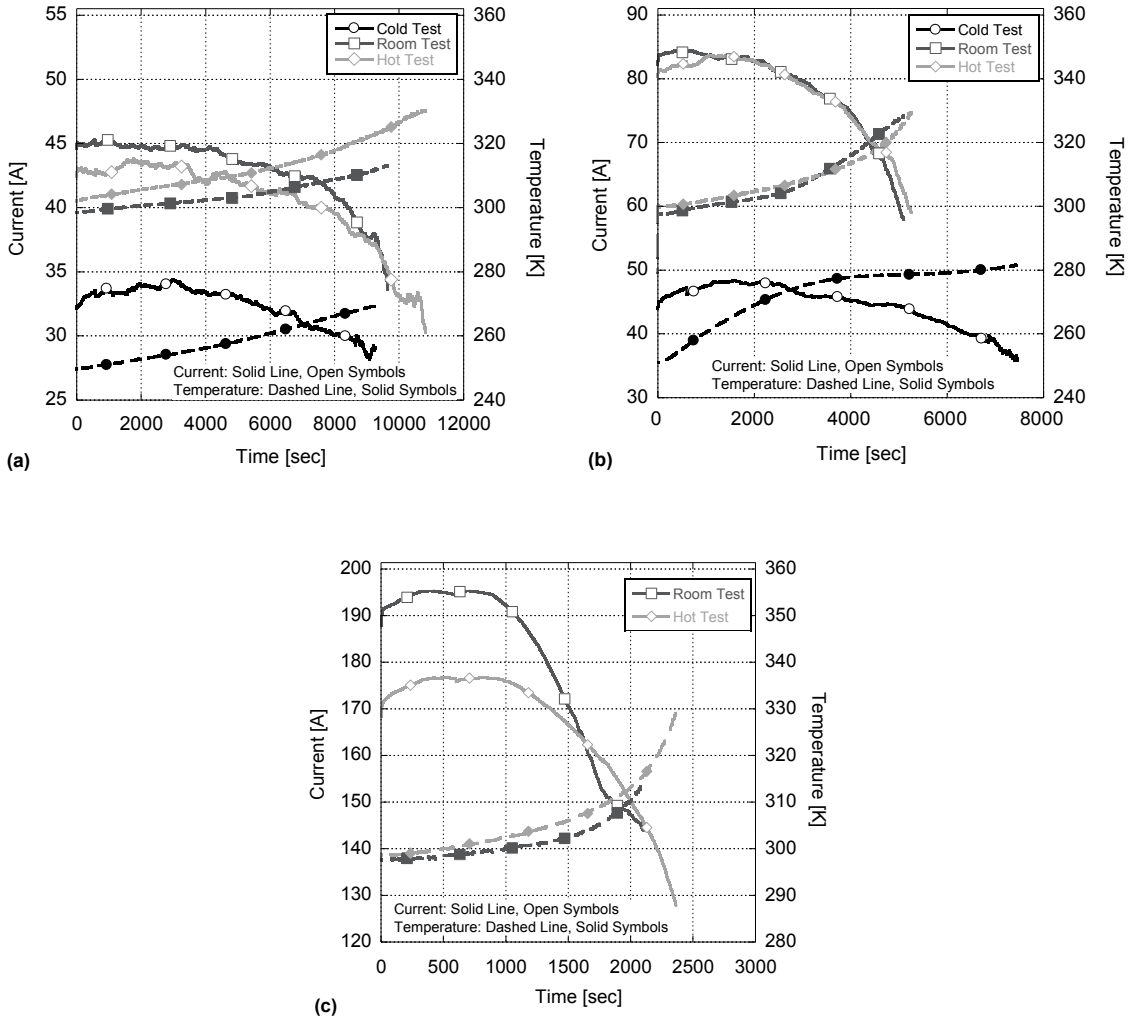

Figure 7: Headway cell #1 dynamic current and temperature profiles for a) 0.5C, b) 1C, and c) 3C discharge rates.

Grouping of data in Figure 8 with respect to the loading conditions helps to emphasize the temperature effects upon discharging. Note that normalized total capacity is a measure of the available capacity over manufacturer specifications given the particular discharge conditions; e.g., 110% for the Kokam cells would indicate that the battery has an effective capacity of 66 ampere-hours during the defined experiment. As the average temperature of the cell increases, the total capacity of the cell also

increases. The results match theoretical expectations [1, 19, 35] and make sense physically. As the cell temperature increases, the internal resistance of the cell decreases and the chemical metabolism of the cell increases, effectively increasing the capacity of the battery [1].

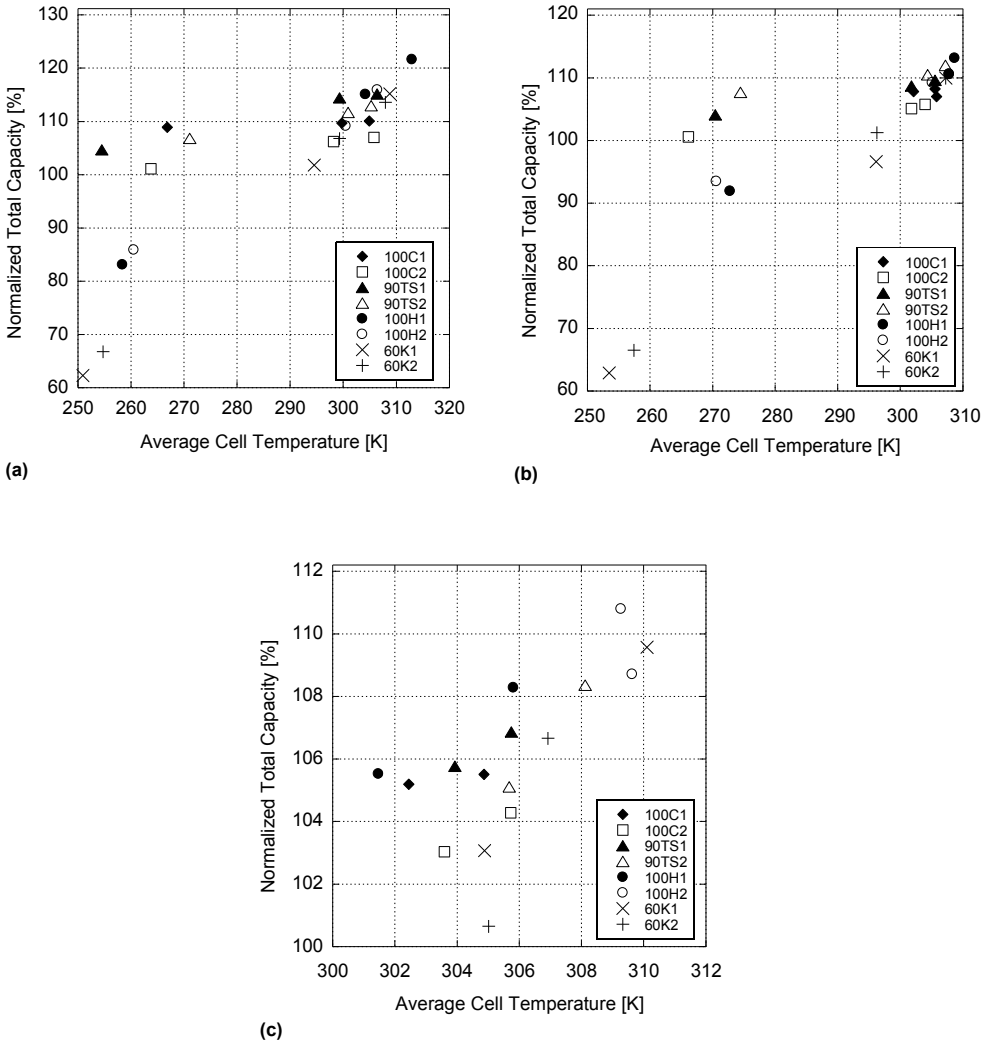

Figure 8: Normalized total capacity with respect to cell temperature for a) 0.5C, b) 1C, and c) 3C discharge rates.

Developing similar trends based on current draw proves difficult, largely due to the non-linearity and complexity of the applied testing conditions. A 0.5C test would result in a higher total capacity than a 3C test at the same temperature due to Peukert effects; however, the increase in cell temperature during the faster discharge event has the potential to outweigh this influence (recall Figure 8 where capacity goes up with temperature). This is especially true during cold chamber testing where nearly all of the cells demonstrated equal or higher total capacities at elevated discharge rates due to cell heating.

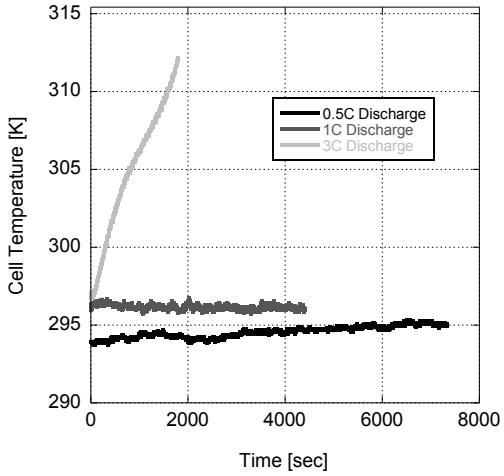

Figure 9: Kokam cell #1 battery temperature profiles under different discharge conditions during an ambient test.

As an example, Figure 9 presents the temperature profile for Kokam cell #1 as a function of discharge rate. The temperature increase due to the elevated loading during the 3C discharge offsets the negative effects of the elevated current draw, resulting in a higher discharge capacity at 3C (61.84 Ah) than at 0.5C (61.06 Ah) and 1C (57.97 Ah). Using the appropriate coefficients (covered later), the 0.5C and 1.0C discharge tests were modeled isothermally at the average temperature of the 3C test (305K). The

model predicted 66.08 Ah of discharge capacity for the 0.5C test and 63.98 Ah for the 1C test using the elevated temperature. As expected, both tests outperformed the actual 3C test, as well as the modeled 3C test (59.44 Ah).

Calculation of the actual model coefficients and exponents utilizes a constrained nonlinear optimization. This particular method utilizes a least-squares fit to compare the relative discharge curve from the test data to the discharge curve generated by the proposed model at each data point (one second intervals). For this situation, the optimization must be constrained by known bounds in order to ensure physicality of the model. For example, α is similar to the Peukert's constant and in a physical sense cannot drop below 1.0 and is rarely more than 1.5 for modern battery technology [1, 3]. Providing good initial guesses and a bound that makes sense physically reduces the chance of the optimization method settling on local, erroneous minimums. The squares of the differences between the test data and model are summed and the square root of the sum is then used as the reduction term for the optimization. This optimization is done by changing the model variables until minimizing this summation to a set tolerance (1E-6). Ideally, the optimization finds a set of coefficients and exponents that allow this value to be equal to zero.

MATLAB provides the framework for the model and optimization. MATLAB allows custom computing scripts to be created and executed utilizing a simplistic programming language with optimization toolboxes available to perform the needed analysis. The specific routine utilized for optimization in MATLAB involves the Gauss-Newton method in order to minimize the resulting final value of the function. Other methods are acceptable; however, since the Gauss-Newton method does not require

the calculation of the second derivatives of the function, choice of this routine retains computational efficiency.

The authors first employed the model with a constant α and allowed the optimization routine to find γ, β, and C_r^0. Since α is known to a rough approximation (~1.03) for lithium batteries, holding it initially constant allows the optimization procedure to focus on the unknowns. This method provides an estimate of the magnitude of γ, β, and C_r^0 for the proposed model. The results of this initial iteration indicated a γ near one with a value of C_r^0 typically between 110-120% of the nominal capacity. From a physical standpoint, this is reasonable since γ is used to relate the model to the test data at a current draw relative to one ampere (I_{ref}) and a temperature relative to 298K (T_{ref}). Ignoring the effects of β, the equation effectively becomes Peukert's equation (with I_{ref} = one). The work presented here allows for some adaptation by not requiring that γ be equal to one as Peukert specifies. However, by initially setting γ equal to one, the optimization can effectively move in the right direction reducing the possibilities of local minimums and finding physical values for the other coefficients. The initial test results also reveal that the actual capacity of the cells was rarely more than 120% of nominal, indicating a C_r^0 near 120%. This optimization occurs over both cells of each type in the same optimization in order to create a set of coefficients for a particular battery type as opposed to a set of coefficients that only matches a single, specific cell.

Table 3: Model optimization results with constant γ (1 Ah), and C_r^0 (120%) in order to increase proper physical representation.

	CALB $LiFePO_4$	ThunderSky $LiFePO_4$	Headway $LiFePO_4$	Kokam LiPO
α	1.027	1.021	1.023	1.043
β	0.324	0.440	1.720	2.910

Table 4: Model optimization results for all four coefficients.

	CALB $LiFePO_4$	ThunderSky $LiFePO_4$	Headway $LiFePO_4$	Kokam LiPO
α	1.0269	1.0213	1.0287	1.0486
β	0.3072	0.4393	1.7809	2.9988
γ	1.0032	1.0047	1.0193	1.0259
C_r^0	119.80%	121.95%	126.04%	127.33%

Utilizing the results from this method as initial values, γ is set to one Ah and C_r^0 equal to 120% of the nominal cell capacity. This systematic approach removes some of the flexibility of a four-variable optimization and reduces the likelihood of the optimization producing a non-physically based curve-fit. Table 3 presents the results from this optimization. Using these results as initial guesses, optimization of all four variables is done in order to find the best fit possible with the results given in Table 4.

To investigate the overall accuracy of the model, the deviations between predicted SOC for the model and actual experiment were calculated. Figure 10 illustrates the *maximum* deviation seen in the actual SOC to the model, along with the *average* difference in SOC. Representation of the plots in this manner illustrates results from all tests in an easy to digest format. The model provides close agreement with the experimental test results with all outcomes within 95% of the actual tested values. In addition, more than 80% of the tests are within 97% of the test data. Further testing to provide average discharge profiles would help refine the data; however, due to the capacity of the cells under investigation, it took six months to complete the study as-is. Future work will explore average profiles and the resultant standard deviations in the experimental tests.

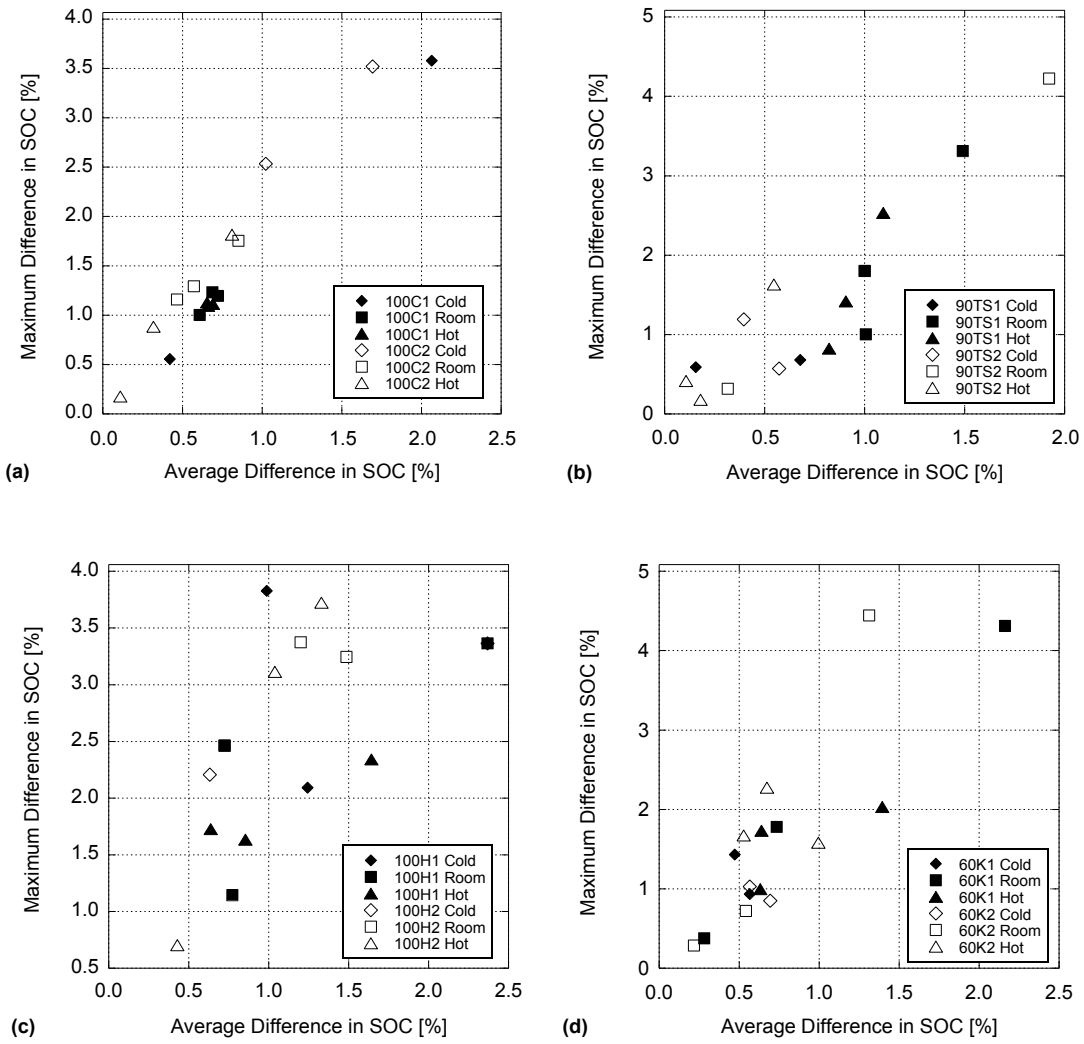

Figure 10: Average and maximum model accuracy with respect to SOC for a) CALB, b) ThunderSky, c) Headway, and d) Kokam cells.

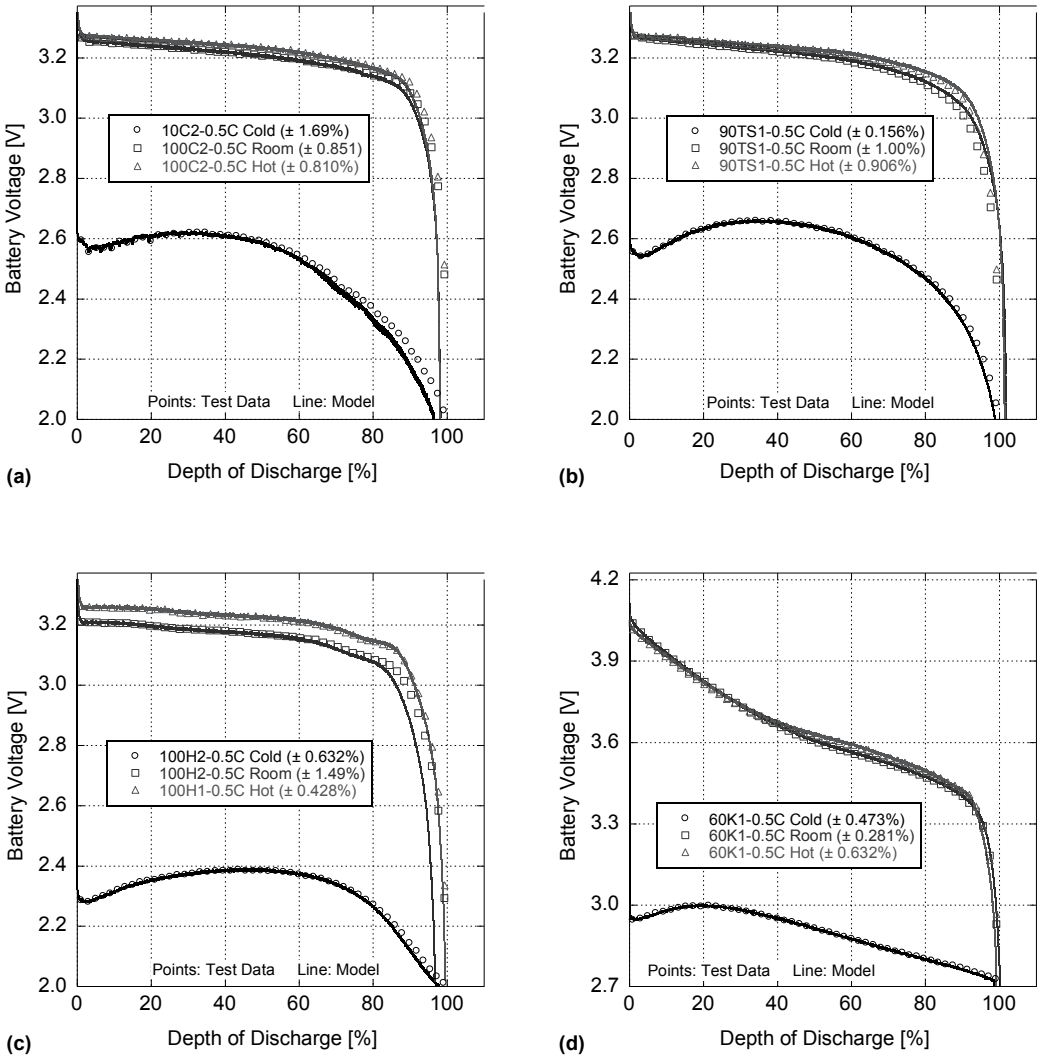

Figure 11: 0.5C Discharge profiles with average depth of discharge error indicated for a) CALB, b) ThunderSky, c) Headway, and d) Kokam.

By demonstrating the voltage and depth of discharge relationship for each of the tested cell types at the 0.5C discharge rate (Figure 11), it becomes clear that the model accurately simulates the absolute depth of discharge (DOD) across a wide variety of operating temperatures for all of the investigated cell types. When comparing the two most similar cells, CALB and ThunderSky, the CALB cells outperform the ThunderSky cells in temperature performance by a fair margin. This is to be expected as CALB was

developed as a sister company of ThunderSky for use as a Chinese aviation lithium battery and is held to higher performance standards [42]. These standards may be the underlying reason for the CALB cells demonstrating some of the most desirable temperature and current coefficients (low β and γ respectively) of all the cells tested as well. Given the same discharge criteria and battery capacity, the cell design with the lower β and γ will result in the longest discharge time.

The Kokam pouch cells exhibit the highest increase over the manufacturers specified nominal capacity; however, these cells have the largest temperature and current coefficients of all cells tested, outweighing this benefit. This illustrates that care should be taken when performing the testing in order to ensure the battery pack design is in “end use” form as the temperature coefficient is likely dependent on the physical cell design. Due to chemistry and nominal capacity, the Kokam cells demonstrated the lowest mass and highest surface areas of all the cells tested and, as a result, environmental changes influenced these cells the most. The Headway multiple cell configuration is also the likely cause of the higher temperature coefficients value as there is a large amount of surface area between the individual cells (Figure 12).

Figure 12: Cells under Investigation (from left to right) CALB 100Ah, ThunderSky 90Ah, Headway 10P1S 100Ah Pack (front), Kokam 60Ah

The test data and resulting correlations indicate battery temperature performance is not only a function of cell chemistry, but physical specifications and pack configurations as well. The model effectively captures the physical battery chemistry and the environmental effects on the overall cell design. The result is a real world battery model based on fundamental, physical relationships capable of configuration by manufacturers and system-builders alike for multiple pack designs. With that in mind, future work should involve studying the use of multiple cells in closely packed configurations to explore the effect of cell density on temperature performance.

5. Conclusion

The evolution of battery technology requires a numerically efficient method to predict correctly the remaining State of Charge of batteries at any point during a discharge cycle utilizing a minimal data set. Historically, this is accomplished through a combination of Coulomb counting and open-circuit voltage profile interpolation

algorithms. These methods make quantifying cell temperature effects difficult or non-existent.

This paper demonstrates an intuitive and comprehensive, yet high-level model that accurately predicts the remaining battery capacity to within five-percent across a wide range of operating conditions. Due to the minimal required dataset and computational simplicity, the model remains feasible for the current state-of-the-art battery technology, as well as for integration within battery management systems. The test methods presented provide a straightforward and economical approach to capturing the required data set and allow future work to investigate the effects of battery pack configurations, as well as various thermal management methods.

Acknowledgments

This work was supported by Smith Electric Vehicles and the University of Kansas Transportation Research Institute [grant number IND 0066912].

References

1. Buchmann, I., *Batteries in a portable world*2001: Cadex Electronics.
2. Peukert, W., *On the dependency of the discharge capacity versus discharge rate for lead-acid batteries.* Elektrotechnische Zeitschrift, 1897. **20**: p. 20-21.
3. Linden, D. and T.B. Reddy, *Handbook of Batteries (3rd Edition)*, 2002, McGraw-Hill.
4. Pavlov, D. and G. Petkova, *Phenomena That Limit the Capacity of the Positive Lead Acid Battery Plates.* Journal of the Electrochemical Society, 2002. **149**(5): p. A654.
5. Doerffel, D. and S.A. Sharkh, *A critical review of using the Peukert equation for determining the remaining capacity of lead-acid and lithium-ion batteries.* Journal of power sources, 2006. **155**(2): p. 395-400.
6. Rakhmatov, D., S. Vrudhula, and D.A. Wallach, *A model for battery lifetime analysis for organizing applications on a pocket computer.* Very Large Scale Integration (VLSI) Systems, IEEE Transactions on, 2003. **11**(6): p. 1019-1030.
7. Rakhmatov, D., S. Vrudhula, and D.A. Wallach. *Battery lifetime prediction for energy-aware computing*. in *Proceedings of the 2002 International Symposium on Low Power Electronics and Design*. 2002.
8. Rakhmatov, D., S. Vrudhula, and D.A. Wallach, *A model for battery lifetime analysis for organizing applications on a pocket computer.* IEEE Transactions on Very Large Scale Integration (VLSI) Systems, 2003. **11**(6): p. 1019-1030.
9. Doyle, M., J. Newman, and J. Reimers, *A quick method of measuring the capacity versus discharge rate for a dual lithium-ion insertion cell undergoing cycling.* Journal of power sources, 1994. **52**(2): p. 211-216.
10. Linden, D. and T. Reddy, *Handbook of Batteries, 2002*, McGraw-Hill.
11. Johnson, V., *Battery performance models in ADVISOR.* Journal of power sources, 2002. **110**(2): p. 321-329.
12. Ying, R.Y., *State of charge algorithm for lead-acid battery in a hybrid electric vehicle*, 2003, US Patent 6646419.
13. Bumby, J., P. Clarke, and I. Forster, *Computer modelling of the automotive energy requirements for internal combustion engine and battery electric-powered vehicles.* Physical Science, Measurement and Instrumentation, Management and Education-Reviews, IEE Proceedings A, 1985. **132**(5): p. 265-279.
14. Proctor, R.L., et al., *Accurate battery state-of-charge monitoring and indicating apparatus and method*, 1997, US Patent 5656919.
15. Atwater, T.B., *Resettable state-of-charge indicator for rechargeable batteries*, 1997, US Patent 5640150.
16. Oh, J.M., et al., *Ionomer Binders Can Improve Discharge Rate Capability in Lithium-Ion Battery Cathodes.* Journal of the Electrochemical Society, 2011. **158**(2): p. A207.
17. Amatucci, G., et al., *Materials' effects on the elevated and room temperature performance of C/LiMn2O4 Li-ion batteries.* Journal of power sources, 1997. **69**(1-2): p. 11-25.
18. Rao, R., S. Vrudhula, and D.N. Rakhmatov, *Battery modeling for energy aware system design.* Computer, 2003. **36**(12): p. 77-87.

19. Gao, L., S. Liu, and R.A. Dougal, *Dynamic lithium-ion battery model for system simulation.* IEEE Transactions on Components and Packaging Technologies, 2002. **25**(3): p. 495-505.
20. Larminie, J., J. Lowry, and I. NetLibrary, *Electric vehicle technology explained* 2003: Wiley Online Library.
21. Du Pasquier, A., et al., *A comparative study of Li-ion battery, supercapacitor and nonaqueous asymmetric hybrid devices for automotive applications.* Journal of power sources, 2003. **115**(1): p. 171-178.
22. Brilmyer, G.H. and W.H. Tiedemann, *Dynamic state-of-charge indicator for a battery and method thereof*, 1989, US Patent 4876513.
23. Jossen, A., *Fundamentals of battery dynamics.* Journal of power sources, 2006. **154**(2): p. 530-538.
24. Meissner, E. and G. Richter, *The challenge to the automotive battery industry: the battery has to become an increasingly integrated component within the vehicle electric power system.* Journal of power sources, 2005. **144**(2): p. 438-460.
25. Lahiri, K., et al. *Battery-driven system design: A new frontier in low power design*. in *Design Automation Conference, 15th International Conference on VLSI Design* 2002. IEEE Computer Society.
26. Song, L. and J.W. Evans, *Electrochemical-thermal model of lithium polymer batteries.* Journal of the Electrochemical Society, 2000. **147**(6): p. 2086.
27. Doyle, M., T.F. Fuller, and J. Newman, *Modeling of galvanostatic charge and discharge of the lithium/polymer/insertion cell.* Journal of the Electrochemical Society, 1993. **140**: p. 1526.
28. Fuller, T.F., M. Doyle, and J. Newman, *Relaxation Phenomena in Lithium-Ion-Insertion Cells.* Journal of the Electrochemical Society, 1994. **141**(2): p. 982.
29. Evans, T., T. Nguyen, and R.E. White, *A mathematical model of a lithium/thionyl chloride primary cell.* Journal of the Electrochemical Society, 1989(2): p. 328.
30. Tsaur, K.C. and R. Pollard, *Mathematical modeling of the lithium, thionyl chloride static cell.* Journal of the Electrochemical Society, 1984. **131**(2): p. 975.
31. Gu, W. and C. Wang, *Thermal-electrochemical modeling of battery systems.* Journal-Electrochemical Society, 2000. **147**(8): p. 2910-2922.
32. Gu, W., et al., *Computational fluid dynamics modeling of a lithium/thionyl chloride battery with electrolyte flow.* Journal of the Electrochemical Society, 2000(2): p. 427.
33. Syracuse, K.C. and W.D.K. Clark. *A statistical approach to domain performance modeling for oxyhalide primary lithium batteries*. in *Annual Battery Conference on Applications and Advances*. 1997. California State University, Long Beach, CA, USA: IEEE.
34. Pedram, M. and Q. Wu. *Design considerations for battery-powered electronics*. in *Proceedings 1999 Design Automation Conference* 1999. ACM.
35. Gold, S. *A PSPICE macromodel for lithium-ion batteries*. in *The Twelfth Annual Battery Conference on Applications and Advances* 1997. IEEE.

36. Panigrahi, T., et al. *Battery life estimation of mobile embedded systems*. in *Proceedings of the The 14th International Conference on VLSI Design* 2001. IEEE.
37. Pollet, B.G., I. Staffell, and J.L. Shang, *Current Status of Hybrid, Battery and Fuel Cell Electric Vehicles: from Electrochemistry to Market Prospects.* Electrochimica Acta, 2012: p. Corrected proof. Volume / Issue / Pages Not Yet Available.
38. Anderson, D.L., *An Evaluation of current and future costs for lithium-ion batteries for use in electrified vehicle powertrains*, 2009, Duke University.
39. *Test of Li-ion Battery for Self-heating & Lifetime Evaluation*, 2010, Tsinghua University: http://www.transportation.anl.gov.
40. Venis, M., *Via Electronic Mail*, November 2011, marc@vencon.com.
41. Oppenheim, A.V., R.W. Schafer, and J.R. Buck, *Discrete-time signal processing*. Vol. 2. 1989: Prentice hall Upper Saddle River.
42. Kriss, E., *Chinese Battery Manufacturing* 2011: Fair Isle Press. 10.

CHAPTER 4: An Advanced Electric Vehicle Duty Cycle Simulation Model Derived from Newton's Second Law of Motion

Austin Hausmann[2] and Christopher Depcik

Department of Mechanical Engineering - University of Kansas, Lawrence, Kansas (United States)

Abstract

In order to provide students and researchers at the University of Kansas with a vehicle dynamics tool for electric drive vehicles, this chapter describes an advanced numerical model. This work demonstrates the physical and mathematical theories involved, as well as outlining the model flow and the necessary algorithms. Moreover, this chapter covers the equipment, software, and processes necessary for collecting the required data. Furthermore, a real world, on-road driving cycle provides for a quantification of accuracy. Multiple University of Kansas student project vehicles are then studied using parametric studies applicable to the operating requirements of the vehicles. Further investigation demonstrates the accuracy and trends associated with the advanced models presented in Chapters 2 and 3.

Words: 109

Nomenclature

Variable	Description	Units
a_D	Unitless aerodynamic drag coefficient	[-]
b_D	Linear velocity aerodynamic drag coefficient	[m/s]
a_{rr}	Static rolling resistance coefficient	[N]
b_{rr}	Linear velocity rolling resistance coefficient	[N/(m/s)]
d_{rr}	Quadratic velocity rolling resistance coefficient	[N/(m^2/s^2)]
$C_{20\text{-}hr}$	20-hour rate cell capacity	[amp-hours]
C_{cell}	Nominal cell capacity	[amp-hours]

[2] Corresponding author. Tel.: +1 785 840 7693; E-mail address: hausmann@ku.edu
1501 W. 15th St. 3138 Learned Hall Lawrence, KS 66045 USA

C_r	Capacity remaining	[ampere.hour]
C_D	Standard aerodynamic drag coefficient	[-]
C_{pack}	Total nominal capacity of the battery pack	[amp-hours]
CR_{batt}	Charge removed from the battery pack	[amp-hours]
D	Distance traveled	[m]
d_{tire}	Tire diameter	[m]
dt	Change in time between successive iterations	[seconds]
E_{acc}^{i}	Energy draw of single accessory	[kwh]
$\dot{i}$	Specific energy of a battery cell	[kWh/kg]
E_{cell}	Energy of a battery cell	[kWh]
E_{acc}^{i}	Energy of single accessory of course of route	[kwh]
E_{pack}	Total energy of the battery pack	[kWh]
$E_{pack}^{removed}$	Energy removed from battery pack during route	[kWh]
F_{AD}	Aerodynamic drag force	[N]
F_{GR}	Force of road gradation	[N]
F_L	Aerodynamic lift force	[N]
F_{LA}	Linear acceleration force	[N]
F_{RR}	Rolling resistance force	[N]
F_{TE}	Total tractive effort force	[N]
g	Acceleration due to gravity	[m/s^2]
G_{final}	Final drive ratio	[-]
$GVWR$	Gross vehicle weight rating	[kg]
H	Vehicle frontal height	[m]
I_{batt}^{out}	Battery current out	[amperes]
$I_{charger}$	Battery charger input current	[amperes]
I_{ref}	Reference current	[amperes]
k	Peukert's Constant	[-]
m	Vehicle mass	[kg]
m_{base}	Base mass of the vehicle	[kg]
m_{cell}	Mass of a single battery cell	[kg]
m_{pack}	Mass of the total battery pack	[kg]
$m_{passengers}$	Mass of the vehicle passengers	[kg]
$m_{payload}$	Mass of the vehicle payload	[kg]
N_{acc}	Total number of individual accessory draws	[-]

N_{gears}	Number of transmission gears	[-]
$n_{parallel}$	Number of strings in parallel	[-]
n_{series}	Number of strings in series	[-]
P_{acc}	Total instantaneous vehicle accessory power draw	[watts]
$\bar{P}_{acc}^{i}$	Average power draw of single accessory	[watts]
P_{batt}^{out}	Batter power draw	[watts]
$P_{charger}$	Battery charger power	[watts]
P_{motor}^{in}	Incoming electric motor power	[watts]
P_{motor}^{out}	Electric motor output shaft power	[watts]
P_{regen}	Regenerative braking power	[watts]
$P_{required}$	Power requirement to solve tractive force balance	[watts]
p_{tire}	Tire pressure	[kPa]
R_{batt}	Battery terminal resistance	[omhs]
r_{tire}	Tire radius	[m]
T_{batt}	Battery temperature	[K]
T_{ref}	Reference temperature	[K]
t	Time	[s]
t_{acc}^{i}	Total power draw time of single accessory	[hours]
t_{charge}^{bulk}	Battery bulk charge time	[hours]
t_{charge}^{total}	Battery total charge time	[hours]
t_{total}	Total route time	[s]
V	Absolute vehicle velocity	[m/s]
V_{batt}	Total battery pack voltage	[volts]
V_{cell}	Cell voltage	[volts]
V_{cell_nom}	Nominal cell voltage	[volts]
$V_{charger}$	Battery charger input voltage	[volts]
W	Vehicle frontal width	[m]
Z	Vertical vehicle load	[N]
α, β	Rolling resistance exponents	[-]
$\alpha_{batt}, \gamma_{batt}$	Current coefficients	[-]
β_{batt}	Temperature coefficient	[-]
$\eta_{charger}$	Battery charger efficiency	[-]
η_{motor}	Electric motor efficiency	[-]

$\eta_{transmission}$	Transmission mechanical efficiency	[-]
μ_{RR}	Standard coefficient of rolling resistance	[-]
Ω	Rotational speed of motor	[rad/s]
ρ	Density of air	[kg/m^3]
τ_{motor}	Motor torque	[N.m]
θ	Road gradation angle	[deg]
θ_{regen}	Regenerative braking ratio	[-]

1. Introduction

Recent legislation by the Environmental Protection Agency (EPA), California Air Resources Board (CARB), and other emission regulatory commissions require that automotive manufacturers must reduce exhaust emissions to miniscule levels. Meeting these requirements is becoming increasingly difficult for traditional internal combustion engine (ICE) technologies. Compounding this problem is the difficulty in meeting these standards while simultaneously maintaining the performance and fuel consumption expectations of consumers. These pollution concerns coupled with ever-rising oil prices has led many companies to investigate the use of electric drive components to increase efficiency and lessen emissions. Electric drive vehicles are defined as any vehicle that "*use one or more electric motors or traction motors for propulsion*" [1]. For full-scale deployment of electric drive vehicles, many key vehicle logistical parameters require examination including, but not limited to driving range requirements, charging times, and on-road vehicle performance. One of the most common reluctances towards purchasing electric vehicles is their limited range. Consumers are often worried if they will have the range required to complete their daily driving and what they will do if the battery pack starts to run low, often known as range anxiety [2].

Of particular interest to the authors is the performance associated with two student-built electric drive vehicle projects at the University of Kansas (KU). The first of which is a 1974 Volkswagen Super-Beetle converted to a plug-in series hybrid. The vehicle utilizes an onboard biodiesel generator in order to aid in the charging of a 120 VDC nominal lead-acid battery pack that powers a brushed Direct Current (DC) motor. The vehicle has been road worthy since the spring of 2010 and is a research platform for multiple student projects. The second vehicle is a 1997 GMC Jimmy in the process of conversion to a full electric delivery vehicle for use by the KU Libraries in their daily delivery of materials. In order to understand and aid in the design process of both vehicles necessitates a medium for simulating the effects of various powertrain components. As a result, this work describes the formulation of a dynamic vehicle simulation model in an effort to better analyze electric drive technology, as well as aid in the design of student research projects [3-8]. In addition, this model allows investigation of the advanced models developed in the previous two chapters. This effort stands as a collection of the theoretical background, model flow, specific algorithms, validation, and performance studies associated with the model.

2. Electric Vehicle Dynamics Model

In order to aid in the design process and reduce range anxiety, this work formulates an electric vehicle dynamics model utilizing Newton's Second Law (conservation of momentum) for a constant mass object. The model includes typical physical vehicle parameters, energy flow algorithms, and improvements introduced in the previous two chapters. The model itself provides advanced methods for predicting vehicle performance while retaining the goal of relatively simplistic inputs. This allows

for simulation of virtually any conceivable route using only vehicle velocity and elevation data. At each time step, a total tractive force balance based on Newton's Second Law is calculated:

$$F_{TE} = F_{GR} + F_{AD} + F_{RR} + F_{LA} \quad (1)$$

where F_{GR} is the gradation force, F_{AD} is the aerodynamic force, F_{RR} is the rolling resistance force, and F_{LA} is the linear acceleration force (all in Newtons). The summation of these forces determines the overall magnitude and direction of the force required to produce vehicular acceleration (F_{TE}).

Calculation of the gradation force transpires using the total weight of the vehicle and the road angle (θ) in order to determine the force required to overcome the vertical change in distance:

$$F_{GR} = mg\sin\theta \quad (2)$$

where m is the vehicle mass and g is the gravitational constant. In this expression, determination of the road angle occurs geometrically:

$$\theta = \tan^{-1}\left\{\frac{\text{elevation}(t_1) - \text{elevation}(t_0)}{0.5\left[\text{velocity}(t_1) + \text{velocity}(t_0)\right](t_1 - t_0)}\right\} \quad (3)$$

where t_0 is the initial time and t_1 is the final time of the time step under investigation. This effect either decelerates the vehicle (positive grade change) or aids in the acceleration of the vehicle (negative grade change).

The aerodynamic force is a function of the air density (ρ), frontal area of the vehicle (A_f), coefficient of drag (C_D), and vehicle velocity (V). In the traditional textbook form, this equals [9]:

$$F_D = \frac{1}{2}\rho A_f C_D V^2 \quad (4)$$

If the advanced model outlined in Eqn. 8 of Chapter 2 is used, the aerodynamic force is as follows:

$$F_D = \frac{1}{2}\rho A_f \left[a_D + \frac{b_D}{V} \right] V^2 \quad (5)$$

where a_D and b_D are the calibrated coefficients described in Chapter 2. When compared to Eqn. 8 in Chapter 2, reducing model complexity occurs by removing the influence of yaw angles and wind effects. Incorporation of these parameters would involve inclusion of accelerometer data and wind measurement data from the vehicle (on-board). As discussed in Chapter 2, the differences in including these effects are relatively minimal at the cost of substantially increasing data logging and numerical analysis requirements.

The traditional form of the rolling resistance force includes the vehicle weight (mg), rolling resistance coefficient (μ_{RR}), and road angle [3]:

$$F_{RR} = \mu_{RR} mg \cos\theta \quad (6)$$

From the improved model in the second chapter (Eqn. 17), the rolling resistance force is a function of tire pressure (p_{tire}), vehicle weight, velocity, road angle, and five calibrated coefficients ($\alpha, \beta, a_{rr}, b_{rr},$ and d_{rr}):

$$F_{RR} = \left(\frac{p_{tire}}{p_{ref}} \right)^{\alpha} \left(\frac{z}{z_{ref}} \right)^{\beta} \left(a_{rr} + b_{rr} V + d_{rr} V^2 \right) \quad (7)$$

The final component of the tractive force balance is the linear acceleration force [3]:

$$F_{LA} = m\left[V(t_i) - V(t_{i-1}) \right] / dt \quad (8)$$

where $V(t_i)$ is the velocity at the current numerical step and $V(t_{i\text{-}1})$ is the vehicle velocity at the previous numerical step. This linear acceleration force is essentially Newton's

Second Law and is a function of the vehicle mass and acceleration required to match the requested velocity profile.

Conversion to the power required by the electric motor ($P_{required}$) occurs by multiplying the total tractive force by the vehicle velocity:

$$P_{required} = F_{TE} V(t) \quad (9)$$

This transformation of the force balance into an energy input allows for a more direct calculation of drivetrain power requirements. Moreover, this energy constraint is not the power output required by the battery pack, but the power applied to the rear wheels after including all driveline efficiency losses in order to accelerate the vehicle according to the input velocity.

Solving for the battery power requirement systematically happens by moving from the wheels through the driveline to the motor and finally calculating the power draw from the battery pack. First, the use of the transmission efficiency ($\eta_{transmission}$) allows for calculation of the motor output shaft power (P_{motor}^{out}) from the power required at the wheels:

$$P_{motor}^{out} = P_{required} \eta_{transmission} \quad (10)$$

Both automatic and manual transmissions typically use spur and helical gear combinations in order to either reduce or increase the output speed of the motor [10, 11]. Spur and helical gears have a power transmission efficiency of approximately 96-99% per mating pair. The losses are generally a result of fluid drag and friction on the gear contact surfaces [10, 11]. While electric vehicles do not typically use traditional transmissions [3], correct transmission design optimization could possibly lead to an increase in efficiency and range depending on the vehicle route and application [12-14].

All else being equal, as the number of gears and contact points between the gears increases, the overall efficiency of the transmission decreases.

As a result, estimation of transmission efficiency occurs using the total number of gears as a power multiplier:

$$\eta_{transmission} = 0.99^{(2+N_{gears})} \quad (11)$$

The value of two in the exponent accounts for the rear differential efficiency and N_{gears} is the number of gear combinations in the transmission. For typical electric vehicle reduction boxes, this value will be one. This method merely assumes a 99% mating efficiency taken to the power of the number of gearing combinations however; it avoids obtaining very specific information regarding the internals of the vehicle transmission. While this method is elementary, it provides a relatively accurate method for estimating transmission efficiency while maintaining computational speed. In order to improve this method further entails a dynamic transmission efficiency model based on the rotational speed and physical design of each gear.

Calculation of the motor torque required (τ_{motor}) then follows using the motor output shaft power divided by the motor speed:

$$\tau_{motor} = P_{motor}^{out} / \Omega \quad (12)$$

where Ω is the rotational speed of the motor in radians per second calculated from the vehicle speed:

$$\Omega = 60\pi G_{final} V(t) / d_{tire} \quad (13)$$

where 60 is used to convert the rotational velocity from radians per second to rotations per minute and G_{final} is the final drive ratio of the vehicle. At this point, if the rotational speed of the motor or the requested torque exceeds the limiting values specified by the

manufacturer, the values are set to their limits with subsequent recalculation of the force balance.

Determination of motor efficiency (η_{motor}) then occurs by means of a look-up map using the torque and rotational speed of the motor (this process will be covered in more detail later). Use of this value in conjunction with the motor output shaft power allows for computation of the incoming motor power requirement:

$$P_{motor}^{in} = P_{motor}^{out} / \eta_{motor} \quad (14)$$

In other words, there is an efficiency loss across the motor that relates the power input to the motor to the actual power delivered by the motor.

Furthermore, the total battery power draw requirement $\left(P_{batt}^{out}\right)$ is now a function of this input motor power requirement and the total power draw of all the vehicle accessories (P_{acc}):

$$P_{batt}^{out} = P_{motor}^{in} + P_{acc} \quad (15)$$

The power draw for these accessories, such as air conditioning and the auxiliary 12-volt system, is presented later in this chapter.

Determination of the current draw from the battery pack requires knowledge of the battery pack voltage. In order to initialize the simulation, the first numerical time step utilizes the pack voltage at the initial State of Charge (SOC). After computing the voltage and battery power draw, the fundamental power equation allows for determination of the battery current draw. Moreover, in order to provide for a more physical representation of actual battery usage, battery internal resistance effects are integrated [3]:

$$P_{batt}^{out} = V_{batt} I_{batt}^{out} - 2R_{batt}\left(I_{batt}^{out}\right)^2 \quad (17)$$

where V_{batt} is the pack voltage and I_{batt}^{out} is the current draw coming from the batteries. The value of two in the above equation accounts for the resistance (R_{batt}) through each battery terminal (e.g., one positive and one negative).

Rearrangement of the terms leads to a quadratic formula representing the current draw of the battery with respect to the battery voltage, internal resistance, and power draw:

$$I_{batt}^{out} = \frac{V_{batt} - \sqrt{\left(V_{batt}\right)^2 - 8\left(R_{batt}P_{batt}^{out}\right)}}{4\left(R_{batt}\right)} \quad (18)$$

This current draw allows for calculation of the voltage drop of the battery pack under load for the next time step (covered later in this chapter).

Electric motor control units often use current and power limiting in order to protect the power source and electric motor from excessive energy draws [3, 14, 15]. In order to account for this, the motor controller often includes an adjustable constant current limit (e.g., maximum current allowed). Hence, the model incorporates a user defined current limit that checks against the current calculated in Eqn. (18). If the calculated current is greater than the defined current limit, the current draw at the time step under calculation in the simulation is then set to the limit value.

It is important to note that since calculation of the motor power occurs from the specified acceleration in the input file (e.g., KU Libraries ICE vehicle test) it may require a current draw beyond the current limit. Hence, this necessitates a recalculation of the motor power and vehicle acceleration in order to account for the implemented current draw limit. This is done using an iterative loop that reduces the velocity of the vehicle in small steps (0.1 m/s increments) until the current requirement that is needed to match this velocity is equal to the current draw limit. Furthermore, calculation of a new force balance happens at each step of the iterative loop using this new velocity estimate.

Hence, it is possible that the electrified drivetrain cannot match the intended driving profile.

If the required current draw of the vehicle is negative due to vehicle deceleration, regenerative braking may be available. During deceleration, the kinetic energy of the vehicle is traditionally dissipated through heat via the friction braking system [3, 10]. Electric vehicles provide for the use of regenerative braking by reversing the polarity of the electric drive motor, effectively turning the motor into a generator. While this is an inherently inefficient design, since it is operating a motor as a generator, it allows for some of the wasted energy to be recovered, converted into electric current, and directed back into the battery pack [3, 16-18].

While numerous models exist for regenerative braking [3, 16, 17, 19, 20], many of these models involve exact measurements along with detailed, low-level information regarding the design of the electric motor [4, 6-8, 21]. The work presented here uses a first-order approximation for regenerative braking similar to the work of Larminie and Lowry [3]. Reversing the sign on the current flow and approximating the cell impedance as double the impedance under current draw conditions allows for the model to transfer a fraction of the force balance energy back to the total energy remaining in the battery pack.

$P_{regen} = \theta_{regen} F_{TE} V(t)$	(19)

The internal resistance of the cell is typically different under charging and discharging conditions as a battery is more reluctant to take a charge than deliver a charge. A good first-order estimation for this effect is to simply double the internal cell resistance under conditions in which current is flowing into the battery [3]. In Eqn. (19),

the regenerative braking ratio (θ_{regen}) is the percentage of the overall deceleration or braking force accounted for by the regenerative braking process [3]. This ratio varies from 0.05 to as high as 0.45 and is dependent on the actual motor design and efficiency. Generally, 0.3 is widely accepted as a good average value [3]. Moreover, it is important to mention that this pack charging process only occurs when the force required to move the vehicle becomes negative (deceleration) in the simulation.

Furthermore, manufacturers often limit the magnitude of the regenerative current within the programming of the controller. This is because instantaneous currents can become quite large and damage the electronics inside the controller [15, 22, 23]. In order to account for this, similar to maximum current drawn from the vehicle battery pack, a limiting regeneration current variable is included. Hence, this limits the current as computed from the regenerative braking power. Moreover, in order to prevent overcharging the battery from the regenerative braking process, pack charging only occurs when the battery SOC is less than 95%. In reality, this process is handled by the motor controller and the pack SOC charging limit is set up by the manufacturer [15, 22, 23].

Determination of the final current draw now allows for calculation of the charge removed (CR) from the battery pack. Using the traditional battery model as discussed in Chapter 3, the charge removed is merely a function of the current draw, the Peukert coefficient (k), and the time conversion of the current draw:

$$CR_{batt}(t) = CR_{batt}(t-1) + \left[\frac{I_{ref}\left(I_{batt}^{out}/I_{ref}\right)^{k}}{\left(3600/dt\right)} \right] \quad (20)$$

where 3600 is used to convert the discharge capacity from amp-seconds to amp-hours and dt is the time step of the model in seconds. This is similar to the Coulomb counting method mentioned in Chapter 3 with the addition of the Peukert constant (k) to account for the intrinsic cell losses.

Using the improved model from the previous chapter (Eqn. 10), the current draw becomes a function of the current, battery temperature, and the three calibrated coefficients of γ, α_{batt} and β_{batt}:

$$CR_{batt}(t) = CR_{batt}(t-1) + \gamma\left(\frac{I_{batt}^{out}}{I_{ref}}\right)^{\alpha_{batt}}\left(\frac{T_{ref}}{T_{batt}}\right)^{\beta_{batt}} \quad (21)$$

where I_{ref} and T_{ref} are the reference current (1 amp) and temperature (298K) values respectively and T_{batt} is the battery pack temperature.

Then, tracking the charge removed over the course of the simulation allows for determination of the SOC of the battery pack at each time step:

$$\mathrm{SOC}(t) = 1 - \frac{CR_{batt}(t)}{C_{total}} \quad (22)$$

Note that if the more simple is used, the capacity is the Peukert capacity:

$$C_{total} = \left[\left(C_{20-hr}/20\right)^{k}\right]20 \quad (23)$$

where $C_{20\text{-}hr}$ is the typical 20-hour capacity specified by the battery manufacturer. Recalling the previous chapter, this 20-hour capacity is the capacity of the battery related to a constant discharge of 1 amp for 20 hours. Effectively, the use of Eqn. (23) normalizes the battery capacity based on Peukert's coefficient. This produces a value closer to the maximum capacity as discussed in Chapter 3. If the advanced model is used, C_{total} is the maximum theoretical capacity (C_R^0) as defined in the previous chapter.

Finally, a set of discharge criteria specify the end of the simulation routine. Typically, a vehicle drive cycle is physically complete when the vehicle either (a) reaches its final destination or (b) completely depletes its energy source (traditionally, a petroleum based fuel such as gasoline or diesel). Therefore, the simulation allows for selection of either of these termination criteria. In specific, the simulation can run a given amount of drive cycles or repeat the drive cycle until reaching a given SOC lower limit. The cycle number termination criteria allows the simulation to proceed as long as the simulation has not reached the number of allowable cycles input by the user or 10% SOC. The lower limit SOC criteria only stops the simulation once the vehicle state of charge reaches the specified limit set by the user. These two options allow the user to perform any physically feasible simulation length desired. After reaching the termination criteria, the simulation exits the transient loop while saving the primary route statistical data.

Another primary concern with electric vehicles is the amount of time required to charge the battery pack [3, 24-28]. Once the vehicle route is completed, it is often useful to calculate the charging time required to bring the battery pack back to the initial SOC. Therefore, implementation of a simplistic charging algorithm allows estimation of the charging time based on the charge removed during a simulated route. Hence, computation of charger power ($P_{charger}$) uses a specified charger amperage and voltage ($I_{charger}$ and $V_{charger}$, respectively from the charger model employed) along with an efficiency factor ($\eta_{charger}$):

$P_{charger} = \frac{I_{charger} V_{charger}}{1000} \eta_{charger}$	(24)

Then, calculation of the bulk charge time (t_{charge}^{bulk}) is found by dividing the energy removed in kWh during the route ($E_{pack}^{removed}$) by the charger power, resulting in the amount time required to charge the battery pack in hours:

$$t_{charge}^{bulk} = E_{pack}^{removed} / P_{charger} \quad (25)$$

In lead-acid cells, the charging algorithm is typically broken down into three stages: constant current charge (CCC), constant voltage top charging (CVC), and then a float charge in order to account for the intrinsic losses that occur in lead-acid batteries over time. In lithium-based batteries, the float charge is not necessary and a simple constant-current, constant-voltage (CCCV) charging algorithm is often used. Since the current associated with the CVC portion of the charging curves is typically relatively small when compared to the CCC, the top charge and float charged are often referred to as the float charge. While actual float time of battery under constant voltage conditions varies based on cell chemistry and charger design, it typically ranges from two to three times the amount of time required for bulk charging [28]. As a result, the simulation employs a multiplication factor of 2.5 in order to calculate the total charge time of the battery pack:

$$t_{charge}^{total} = 2.5(t_{charge}^{bulk}) \quad (26)$$

While this is a high-level, first-order approach to battery charge times, it provides a reasonable estimation, as well as the ability to simulate the charge time associated with different levels of battery charging.

The primary purpose of the simulation tool is to calculate duty cycle parameters (e.g., range and energy usage requirements) during a specified route. However, one can employ similar methodologies in order to compute vehicle performance criteria such

as various acceleration times and road grade climbing performance. As a result, after completion of the route simulation, a separate acceleration force model determines vehicle acceleration profiles using the supplied inputs. The overall routine is similar to the previously described algorithm with a few simplifications. Vehicle SOC is set to 90% and remains constant throughout the acceleration calculations. This prevents usage of peak pack voltages resulting in idealized acceleration values. In addition, the current draw of the system or the motor torque profile limits acceleration, whichever is lower. Calculating this value requires computation of a new torque curve using the power available from the specified current limit and the pack voltage associated with a 90% SOC. Then, the model compares the torque curve of the selected motor to the curve defined by the manufacturer. Generation of a new torque curve then occurs at each motor speed value based on the lower (most limiting) of the two torque values associated with that rotational motor speed. Then, simulation of vehicle acceleration happens using the newly defined torque values and a finite difference form of the tractive force balance as follows:

$F_{GR} = mg\sin\theta$	(27)
$F_D = \frac{1}{2}\rho A_f C_D V^2$	(28)
$F_{RR} = \mu_{RR} mg\cos\theta$	(29)
$F_{LA} = \left(G_{final}/r_{tire}\right)\tau_{motor}\eta_{motor}\eta_{transmission}$	(30)
$V(t+1) = V(t) + \left[\left(F_{GR} + F_D + F_{RR} + F_{LA}\right)/m\right]dt$	(31)

The resulting acceleration calculates the vehicle velocity at the next time step. Repetition of this process continues until the motor speed reaches the upper operational limit or the acceleration function reaches the maximum allowable runtime (set at two simulated minutes of acceleration by default).

Performing this numerical process at constant grade changes of 0, 4, and 6% allow for simulation of vehicle acceleration performance due to gradation. Moreover, use of a similar algorithm allows for calculation of the peak grade that the vehicle can handle. This is important in order to help design a vehicle for different geographical locations (e.g., Kansas City vs. San Francisco) along with determining how factors, such as vehicle weight and peak motor torque, affect the on-road performance of the vehicle. Since the peak grade is typically the slope over which a vehicle can maintain a velocity, the magnitude of the motor rotational speed is no longer critical as long as the direction remains positive (e.g., forward movement and not stalled or rolling backwards). Therefore, the motor torque can be set to the peak value determined from the newly calculated torque profile. Application of this torque to the same previously mentioned finite difference form of the tractive force balance determines if forward movement is possible. Starting with a 0% grade, iteration of the grade by values of 0.1 degree commences until acceleration is no longer possible. This limit then defines the maximum grade of the vehicle.

3. Model Implementation

For this effort, MATLAB provides the numerical framework for the simulation. This is because of its real-time programming language and inherent post-processing facilitating rapid development and quick analysis of results [29].

3.1 Calculating Vehicle Payload

It is well documented that vehicle payload can have a significant effect on the energy economy of a vehicle, both conventional and electric [3, 30, 31]. This is particularly applicable for delivery vehicles, such as the 1997 GMC Jimmy targeted for

delivery routes by the University of Kansas Libraries. In order to simulate payload effects, a variety of default options are available within the model:

- 0% loaded
- 50% or 100% loaded (Constant or Linearly Decreasing vs. Time)
- 100, 200, 300 kg (Constant or Linearly Decreasing vs. Time)

As explained previously, these options include the ability to simulate payloads at constant values, as well as decrease the payload over time representing a delivery vehicle offloading packages along the route. If using a constant mass value, adding the mass of the payload ($m_{payload}$) to the vehicle base mass (m_{base}) at each time step determines the simulated total mass.

$$m = m_{base} + m_{pack} + m_{passengers} + m_{payload} \quad (32)$$

where $m_{passengers}$ are the total mass of the on-board personnel and m_{pack} is the mass of the battery pack. Separation of the battery pack mass allows for independent calculation of the total vehicle weight at any point in the model based on the specific energy density and final configuration of the battery pack, a process that will be covered later.

Implementing a decreasing value involves dividing the selected value by the total route time (t_{total}) from the route input file while subtracting this value from the total payload mass at each time step:

$$m(t) = m(t-1) - \left(m_{payload} / t_{total}\right) dt \quad (33)$$

In addition, this list includes the option to select pre-defined values or values calculated based on the gross vehicle weight rating (GVWR). By selecting a value based on the GVWR, calculation of actual payload transpires by subtracting the base weight of the vehicle from the GVWR:

$m_{payload} = \text{GVWR} - m_{base} - m_{pack} - m_{passengers}$	(34)

Then, adding this payload value to the base weight of the vehicle allows for performance of the simulation at (or a fraction of) the GVWR mass. Choice of GVWR provides for performance analysis of the vehicle under the limit of occupant safety.

3.2 Measuring Vehicle Frontal area

There are two methods available in order calculate the vehicle frontal area required for the aerodynamic drag calculation. The most basic, first-order approach is to measure the absolute height (H) and width (W) of the vehicle body and approximate the area as 85% of the resulting rectangle [32]:

$A_f = 0.85(H \cdot W)$	(35)

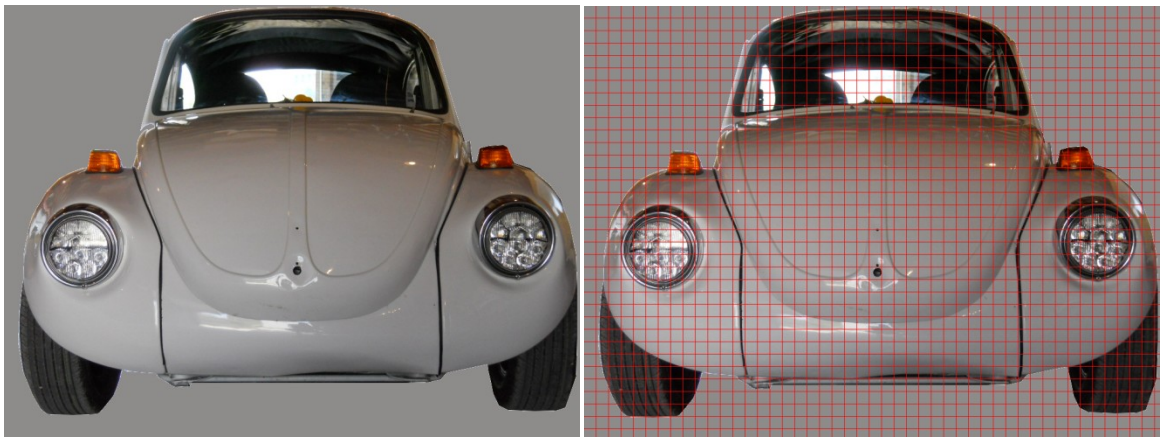

Figure 1: Frontal area calculation method using GIMP grid overlay and headlight (7") for reference point.

The second (and more accurate) approach is to photograph the front of the vehicle as perpendicular as possible ensuring that a known length reference exists in the picture (Figure 1).

Then, one lays a grid over the picture using Gimp (a GNU Image Manipulation Program) or similar image editing software [33]. The next step is to discretize the image while

ensuring that the sum of a set number of grid lines matches the reference length. This is in order account for the physical size of each square in the grid. Moreover, the total number of squares should remain sufficiently large in order to minimize the importance of a fraction of a square. Subsequent summation of the squares calculates the total frontal area of the vehicle. This method reduces some of the error associated with measuring the often-complex shapes such as the front of a vehicle. For the first method and the VW Super-Beetle in Figure 1, the vehicle body height is equal to 30 squares (42 inches) and body width is 44 squares (61 inches) ending in a total frontal area is 2177 in^2. Using the second method and 1052 squares, the frontal area is 2062 in^2.

3.3 Motor Map and Profile Modeling

Calculation of the incoming power requirement for the motor requires determination of the motor efficiency. The simulation accomplishes this by implementing a map of the motor efficiency often found by motor manufacturers through extensive dynamometer testing. Such testing typically transpires by testing the motors under a constant load and measuring the efficiency as motor speed varies. Figure 2 presents a typical motor efficiency plot.

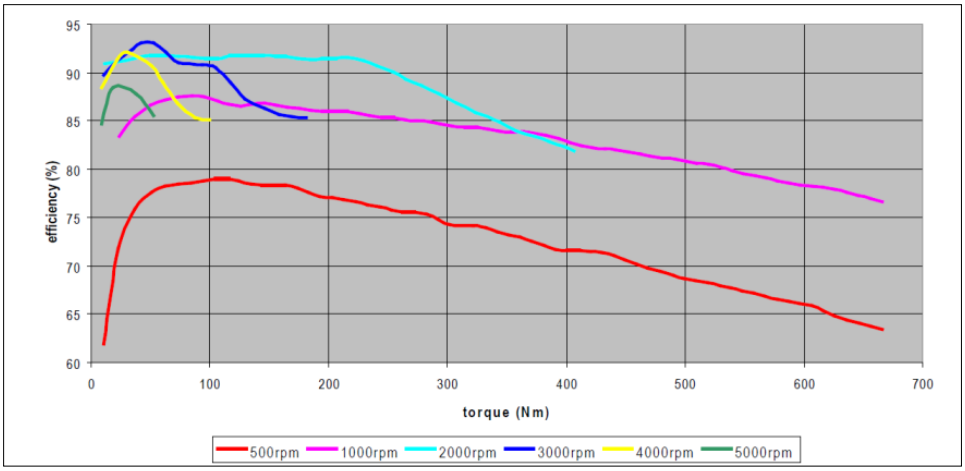

Figure 2: Azure Dynamics AC90 electric motor efficiency profiles [34].

In many cases, manufacturer supplied data is used in the absence of the necessary equipment required to develop the curves through testing. Extraction of the data from a supplied specification sheet requires use of a data digitization program, such as TechDig [35]. TechDig is software that allows the user to save a bitmap of a graph, align the axis using specified coordinates, and then extract the data in comma separated values format. This process essentially provides the user with the ability to generate a data set similar to the data used to generate the original figure. While the data typically contains a number of curves, the simulation requires an entire map to generate efficiency calculations at all possible operating points. In order to accomplish this, one first interpolates the efficiency curves between the data points extracted using TechDig to generate efficiency data along the entire applicable torque curve for each respective motor speed set. In this case, one Newton-meter (N.m) resolution resulted from using a cubic spline interpolation routine developed in MATLAB. Interpolation of the resulting curves then ensues at a one radian per second (rad/s) resolution in order to produce an efficiency map of over a specified range at a resolution of one N.m and one rad/s

(Figure 3). Finally, saving the map as a single comma-separated values (CSV) file allows the simulation routine to calculate the motor efficiency based on the required torque and the motor speed necessary to produce the required vehicle velocity.

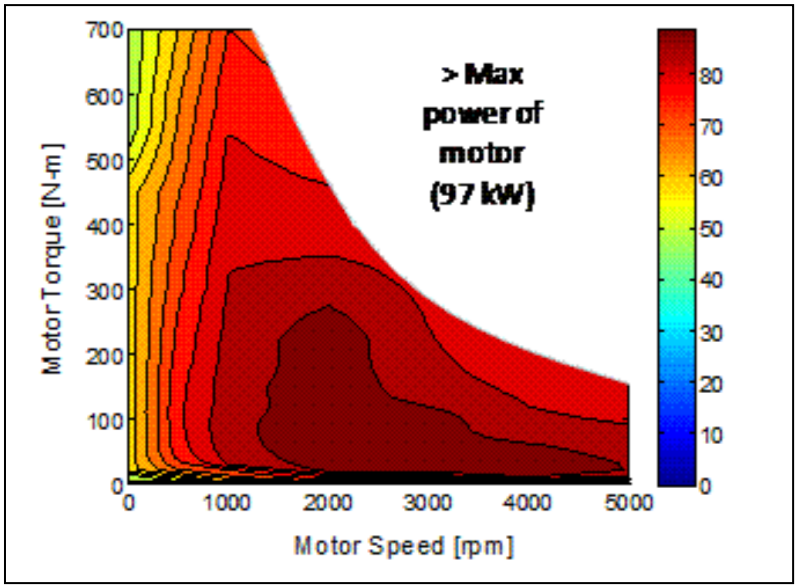

Figure 3: Estimated motor efficiency plot for Azure Dynamics AC90 electric motor.

While the motor efficiency map creates values across a broad range of motor usage, due to operational limits, some of these values are not physically obtainable (e.g., peak torque at peak motor speed). In order to create a tangible motor map, the same process just described allows for extraction of the torque profile from the manufacturer's specified data sheet (Figure 4). Interpolation of these values using a cubic-spline interpolation routine gives a specified torque limit at each of the motor speed points (also seen in Figure 3 by the blank area). Embedding the resulting profile into a MATLAB function file, called after each force balance routine, determines if torque limiting is necessary at the given motor speed. Torque limiting requires changing the

torque value to match the limit and the force balance is re-calculated using the newly updated torque value.

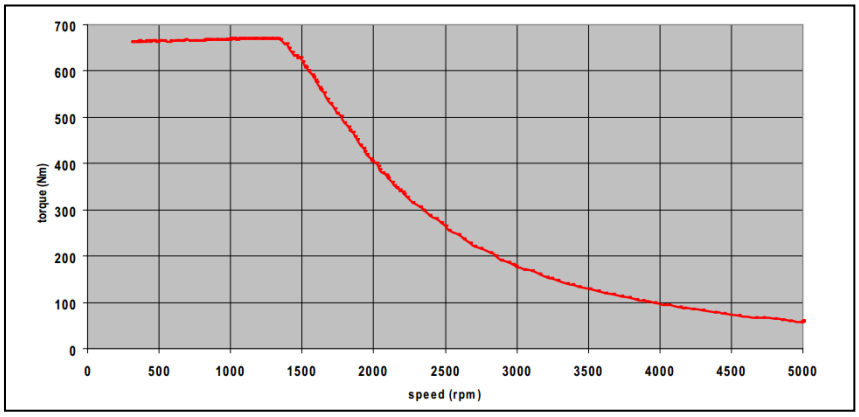

Figure 4: Azure Dynamics AC90 electric motor torque profile [34].

Another limit of the motor is the speed at which it can rotate. Calculation of the operational speed limit of the motor is simpler in practice than the torque limit. The algorithm described in the transmission section (3.5) allows for computation of the motor speed required to match the velocity in the input file (Eqn. 13). If this speed is beyond the operational limit of the motor specified by the manufacturer (e.g., far right value on *x*-axis of Figure 4), and shifting to another gear is not possible, the vehicle becomes speed limited. Consequentially, the motor speed is set to the operational limit and recalculation of the vehicle velocity occurs using this limit.

3.4 Battery Pack Modeling

Implementation of the battery model requires predetermination or calculation of multiple parameters in the numerical routines. For this effort, the battery pack section of the model contains a variety of parameters available for configuration, as well as calculation of automatic values through available battery information:

- Discover Energy EV31A-A Lead-Acid Pack (10S1P)

- Kokam SLPB255255 LiPo Pack (38S2)
- CALB 100Ah LiFe Pack (104S1P)
- Generalized Lead-Acid Pack
- Generalized LiPo Pack
- Generalized LiFe Pack

The Discover Energy pack is the original lead-acid battery pack for the 1974 Volkswagen series hybrid. The second selection is a Kokam lithium-polymer pack designed as a replacement for the lead-acid battery pack. The third option is the CALB lithium-iron pack designed and built for the 1997 GMC Jimmy EV. Options four through six are available for simulations of theoretical battery packs using the cell specifications from the first three options. This feature allows the user to design and simulate custom battery packs designed around the three specific cell options. As most of the cells in options one through three are standard cells for their respective chemistry types, these simulations should provide good first-order estimates for other cell models of similar chemistries.

Accounting for the battery cell resistance in Eqns. (17) and (18) requires measuring the resistance of each of the cells under investigation using the Vencon UBA-5 battery analyzer. The battery analyzer includes the option to measure resistances in the hundredth milliohm range, thus making it useful for measuring cell resistance. This requires first calibrating the resistance of the test leads (typically 0.1 to 0.5 milliohms) and then measuring the internal cell resistance. Then, subtracting the resistance of the leads from the measured cell resistance determines the resistance of

the battery. Ten tests are performed for each of the batteries resulting in values of roughly 0.12 ohms for the lead-acid cells and 0.06 ohms for each of the lithium cells.

In order to allow for partial charging studies, the initial pack SOC can be set at the beginning of the simulation. This number should be set somewhere between 100% and the lower SOC limit as defined in the route information section. Theoretically, this value can be set as high as 110% if the user wants to simulate over-charging conditions. The default value is set at 99% because completely full charging is rarely achieved in real world situations [28].

Modeling of thermal effects on cell performance occurs by selecting an average battery temperature. Since the actual thermal rise of a cell under loading is a result of numerous factors, thermal effects only influence the model through average battery temperatures often taken as ambient conditions. This provides for a first-order approximation, and future work can involve calibration of thermal effects based on cell chemistry, physical cell design, heat capacity, and other heat transfer phenomena beyond the scope of this work. To estimate the effects of cell temperature, two methods are available. When using the advanced model selection of Eqn. (21) in Chapter 3 describes its implementation within the simulation. If using the simplistic version, a third-order polynomial is curve fit to the temperature-capacity relationship provided by the cell manufacturer. This allows for calculation of a fractional capacity (dependent variable) based on the average cell temperature (independent variable) selected.

Common definition of battery packs occurs through the number of strings wired in series and parallel. Both fields are available for describing the pack configuration and changing these fields updates the capacity of the pack (voltage and amp-hours).

Formatting of this field is done using the industry standard format of x**S**y**P** where 'x' indicates the number of cells in series (**S**) and 'y' indicates the number of series strings in parallel (**P**). Cell capacity (C_{cell}) is available in amp-hour format, and one enters the capacity of a single cell in the pack and not the total capacity of all the parallel strings. Then, computation of the entire pack capacity (C_{pack}) comes from the cell capacity multiplied by the number of parallel strings ($n_{parallel}$):

$C_{pack} = n_{parallel} C_{cell}$	(36)

Furthermore, the model calculates the total nominal battery pack voltage (V_{batt} used in Eqn. (18)) using the nominal cell voltage (V_{cell}) and the number of cells wired in series (n_{series}):

$V_{batt} = n_{series} V_{cell}$	(37)

A change to any of the pack configuration parameters updates the pack energy field (E_{pack}) in order to reflect the total energy of the pack in kilowatt-hours. This is done by multiplying the pack voltage by the pack capacity and then converting from watt-hours to kilowatt-hours:

$E_{pack} = V_{batt} C_{pack} / 1000$	(38)

Estimation of the mass of the vehicle battery pack is found by using a specific battery mass parameter $\left(\dot{\ }\right.$:

$\dot{\ } \quad / m_{cell}$	(39)

This allows the simulation to update mass calculations anytime the user changes the pack configuration. The model adds a factor of ten percent to the mass of the cells in order account for battery box packaging:

$m_{pack} = 1.1\left(E_{pack} / \dot{\ }\right.$	(40)

Battery voltage decreases under load [3, 28]; hence, the simulation accounts for this effect by creating battery discharge tables. Given that the model calculated in chapter three does not account for voltage drop conditions, calculations require the use of manufacturer's data. Furthermore, follow-up work providing for expansion of chapter three would allow for demonstration of this phenomenon within the model. Similar to the methods used to generate motor efficiency maps, TechDig allows for extraction of manufacturer specified discharge data (Figure 5). Interpolation of the resulting data using a cubic-spline interpolation algorithm in MATLAB generates voltage data at each depth of discharge (1-SOC) point in 0.01% increments. This produces the appropriate data arrays at each of the *C*-ratings provided by the manufacturer. Further interpolation of these curves across the applicable *C*-ratings of the battery at 0.01*C* increments using the same algorithm allows for generation of an entire voltage map based on depth of discharge and *C*-rating (Figure 6). These maps are then loaded into a function file in CSV format and the voltage of the pack is determined at each time step based on the current draw (and thus *C*-rating) of the battery and the recent depth of discharge calculation. Repetition of this process occurs for each battery under investigation.

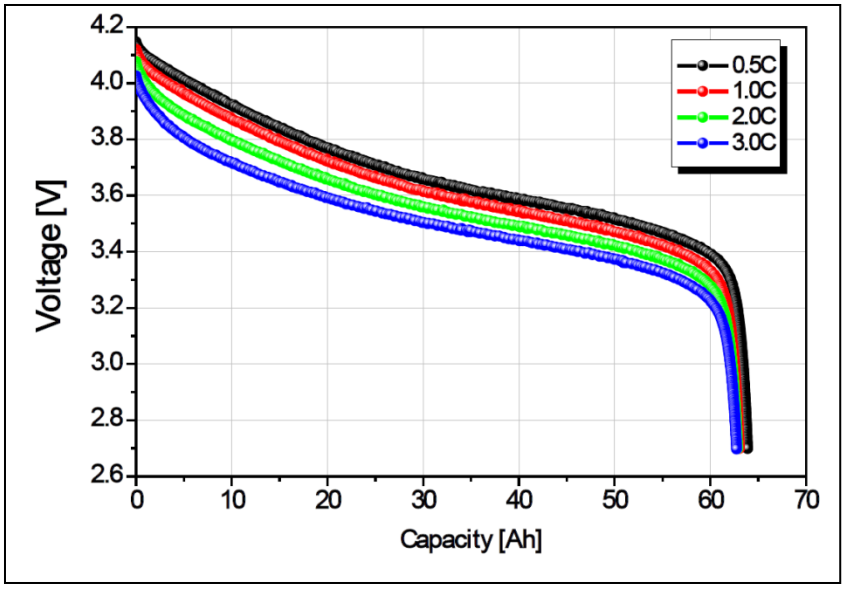

Figure 5: Kokam SLPB96255255 voltage-capacity relationship from manufacturer specification sheet [36].

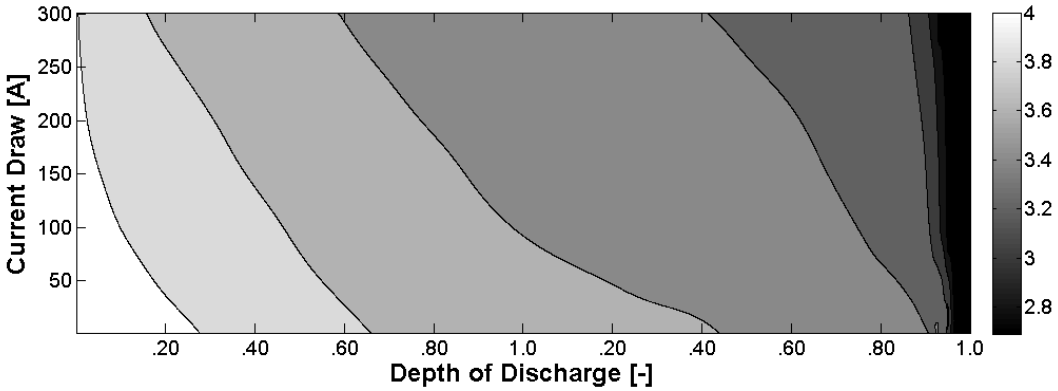

Figure 6: Estimated Kokam SLPB96255255 cell voltage map.

3.5 Vehicle Transmission Modeling

The model employs a routine that accounts for transmission shifting based on the current gear selection, an array of shift points, and motor speed. At each time step, the simulation compares motor speed to the shift point in order to move into the next gear (either an increase or decrease). If the motor speed is higher than the shift point to increase the gear selection, the current gear selection is increased. If the motor speed

has decreased since the last time step, a routine determines if a downshift is necessary. To accomplish this, calculation of a false motor speed is done based on a gear selection of one gear lower than the current gear selection. If this false motor speed is 500 revolutions per minute (RPM) less than the shift point at the lower gear selection, the transmission shifts down to the lower selection and the false motor speed becomes the new actual motor speed. Implementation of this 500 RPM difference prevents the transmission algorithm from constantly switching gears when in close proximity to the shift points. While this value is slightly arbitrary, adjustment by the user to more closely match the control algorithm inside the transmission is possible. While the motor speed and final drive ratio can determine the speed of the vehicle at any point, the model uses the speed from the input file, the present final drive ratio, and the tire diameter to determine the motor speed according to Eqn. (13).

3.6 Limiting Peak Vehicle Velocity

In some situations, it may be desirable to limit the maximum velocity of the vehicle regardless of the input file or standard cycle chosen. This can be particularly useful when developing velocity trends based on changing driving styles and route adaptability. To incorporate this effect, the "*top speed limit"* variable is available. This option is always active, and simply searches the input file for speeds greater than the set limit and changes those values to the specified limit. To deactivate this feature, the user should simply set the limit to an unrealizable value.

3.7 Distance Recovery Option

The distance (D) traveled at each time step is a function of vehicle velocity and the change in time at each step:

$D(t) = D(t-1) + V(t)dt$	(41)

Therefore, if there is a difference between the velocity of the input file and the capable velocity of the vehicle due to current or torque limiting, there will also be a difference in the distance traveled between the two methods. While it may be desirable to quantify this difference, it may also be necessary to ensure that the two methods cover the same distance over the course of the route. Implementation of a selectable distance recovery algorithm allows for this consistency. When the overall distance deviation between the input file and the simulated route becomes greater than ten meters, the attempted velocity is set to an arbitrary and physically unachievable limit. This ensures that the current drawn from the battery pack is equivalent to the current draw limit. Implementation of this algorithm at every step ensures that current limiting will occur until the difference between the two methods is again within ten meters.

This process has two obvious drawbacks. One is the fact that the velocity may be beyond the physically achievable limit of the route. For example, the velocity may be rather large when the route requires the vehicle be stopped at a stop sign or slowed down while turning a corner. This algorithm is also fairly demanding on the battery pack, and it may constantly require the pack to operate at the upper current draw limits.

3.8 Vehicle Accessory Draw Options

A critical component in electric vehicle design is the power draw from vehicle accessories including heating, ventilation, and air conditioning (HVAC) components. In traditional vehicles, the ICE often powers these systems. However, when energized solely on electricity, these components can cause a significant power draw on the battery pack requiring inclusion within the simulation. Typical vehicle auxiliary systems often include:

- Headlights
- Parking lights
- Windshield wipers
- Engine/motor coolant pump
- Engine/motor control systems
- Power steering pump
- Brake compressor air pump
- Heating systems
- Air conditioning systems

These components often cycle on and off at various times based on user input, driving cycle demands, and environmental conditions. Considering all of the factors to model these systems can prove time consuming and predicting the user input is difficult at best. In order to overcome this variability, the model utilizes an average power draw from these systems over the entire drive cycle. This allows the user to include the accessory and HVAC component effects by multiplying the average power draw (when in use) by the total predicted usage time in order to determine the total energy draw of that accessory during the route.

$$E_{acc}^{i} = \overline{P}_{acc}^{i} t_{acc}^{i} \quad (42)$$

where E_{acc}^{i} is the energy draw from a single accessory component i. The summation of these power draws divided by the route time allows for estimation of the power draw across the entire route:

$$P_{acc} = \left(\sum_{i=1}^{N_{acc}} E_{acc}^{i} \right) / t_{total} \quad (43)$$

where N_{acc} is the total number of vehicle accessory draws under investigation. Then, the model adds this power draw to the total power draw of the vehicle battery pack at each time step according to Eqn. (15). While this method is merely an estimation, it avoids the complexities associated with implementing the duty cycle files required to model the state of these systems at every time step, as the structure of these files are often unknown or difficult to generate. This maintains simplicity within the input file requirement.

3.9 Idle Off Option

When recording data from a vehicle during a real world test, a data logger may not stop recording data even through the vehicle is not in operation; e.g., parked for getting a soda at a gas station. This can result in long strings of data for the input file although there is no change in elevation or velocity data. Therefore, when implementing this data in an input file, the resulting accessory draw will continue to deplete the battery pack during the simulation even though these data points are not actually a part of the vehicle route. In order to account for this, the simulation employs an optional routine to turn the accessories off during idle periods. When active, a tracker counts the number of continuous points in which the vehicle velocity is equal to zero. When this counter reaches a full minute, the accessory draw of the simulation is set to zero until the velocity again exceeds zero. Resetting the counter occurs the next time the vehicle velocity exceeds zero. While this routine may lead to errors in the total accessory draw calculation (e.g., the driver leaves the vehicle parked with the air conditioner in operation), the amount of energy and infrequency associated with these events do not warrant specific simulation at this juncture of model development.

4. Experimentation and Model Validation

In order to investigate model accuracy, the 1974 Volkswagen series hybrid (VW) (Table 1) provided the platform for various performance data collection. The VW utilizes both 120 VAC and 230 VAC on-board chargers to integrate with the vehicle generator and encompass a variety of charging options. Use of the vehicle coastdown testing procedure outlined in Chapter 2 resulted in the model parameters given in Table 2. Furthermore, a combined route consisting of both urban and highway driving around Lawrence, Kansas (Figure 7) offered a standard, relatively repeatable driving cycle for comparison within the model.

Table 1: 1974 Volkswagen Super-Beetle series hybrid specifications.

Transmission	Original Four Speed w/ Reverse
Drive motor	NetGain Warp 9, 120 VDC Brushed Series Wound
Motor controller	NetGain Controls Classic DC Speed Controller
Battery pack	Discover Energy EV31A-A 10S1P 120 VDC, 115 Ah
DC-DC converter	ElCon TDC-400-120, 400 W
Generator	Yanmar L100V 5.5 kW operating on 100% biodiesel
120 VAC Charger	ElCon PFC 2500, 1.5 kW
230 VAC Charger	Zivan NG3 F7-PH, 3 kW
Tire Size	185/75R16
Weight w/ generator	2747 lbs
Weight w/o generator	2534 lbs

Table 2: VW coastdown study parameters determined using Chapter 2 derived model.

Parameter	$\bar{x}$
a_d	0.4915
b_d	0.21112
a_{rr}	0.0759
b_{rr}	0.00228
d_{rr}	0.0000168
α	-0.227
β	0.8362

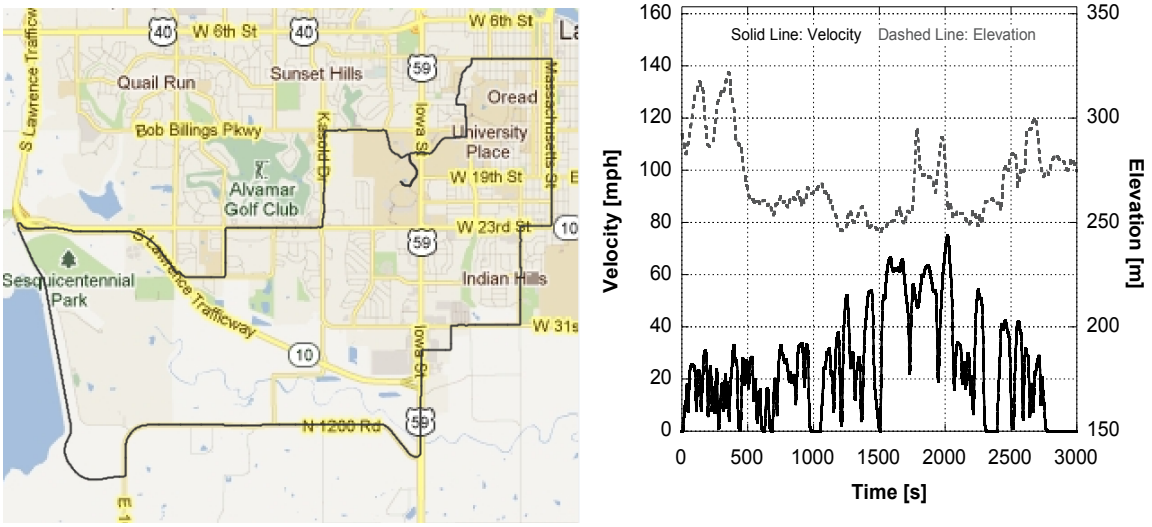

Figure 7: Map (left) along with velocity and elevation profile (right) for Lawrence, Kansas combined usage test route.

The route covers over 21.2 miles with an average velocity of 25.3 mph, top speed of 75 mph, and 722 meters of total elevation change. The route was traced a total of seven times with a focus on maintaining the posted speed limit as much as possible to aid in route consistency. Three runs utilized the biodiesel powered generator in the vehicle but not in operation (hybrid operating in EV mode), one test run with the generator running and charging the batteries (hybrid mode), and three test runs with the generator removed from the car in battery electric vehicle (BEV) mode. This combination allows the authors to model the effects of operating in hybrid mode, as well as the effects of the generator weight on vehicle performance. Recording of battery and motor performance data uses the interface module provided with the NetGain Classic Motor Controller. This interface module communicates with the vehicle controller via a CANbus in order to monitor vehicle performance information. Data is stored at a 5Hz rate on a micro standard digital memory card in CSV format.

A Race Technology DL1 GPS based data logger collects test data on a compact flash card while measuring speed, acceleration, and elevation data. It records at a 20Hz rate using a combination of GPS signals and an on-board six-axis accelerometer. An external battery pack powers the DL1, thus eliminating outside effects on the vehicle battery pack. The data logging process for the motor controller and GPS data loggers starts and ends simultaneously in order to ease in the alignment of time stamps during post-processing. Race Technology provides analysis software named *RT Analysis* in which one can convert data from the route into numerous formats for subsequent examination. For the work described here, this conversion into .mat matrices at a 5Hz rate (to coincide with the powertrain performance data) allows for easy use in MATLAB. Finally, before each test route, vehicle weight is measured using a set of Longacre AccuSet 72701 four-wheel scales. The use of the four-wheel scales allows for completely isolating the vehicle while taking measurements of all wheel loads independently. The scales chosen offer a 0.5 pound per pad accuracy for a total of two pounds per 6000-pound (capacity) accuracy.

Operating the vehicle in hybrid mode requires forethought in order to ensure that the vehicle charger becomes active. When first connecting the charger to the supply power, it initializes a routine to determine if battery charging is necessary. If the charger determines the battery pack is at an acceptable SOC, the charger will power down and not check the pack again for an extended period. Consequentially, starting the generator as soon as the test run begins will not charge the battery pack at any point during the 50-minute test. Therefore, starting the generator roughly four miles into the test run ensures that the battery pack has reached less than a 90% SOC.

Table 3: Route statistics from three driving modes

	Test Time	Energy Used	Efficiency		Final Voltage	Average Current
	[s]	[kWh]	[kWh/mi]	[mpg_e]	[V]	[A]
Hybrid in EV Mode (1)	3145	7.23	0.335	100.6	117	75.6
Hybrid in EV Mode (2)	3256	7.33	0.341	99.0	118	73.0
Hybrid in EV Mode (3)	3020	7.52	0.351	95.9	119	80.1
Series Hybrid Mode	2866	7.20	0.335	100.6	122	79.1
BEV Mode (1)	2788	6.84	0.318	106.0	120	74.2
BEV Mode (2)	2963	6.85	0.319	105.5	121	73.8
BEV Mode (3)	3002	6.82	0.318	106.1	120	72.5

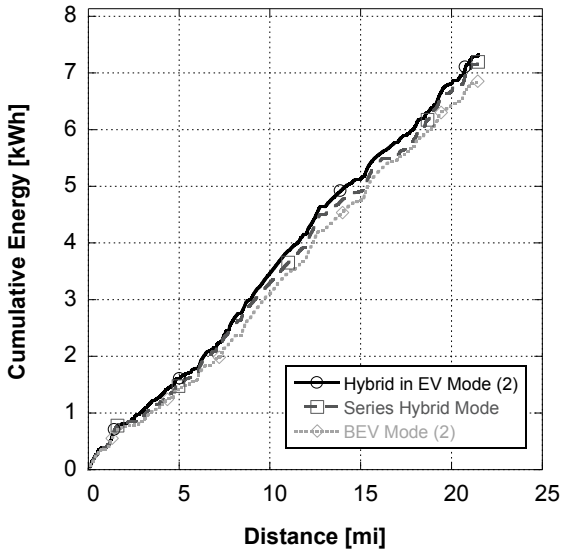

Figure 8: 1974 Volkswagen energy profiles based on operational mode.

Table 3 provides the test run statistics of the three previously mentioned operating modes. Figure 8 demonstrates the weight and energy usage effects between the three operating modes with the energy profiles for the median test run of each mode indicated. Both sets of data for the hybrid configuration result in roughly 7.25 kWh of energy usage with the primary difference being the vehicle gains about 1.75 kWh of this energy back if the generator is in operation during the test run. Because of the weight savings due to removing the generator (~100 kg), the BEV configuration demonstrates

less total energy usage (6.85 kWh). Figure 9 presents the voltage and current profiles using the median energy usage trial for each mode. Because of the dynamic variability associated with monitoring the electric power system, this figure presents these profiles using one-minute rolling averages.

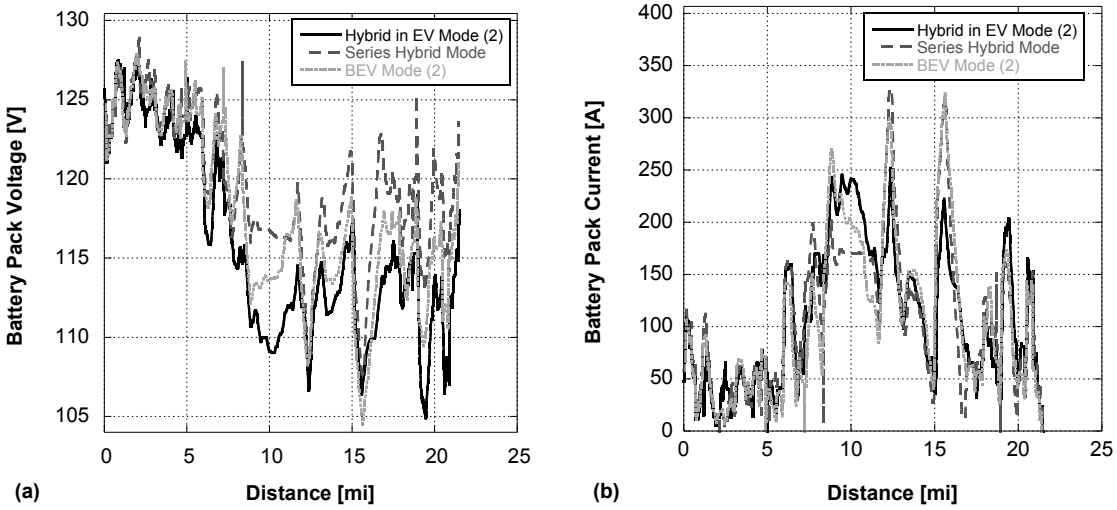

Figure 9: Battery a) voltage and b) current for the three operational modes.

The series hybrid mode has a higher battery pack voltage since the generator is constantly charging the battery pack during the route. In addition, this results in lower current draws because higher pack voltages require less current needed in order to deliver the same amount of power. In BEV mode, the voltage and current is typically between the values of either hybrid mode. This relates directly to the weight savings by removing the generator; e.g., better than the hybrid with generator off, but not as good when the generator is on.

After the vehicle returns from the test run, the batteries are given time to recover (chemistry and temperature) before being placed on charge. The Energy Detective 5000 (TED) hardware provides monitoring of this charging process. The TED hardware is a power line communication system integrated into the electrical system of the

building in which the vehicle is stored. The system uses voltage sensing modules and hall-effect current clamps placed in the building's electrical panel. This system continuously measures the supply voltage and current through the charging circuits while storing to a memory module on a per-minute basis. This allows for measurement of vehicle charging curves in order to investigate the energy usage profiles of the vehicle. The curves are stored in a CSV format and are retrievable through connection via personal computer. Figure 11 plots the battery pack charging data using the test cases with and without generator operation.

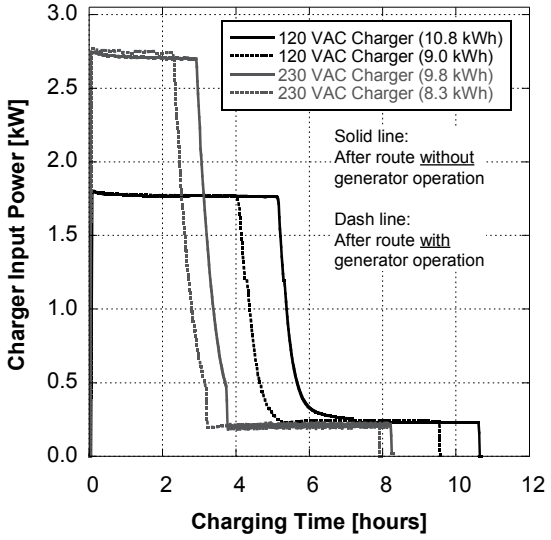

Figure 10: Charging curves for 1974 Volkswagen

When comparing a test run with the generator in operation to a test run without this added power, it appears the generator is able to return about 1.5-1.8 kWh during the test. This matches expectations as the charger was inputting roughly 2.75 kW (Figure 10) over roughly 40 minutes (2.75 kW × 40 minutes = 1.8 kWh). Less power is required in order to return the battery pack to full charge conditions regardless of the drive cycle that is considered (generator on/off), when using the 230 VAC charger. This is likely an

indication of charger efficiency when converting VAC power (supply) to VDC power (battery pack).

Table 4: 1974 Volkswagen Beetle series hybrid model parameters.

Vehicle Geometry	
Wheelbase [m]	2.42
GVWR [kg]	1290
Unloaded Mass [kg]	907
Frontal Height [m]	1.07
Frontal Width [m]	1.55
Coefficient of Drag [-]	0.48
Coefficient of Rolling Resistance [-]	0.01
Advanced Coastdown Model Parameters	
a_d [-]	0.4915
b_d [m/s]	0.21112
a_{rr} [N]	0.0759
b_{rr} [N/(m/s)]	0.00228
d_{rr} [N/(m^2/s^2)]	0.0000168
α [-]	-0.227
β [-]	0.8362
Transmission and Tire Parameters	
Transmission Gear Ratio [-]	2.06 (2nd gear)
Rear Differential Gear Ratio [-]	4.125
Tire Size Specification	195/65R15
Motor	
Model	NetGain Warp 9
Current Draw Limit [A]	400
Regenerative Braking Ratio [-]	-
Battery	
Model	Discover Energy EV31A-A
Series Strings	10
Parallel Strings	1
Nominal Cell Voltage [V]	12
Cell Capacity [Ah]	115
Cell Impedance [ohms]	0.1
Pack Configuration	10S1P
Pack Energy [kWh]	14
Battery Weight [kg]	354
Auxiliary Draw [watts]	135

At this point, enough information exists in order to compare and contrast a VW simulation with the real world test data. Table 4 provides the full specifications required in modeling the VW. In order to simulate the generator effect on battery pack energy,

the model adds the bulk charge power (2.75 kW) from the 230 VAC charger to the overall energy balance as a positive power draw beginning at the time in which the generator is started.

Table 5: Traditional model simulation results.

	Energy Used [kWh]		Efficiency [kWh/mi]		Final Voltage [V]		Average Current [A]	
	Test Data	Model	Test Data	Model	Test Data	Model	Test Data	Model
Hybrid in EV Mode (1)	7.23	7.36	0.335	0.347	117	118.0	75.6	80.5
Hybrid in EV Mode (2)	7.33	7.55	0.341	0.356	118	117.9	73.0	78.3
Hybrid in EV Mode (3)	7.52	8.12	0.351	0.383	119	117.4	80.1	87.4
Series Hybrid Mode	7.20	7.65	0.335	0.361	122	120.6	79.1	88.4
BEV Mode (1)	6.84	7.21	0.318	0.340	120	118.6	74.2	86.0
BEV Mode (2)	6.85	7.23	0.319	0.341	121	118.7	73.8	79.7
BEV Mode (3)	6.82	7.17	0.318	0.338	120	118.8	72.5	78.2

Table 6: Advanced model simulation results

	Energy Used [kWh]		Efficiency [kWh/mi]		Final Voltage [V]		Average Current [A]	
	Test Data	Model	Test Data	Model	Test Data	Model	Test Data	Model
Hybrid in EV Mode (1)	7.23	6.93	0.335	0.327	117	118.7	75.6	75.7
Hybrid in EV Mode (2)	7.33	7.19	0.341	0.339	118	118.5	73.0	74.2
Hybrid in EV Mode (3)	7.52	7.80	0.351	0.368	119	117.9	80.1	83.9
Series Hybrid Mode	7.20	7.31	0.335	0.345	122	121.4	79.1	84.2
BEV Mode (1)	6.84	6.91	0.318	0.326	120	119.0	74.2	82.1
BEV Mode (2)	6.85	6.93	0.319	0.327	121	119.2	73.8	76.25
BEV Mode (3)	6.82	6.74	0.318	0.317	120	119.2	72.5	74.8

Table 7: Relative error comparison of modeling methods

	Total Energy [kWh]	Relative Error	
	Test Data	Traditional Model	Advanced Model
Hybrid in EV Mode (1)	7.23	1.80%	4.15%
Hybrid in EV Mode (2)	7.33	3.00%	1.91%
Hybrid in EV Mode (3)	7.52	7.98%	3.72%
Series Hybrid Mode	7.20	6.25%	1.53%
BEV Mode (1)	6.84	5.41%	1.02%
BEV Mode (2)	6.85	5.55%	1.17%
BEV Mode (3)	6.82	5.13%	1.17%

This comparison between the experimental data and the model begins by first using the traditional models for rolling resistance and aerodynamic drag. Table 5 presents this assessment of the various energy usage statistics. Then, the same test runs are simulated occurs using the advanced rolling resistance and drag models described in Chapters 2 and 3 with the outcomes elucidated in Table 6. As expected,

the use of the updated models demonstrates a more accurate simulation across all three operating modes of the vehicle. This is evident in Table 7 that provides the relative error of both modeling methods. Overall, the associated error is likely due to the numerous assumptions made in the model, as well as the accuracy associated with creating input files from data logged vehicle tests.

A validated model allows for exploration of different vehicle parameters and associated configurations. For example, performing a parametric study across a variety of vehicle loading conditions, tire pressure values, and battery temperature effects allows for an expanded understanding of the operational range of the vehicle (Figure 12). In particular, the vehicle performs significantly better when battery conditions are greater than 20 degrees Celsius. The average range across all loading conditions is almost 11% better when comparing the simulations performed above 20 degrees Celsius. This matches the expectations derived from Chapter 3 which shows that battery capacity falls off more quickly below the reference temperature (T_{ref}) of 23 degrees Celsius.

As tire pressure decreases, the achievable range of the vehicle also decreases as a function of the higher rolling resistance force; e.g., an average of 6.5% for a decrease from 50 psi to 15 psi. Chapter 2 discusses this trend in detail. Moreover, as anticipated the total vehicle mass tends to have a significant impact on the total range of the vehicle. As previously mentioned in this chapter and Chapter 2, mass has a negative influence on the rolling resistance, gradation force, and the overall acceleration force of the vehicle (Newton's Second Law). Figure 12 indicates that a 60% increase in mass will result in a nearly 40% decrease in range. This trend leads the authors to

believe the vehicle would benefit from a pack with a lower overall mass as the Discover Energy lead-acid pack accounts for roughly 30% of the total vehicle mass.

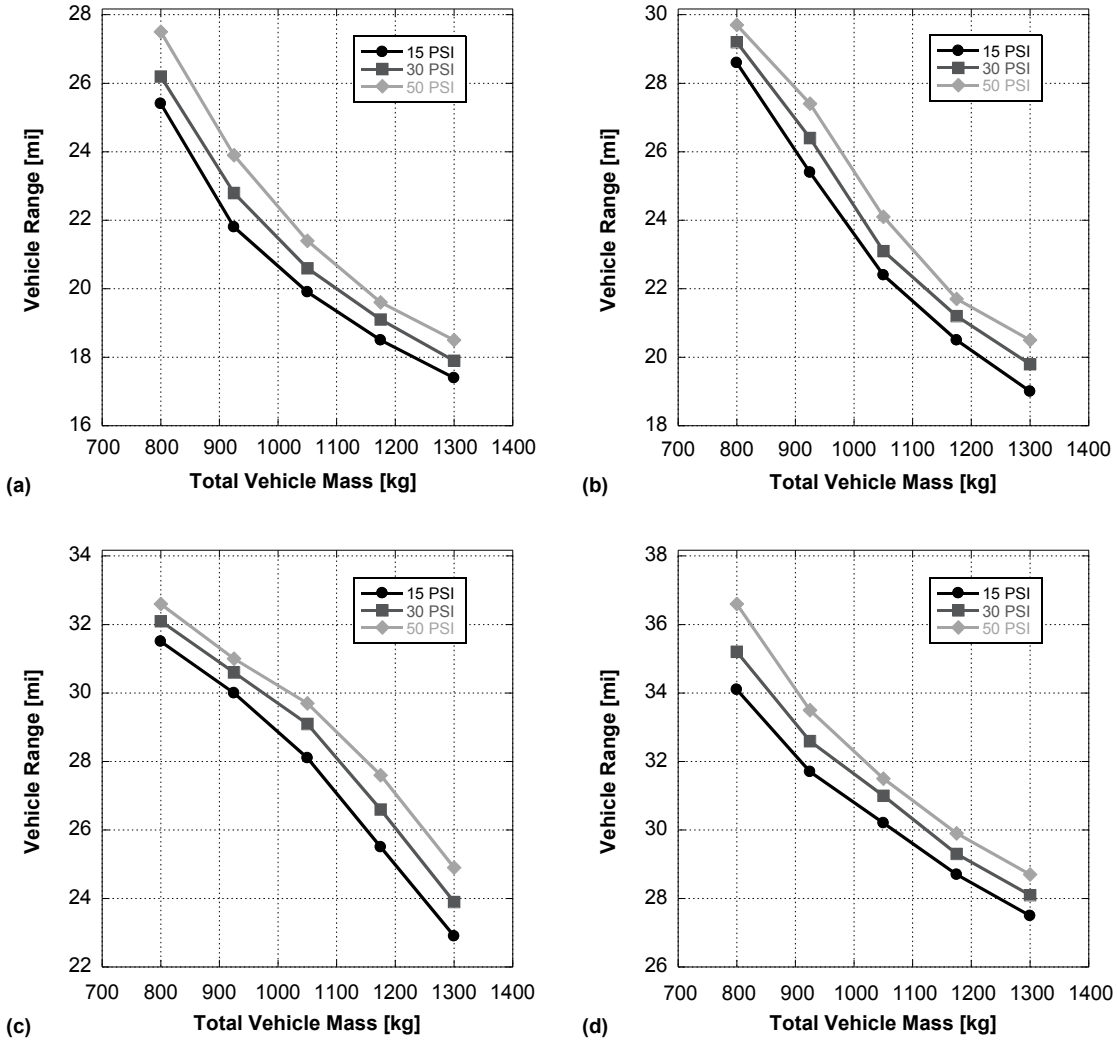

Figure 11: Discover Energy lead-acid simulations at a) -10°C, b) 0°C, c) 23°C, and d) 45°C.

While lead-acid technology and the initial vehicle design provided a medium for model development and validation, significant improvement in vehicle range and overall performance is possible by converting the 1974 Volkswagen series hybrid to utilize a more modern lithium battery pack. Thanks to a generous donation from Aptera Motors,

the author constructed and built a lithium battery pack designed around 76 Kokam SLPB96255 cells (Figure 12). In a 38S2P configuration, the pack possesses a 140 VDC nominal voltage and 120 Ah capacity for a total energy content of 16.8 kWh. The pack including the cells and necessary chassis weighs roughly 250 pounds (as opposed to the 800 pound 13.8 kWh lead-acid pack). By removing the generator, these numbers bring the total operating weight of the VW to less than the 2088 pound factory weight (2040 pounds).

While the pack would undoubtedly provide improved performance over the lead-acid configuration, an inherent design feature caused the pack to self-discharge and rupture destroying many of the cells (Figure 12). According to Victor Tikhonov of Metric Mind EV, the fused seams along the sides of the pouches are conductive [37]. Kokam omitted this feature in both the safety and design documentation provided. As a result, aluminum rails used in the support structure for the battery box frame allowed the cells to self-discharge upon being connected in series. While funding and time prevented the building of a suitable replacement pack, the model still allows the authors to simulate the effects of conversion to a new, modern battery pack design.

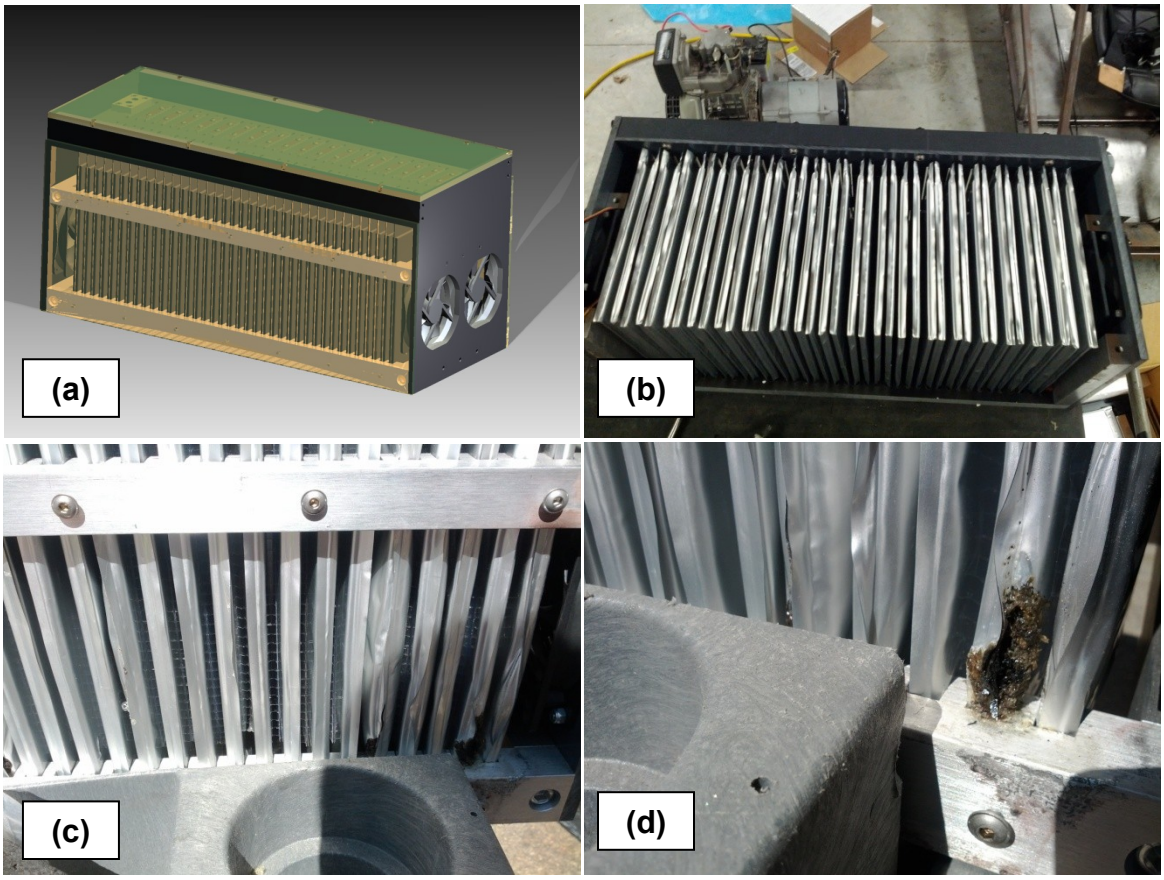

Figure 12: Kokam SLPB96255255 a) design rendering, b) built pack, and c-d) ruptured cells.

Table 8: Comparing lithium battery pack simulations

	Advanced Model Energy Used [kWh]			Advanced Model Remaining SOC [%]		
	Discover	Kokam	CALB	Discover	Kokam	CALB
Hybrid in EV Mode (1)	6.93	6.02	6.13	18.5%	64.3%	56.5%
Hybrid in EV Mode (2)	7.19	6.15	6.25	14.7%	63.5%	55.6%
Hybrid in EV Mode (3)	7.80	6.70	6.76	5.5%	60.3%	52.0%
Series Hybrid Mode	7.31	6.32	6.40	38.6%	73.1%	67.2%
BEV Mode (1)	6.91	5.98	6.04	18.8%	64.6%	57.1%
BEV Mode (2)	6.93	6.08	6.17	18.5%	64.0%	56.2%
BEV Mode (3)	6.74	6.17	6.25	21.3%	63.4%	55.6%

The first lithium based battery pack simulated using the 1974 Volkswagen platform was the Kokam 38S2P lithium-polymer pack described in the previous paragraph. These simulations resulted in significant performance improvement over the lead-acid pack simulations as illustrated in Table 8. Moreover, it is feasible to construct

a pack similar to the Kokam configuration using the CALB 100Ah lithium-iron cells tested in Chapter 3. Table 8 also provides the simulation results using a theoretical CALB pack designed with specifications similar to the Kokam configuration (44S1P). The results illustrate that the lithium cells offer a greatly improved range and efficiency performance over lead-acid in every operational mode as the energy usage decreases by an average of 14% and the remaining SOC increases by nearly 42%. These results are a combination of lighter weight and higher capacity battery packs along with lower Peukert coefficients resulting in decreased discharge losses. The differences between the two lithium designs is minimal with the Kokam pack offering slightly better results due to a larger pack capacity and lower specific weight.

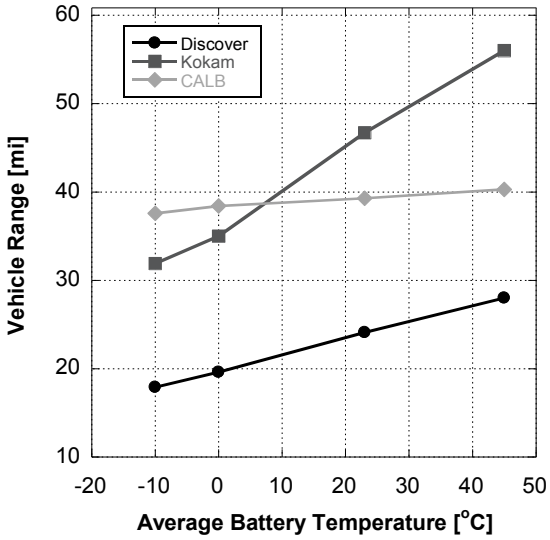

Figure 13: Cell chemistry effects on 1974 Volkswagen series hybrid range

As Figure 13 indicates, the CALB cells demonstrate a more uniform temperature performance than the other battery types. This is a direct result of the advanced model coefficients, and Chapter 3 explains this phenomenon thoroughly. While the Kokam cells offer a significant range improvement in warmer discharge conditions, temperatures below 8°C negate this advantage. The lead acid performance appears

relatively linear with temperature, matching the work of Buchmann [28] and the manufacturer supplied specification sheet [38]. Intended operation of the vehicle in warmer climates illustrates that the Kokam pack likely presents the best choice; however, the temperature characteristics of the CALB pack would provide for less range loss in colder operating conditions.

As previously mentioned, the ability to model the 1997 GMC Jimmy electric delivery vehicle (GMC) currently under construction for use by the KU Libraries is also of primary interest to the authors. While gathering the data set required to implement the advanced drag and rolling resistance model will not be possible until the vehicle is completed, the simulation can still be performed using the traditional dynamics model, as well as the advanced battery performance model. As a result, collection of data from the current KU libraries delivery vehicle using the DashDyno mentioned in Chapter 2 was done over a two-week period. The test run proved to be repeatable following a similar profile each day. Using the data set associated with the best GPS signal, Figure 14 provides the route characteristics used by the model.

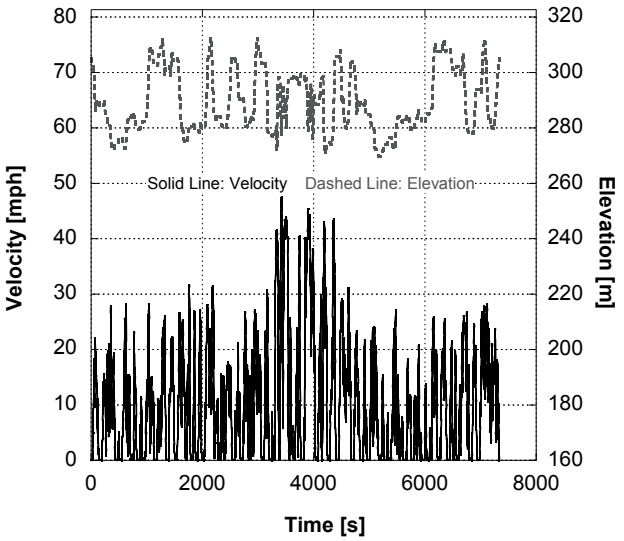

Figure 14: Velocity and elevation profile for KU Libraries delivery route.

Table 9: 1997 GMC Jimmy BEV model parameters

Vehicle Geometry	
Wheelbase [m]	2.72
GVWR [kg]	2200
Unloaded Mass [kg]	1590
Frontal Height [m]	1.65
Frontal Width [m]	1.75
Coefficient of Drag [-]	0.42
Coefficient of Rolling Resistance [-]	0.01
Transmission and Tire Parameters	
Transmission Gear Ratio [-]	-
Rear Differential Gear Ratio [-]	3.73
Tire Size Specification	195/65R15
Motor	
Model	Azure Dynamics AC55
Current Draw Limit [A]	175
Regenerative Braking Ratio [-]	0.30
Battery	
Model	CALB 100 Ah
Series Strings	104
Parallel Strings	1
Nominal Cell Voltage [V]	3.2
Cell Capacity [Ah]	100
Cell Impedance [ohms]	0.06
Pack Configuration	104S1P
Pack Energy [kWh]	34
Battery Weight [kg]	343
Auxiliary Draw [watts]	600
Air Conditioner Draw [watts]	2,500
Heater Draw [watts]	2,000

The route consists of 20.9 miles with an average velocity of 10.3 mph, top speed of 47 mph, and 1087 meters of total elevation change. Table 9 provides the powertrain and physical design specifications required for input into the model. As an electric delivery vehicle with year round operating requirements, the effects of payload profiles, HVAC power draws, and battery temperature performance are of particular interest to the authors. The use of the simulation tool allows study of each parameter relatively

quickly, developing expected performance metrics (Figure 15) and trends while reducing the effects of range anxiety.

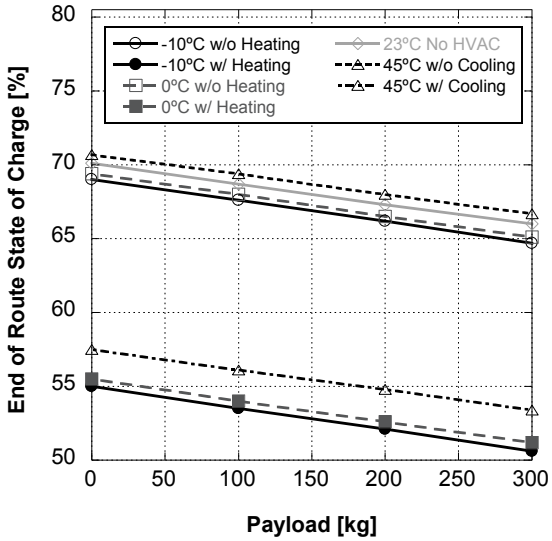

Figure 15: 1997 GMC Jimmy simulation results with varying average battery temperature, payload, and HVAC effects.

The resulting simulations indicate that the GMC will have no trouble completing the route under any of the conditions simulated and will likely be able to complete two days of delivery cycles before requiring a recharge. In addition, the library expects payloads to be much lighter than the highest conditions presented here that only result in about a 5% loss of SOC. As anticipated, the HVAC loads will have a significant effect on battery pack performance (~15% SOC), and further optimization of these systems would likely show more improvement than efforts to reduce the total vehicle weight. The use of CALB cells aids in the temperature performance of the vehicle and should provide KU Libraries with confidence when operating the vehicle during the winter months.

5. Conclusion

Newton's Second of Motion provides the foundation of an electric drive model. Using advanced vehicle dynamics and battery modeling, the model incorporates innovative methods to simulate vehicle range performance while requiring a minimal data set. The model is capable of simulating vehicle performance using traditional methods, as well as the proposed more sophisticated models. Both models and the simulation as a whole were validated using data collected from a student built research vehicle under real world driving conditions. The simulation demonstrates increased accuracy for the advanced rolling resistance, drag force, and battery models.

After creation and once properly set up, the model allows simulation of multiple vehicle parameters in a relatively short timeframe. This allows future researchers to use the tool to run expanded parametric studies, as well as in the vehicle design process when studying powertrain, vehicle design, and accessory draw effects.

Acknowledgements

This work was supported by Smith Electric Vehicles and the University of Kansas Transportation Research Institute [grant number IND 0066912].

References

1. Faiz, A., C.S. Weaver, and M.P. Walsh, *Air pollution from motor vehicles: standards and technologies for controlling emissions* 1996: World Bank Publications.
2. Pearre, N.S., et al., *Electric vehicles: How much range is required for a day's driving?* Transportation Research Part C: Emerging Technologies, 2011.
3. Larminie, J., J. Lowry, and I. NetLibrary, *Electric vehicle technology explained* 2003: Wiley Online Library.
4. Butler, K.L., M. Ehsani, and P. Kamath, *A Matlab-based modeling and simulation package for electric and hybrid electric vehicle design.* Vehicular Technology, IEEE Transactions on, 1999. **48**(6): p. 1770-1778.
5. Markel, T., et al., *ADVISOR: a systems analysis tool for advanced vehicle modeling.* Journal of power sources, 2002. **110**(2): p. 255-266.
6. Husain, I. and M.S. Islam, *Design, modeling and simulation of an electric vehicle system.* 1999.
7. He, X. and J.W. Hodgson, *Modeling and simulation for hybrid electric vehicles. I. Modeling.* Intelligent Transportation Systems, IEEE Transactions on, 2002. **3**(4): p. 235-243.
8. Rizzoni, G., L. Guzzella, and B.M. Baumann, *Unified modeling of hybrid electric vehicle drivetrains.* Mechatronics, IEEE/ASME Transactions on, 1999. **4**(3): p. 246-257.
9. Fox, R.W., A.T. McDonald, and P.J. Pritchard, *Introduction to fluid mechanics*. Vol. 7. 1985: John Wiley & Sons New York.
10. Bosch, R., *Bosch Automotive Handbook* 8th ed 2011: SAE International.
11. Donley, M.G., T.C. Lim, and G.C. Steyer, *Dynamic analysis of automotive gearing systems*, 1992, Society of Automotive Engineers, 400 Commonwealth Dr, Warrendale, PA, 15096, USA.
12. Schulz, M., *Circulating mechanical power in a power-split hybrid electric vehicle transmission.* Proceedings of the Institution of Mechanical Engineers, Part D: Journal of Automobile Engineering, 2004. **218**(12): p. 1419-1425.
13. Miller, J.M., *Hybrid electric vehicle propulsion system architectures of the e-CVT type.* Power Electronics, IEEE Transactions on, 2006. **21**(3): p. 756-767.
14. Powell, B., K. Bailey, and S. Cikanek, *Dynamic modeling and control of hybrid electric vehicle powertrain systems.* Control Systems Magazine, IEEE, 1998. **18**(5): p. 17-33.
15. Hori, Y., Y. Toyoda, and Y. Tsuruoka, *Traction control of electric vehicle: Basic experimental results using the test EV "UOT Electric March".* Industry Applications, IEEE Transactions on, 1998. **34**(5): p. 1131-1138.
16. Gao, Y. and M. Ehsani, *Electronic braking system of EV and HEV-integration of regenerative braking, automatic braking force control and ABS.* SAE Technical Paper, 2001.
17. Gao, Y., L. Chen, and M. Ehsani, *Investigation of the Effectiveness of Regenerative Braking for EV and HEV.* SAE Technical Paper, 1999.
18. Barras, B., et al., *Electric Vehicle Conversion*, 2011, Southern Illinois University Carbondale.
19. Schechter, M.M., *Regenerative Compression Braking- A Low-Cost Alternative to Electric Hybrids.* SAE transactions, 2000. **109**(3): p. 1192-1203.

20. Gao, H., Y. Gao, and M. Ehsani. *A neural network based SRM drive control strategy for regenerative braking in EV and HEV*. in *Electric Machines and Drives Conference*. 2001. IEEE International.
21. Bailey, K. and B. Powell. *A hybrid electric vehicle powertrain dynamic model*. 1995. IEEE.
22. Phillips, A.M., M. Jankovic, and K.E. Bailey. *Vehicle system controller design for a hybrid electric vehicle*. 2000. IEEE.
23. Rahman, K.M., et al., *Advantages of switched reluctance motor applications to EV and HEV: design and control issues.* Industry Applications, IEEE Transactions on, 2000. **36**(1): p. 111-121.
24. Morrow, K., D. Karner, and J. Francfort, *Plug-in hybrid electric vehicle charging infrastructure review.* US Departent of Energy-Vehicle Technologies Program, 2008.
25. Taylor, J., et al. *Evaluation of the impact of plug-in electric vehicle loading on distribution system operations*. 2009. IEEE International.
26. Lam, L. and R. Louey, *Development of ultra-battery for hybrid-electric vehicle applications.* Journal of power sources, 2006. **158**(2): p. 1140-1148.
27. Dhameja, S., *Electric vehicle battery systems* 2001: Newnes.
28. Buchmann, I., *Battery university*, 2003, July.
29. Depcik, C. and D.N. Assanis, *Graphical user interfaces in an engineering educational environment.* Computer Applications in Engineering Education, 2005. **13**(1): p. 48-59.
30. Chan, C. and K. Chau, *Modern electric vehicle technology*. Vol. 47. 2001: Oxford University Press, USA.
31. Cao, J.T., et al., *A study of electric vehicle suspension control system based on an improved half-vehicle model.* International Journal of Automation and Computing, 2007. **4**(3): p. 236-242.
32. Moaveni, S. and I. Sharma, *Engineering Fundamentals: An Introduction to Engineering: SI Edition* 2011: Thomson Engineering.
33. GIMP, G., *Image Manipulation Program*, 2004.
34. *Azure Dynamics. AC90 Motor with DMOC645 Controller*. Force Drive Electric Drive Solutions 2010; Available from: http://www.azuredynamics.com/products/force-drive/documents/AC90_DMOC645ProductSheet.pdf.
35. Jones, R.B., *TechDig*, 1998.
36. *Edison Power. SLPB (Superior Lithium Polymer Battery) Technical Specification*. Technical Specification 2009; A1:[Available from: http://edisonpower.co.jp/product/pdf/Tech_spec_SLPB96255255_60Ah_A1.pdf.
37. Andrea, D. *Tips for pouch cells*. 2012; Available from: http://liionbms.com/php/pouch_tips.php.
38. *Discover Energy EV31A-A*. EV Traction Dry Cell Industrial Battery 2012.

CHAPTER 5: Creating a Graphical User Interface for Performing Vehicle Route Simulations Using MATLAB

Austin Hausmann and Christopher Depcik

Department of Mechanical Engineering - University of Kansas, Lawrence, Kansas (United States)

Abstract

While computational code in its base language format proves useful for developing and editing the functionality of a model, its usage by individuals unfamiliar with the code along with repeated running by the developer can prove time consuming and inelegant. The use of a graphical user interface (GUI) provides a means for simplifying the underlying code and improving the overall accessibility of a program. This chapter covers the advantages of using MATLAB's GUI *Development Editor* in order to create a standalone GUI, as well as many of the common topics associated with building GUIs in MATLAB. In particular, the following sections present a complete GUI incorporating the efforts of the previous three chapters along with instructions for usage. Discussion includes multiple avenues for data analysis within the GUI, as well as the ability to export the data created from the simulation.

Words: 128

1. Introduction

MATLAB has proven to be a useful software and coding language for rapid code development along with implementation of mathematical and physical modeling [1]. However, editing raw code can prove to be difficult without a low-level understanding of the architecture of the code regardless of the software language. This effort proves even more difficult when magnified by the differences between coding styles of multiple

authors. For instance, it can be difficult to understand what an author is attempting to accomplish within a certain script if one does not understand the methodology behind the routine.

In order to overcome these and other difficulties, graphical user interfaces (GUI) are often used to provide a user with the ability to control various parameters and variables within a code through the use of easy to understand buttons, sliders, and various other controls [2]. For example, the dynamic vehicle model from Chapter 4 consists of thousands of lines of MATLAB code. Users with limited exposure to vehicular modeling or limited experience with MATAB may have difficulty navigating the code in order to produce desired results. Since the author's model is an educational and research tool for students and professors at the University of Kansas, ease of use is a necessity. As a result, development of a GUI is highly desirable.

2. Creating graphical user interfaces in MATLAB

As an aid to the GUI development process, MATLAB provides the *GUI Development Environment* (GUIDE). GUIDE offers an interactive environment for designing, creating, formatting, and programming a GUI from scratch using MATLAB [3]. It is possible to write a GUI programmatically using only the MATLAB command window; however, the use of the GUIDE can save a significant amount of time by automatically generating code in order to outline the framework of the GUI. Depending on the skill of the user and scale of the GUI, the creation procedure can be a complex and time-consuming process. The following work will outline this process briefly; however, this will not be a stand-alone document for GUI creation. There are many

other resources that accomplish this tactic [2, 4, 5]. Moreover, the Mathworks website (*www.mathworks.com*) and MATLAB help files are useful for this task.

To use GUIDE, one starts the application by typing "*guide*" into the MATLAB command window and pressing enter. This executes the *GUIDE Quick Start* environment allowing the user to create a new GUI or open an existing GUI. The first step in creating a GUI is laying out the front-end window. This window acts as the main hub for control and display of the underlying MATALB script. Inputs are available through a variety of controls:

- Push buttons
- Sliders
- Radio buttons
- Check boxes
- Editable text fields
- List boxes
- Pop-up menus

Push buttons allow for initialization of an action when clicked. This can be as simple as increasing an integer value of a single variable or running an entire set of simulations. Sliders establish a numeric value without requiring the user to type in the value. Easy adjustment of the slider allows the user to change the number at a set iteration. The user moves the slider by either clicking and dragging or clicking on the arrows at each end of the slider. Check boxes and radio buttons typically define the state of a variable. In particular, check boxes allow for independent choices, as opposed to radio buttons that include mutually exclusive variables. In both cases, additional programming allows

these forms to behave outside of their originally intended uses. Editable text fields gather a variety of custom inputs from the user, such as strings or numbers for use within the code or generating outputs. While their appearances are vastly different, list boxes and pop-up menus are nearly identical with the exception that list boxes allow for multiple selections and pop-up menus only allow for a singular selection.

The various output parameters include both static text fields and axes. Static text fields display information to user in text format and do not allow editing by the user. They are merely a means of displaying information. Axes provide information to the user graphically, often in the form of plots or figures.

Equipped with an understanding of what is available, the developer can create a sketch outlining the overall design of the GUI. This requires forethought in order to determine the needs for each window in the entire software set. This process helps envision the requirements of the GUI along with how the end user will accomplish it before attempting to create an electronic version. Any variables that are available for editing within the main code should be editable within the GUI. After deciding the design for the GUI, the developer should add all of the inputs, outputs, figures to a MATLAB *.fig* file. The architecture of GUIDE allows accomplishment of this via a drag-and-drop methodology. This includes resizing fields, buttons, and figures. Editing the default values and states for all fields, as well as available fields and selections for menus is available by right clicking on the field and selecting the *Property Inspector* menu. Moreover, it is advisable to edit the name of the field through the "*Tag"* field in the *Property Inspector* menu. The "*Tag"* will appear in the code generated by the

GUIDE and naming the variables to correspond with the functionality on the figure file will save time when associating the variables with their fields in the GUI front end.

After completing the figure file, the developer should save the resulting GUI and execute it in order to determine any initial issues. The first time this is done, GUIDE will generate the necessary code in order to incorporate needed algorithms while applying the underlying code. The code saves as a standard *.m* MATLAB script file while the figure has the same name as *.fig* for future revising.

While GUIDE will produce the framework for GUI behavior, the programmer must properly place and call the respective numerical algorithms. In order to implement the newly created GUI with the appropriate MATLAB scripts, it is necessary to have a thorough understanding of callbacks and handles. Callbacks work as functions that tie the GUI figure to the MATLAB script. These functions typically execute based on specific tasks (e.g., button pushes, changing values, etc.). The execution of a callback is the equivalent of calling a separate function file (or sub-function) within a MATLAB script. Their usage occurs for a variety of reasons including button pushes, value changes, and any other forms of interaction. Handles identify certain parameters with their values and commands associated within the fields in the GUI figure. The combination of callbacks and handles allows various fields to communicate with each other through interaction by the user. When saving the figure file from GUIDE, the underlying framework creates callbacks for each of the fields in the figure. This is where GUIDE can save a significant amount of time over coding a GUI programmatically, which would require coding all of the callbacks individually.

In order to associate the values in the GUI fields with the necessary algorithms requires use of the *get* and *set* commands. As their names imply, the "*get"* command retrieves values in the GUI and saves them to variable name and "*set"* sends variables from the script file to a field within the GUI.

3. A Graphical User Interface for the Vehicle Dynamics Model

Using the basic technique described above, Figure 1 presents a constructed GUI for the vehicle dynamics model of Chapter 4.

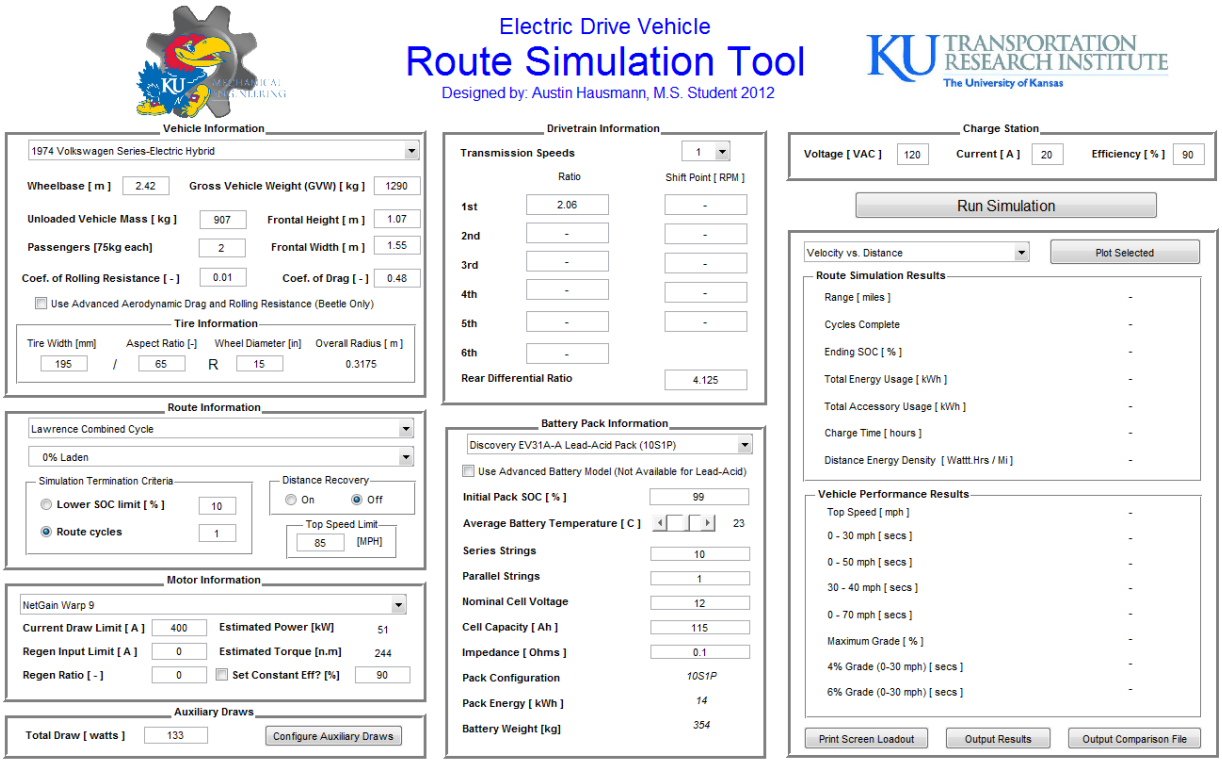

Figure 1: Graphical user interface for vehicle dynamics model.

The main GUI window is broken down into eight unique sections presented in the rest of this chapter:

- Vehicle Information
- Route Information

- Motor Information
- Auxiliary Draws
- Drive Train Information
- Battery Pack Information
- Charge State
- Results

Moreover, there are a number of buttons incorporated in order to run simulations and export a wide variety of data.

3.1 Vehicle information

The *Vehicle Information* section contains details related to the physical specifications of the vehicle (Figure 2).

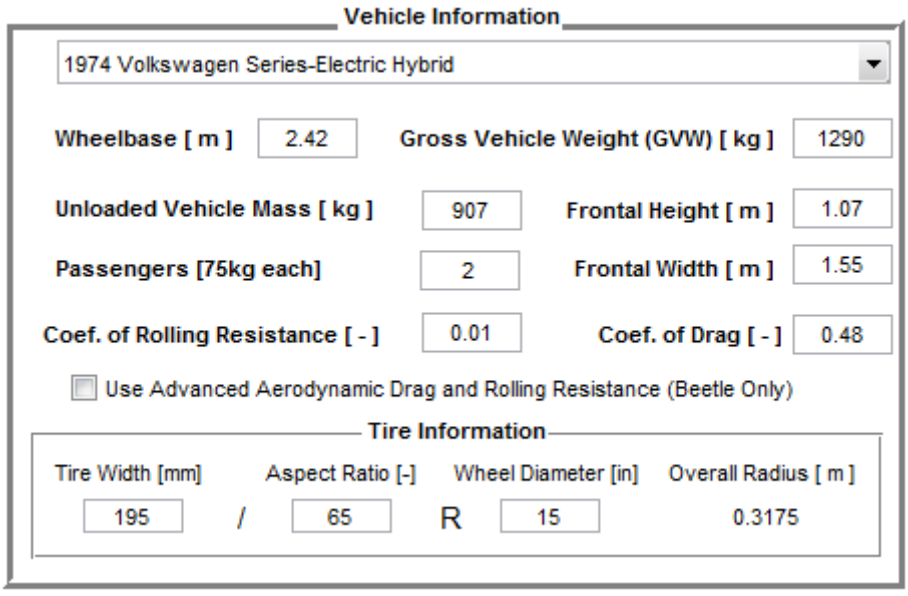

Figure 2: Vehicle information section.

- The *Vehicle Selection* dropdown menu provides the user with the ability to select from default configurations loaded into the code. Selecting the appropriate

vehicle will update all of the other fields in the GUI to their appropriate values for the selected vehicle. In addition, the dropdown menu provides the user with the ability to select a custom vehicle. This option does not apply any changes to the default values. It is possible to load virtually any vehicle design using this option; however, configurations that result from this option might not be physically possible or feasible.

- The *Vehicle Wheelbase* field is for informational purposes only. While this value can have an effect on the vehicle mass in real world configurations, it does not factor into the mass calculations within the model. This method gives the user additional flexibility when designing new vehicle configurations and allows for easier vehicle identification in future vehicle designs.
- The *Gross Vehicle Weight Rating* field adjusts for vehicle loading in the *Route Information* section covered later. This value is the maximum allowable total mass of the vehicle when loaded.
- The *Unloaded Vehicle Mass* field is the mass of the vehicle minus any cargo load, passengers, and battery weight. The total battery mass is later added to the total mass of the vehicle based on the specific weight of the battery pack configuration as defined in Chapter 4. Not calculating the battery weight in this section allows the model to handle the computation enabling the user to simulate multiple battery configurations quickly for the same vehicle configuration without manually calculating the battery weight before each simulation.
- The *Coefficient of Drag* field is the common value used to calculate the aerodynamic drag force on the vehicle as defined in Chapters 2 and 4.

Computational the frontal area uses both the *Frontal Height* and *Frontal Width* fields.

- The *Coefficient of Rolling Resistance* is the traditional value as presented in Chapter 2.
- Implementation of the advanced coastdown model described in Chapter 2 occurs by selecting the *Advanced Aerodynamic Drag and Rolling Resistance* option. This option is currently only available for the 1974 Volkswagen Super Beetle series hybrid.
- The *Tire Information* subsection defines the overall rolling radius of the tire. Automatic calculation of the *Overall Radius* field happens anytime the user changes the *Tire Width*, *Aspect Ratio*, or *Wheel Diameter*.

3.2 Route Information

The *Route Information* section specifies the driving cycle for the simulation. This section consists of the vehicle velocity, elevation, and loading profiles along with the simulation termination criteria, distance recovery option, and top speed limit of the route (Figure 3). The GUI allows for implementation of virtually any route profile using a minimal data set. The input files must contain velocity data [mph] in the first column and elevation data [m] in the second column input at a one-hertz rate. The file format can be in the following file extensions: *.xlsx*, *.xls*, and *.csv*. It may also be useful to compare the simulation data to actual measured data from the route. This feature is available when selecting a custom input file. Figure 4 presents the GUI for the option to load comparison data after selecting the file path.

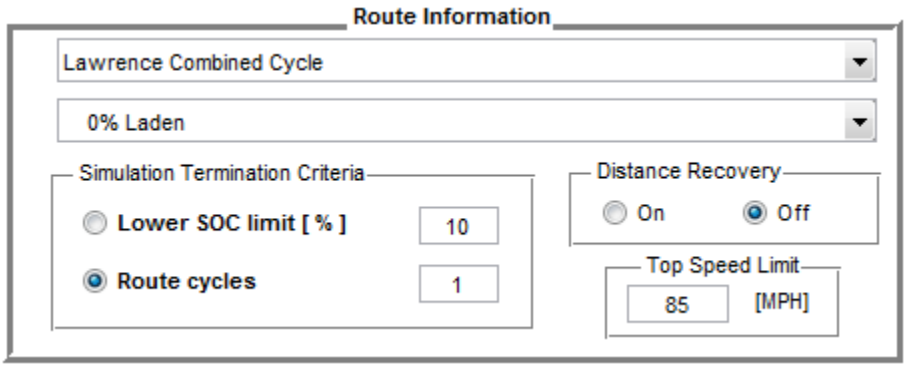

Figure 3: GUI route information section.

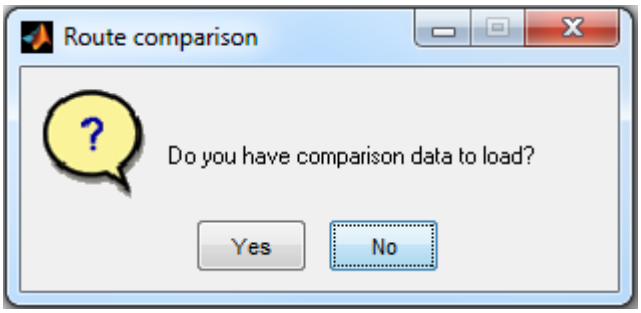

Figure 4: Comparison data load prompt.

0	310	0	99	322	-6	-1.93	0.001
0	310	0	99	322	-6	-1.93	0.001
0	310	0	99	322	-6	-1.93	0.002
0	310	0	99	322	-6	-1.93	0.002
0	310	0	99	322	-6	-1.93	0.003
0	310	0	99	322	-6	-1.93	0.003
1	310	0	99	322	-6	-1.93	0.004
2	310	0	99	322	-15	-4.83	0.005
4	310	0	99	320	-37	-11.84	0.008
5	310	0	99	320	-48	-15.36	0.013
6	310	0.01	99	320	-61	-19.52	0.018
7	310	0.01	99	320	-44	-14.08	0.022

Figure 5: Sample comparison data input file.

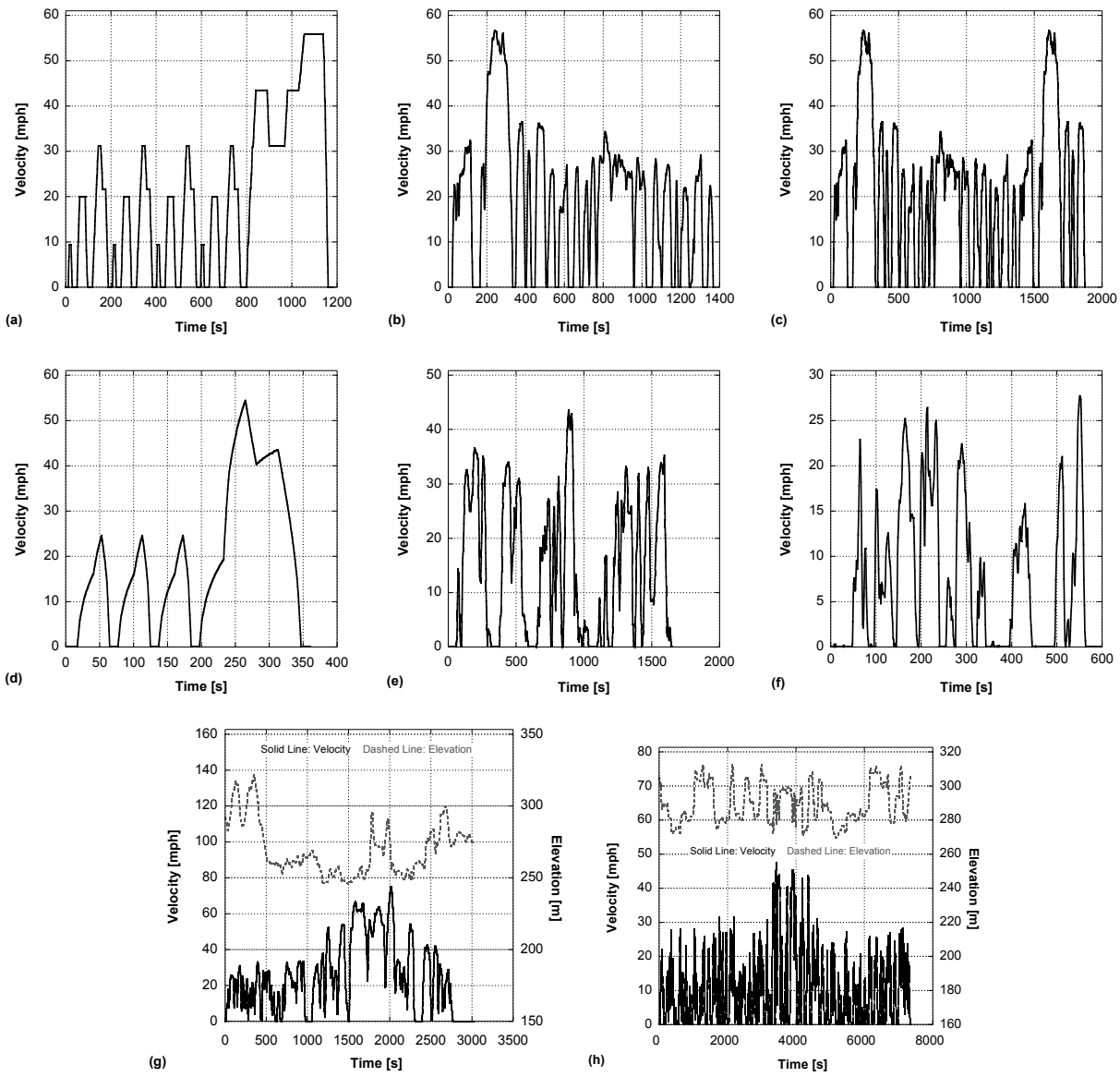

Figure 6: Available drive cycles a) NEDCL, b) UDDS, c) FTP-75, d) SFUDS, e) CSC, f) NYCC, g) Lawrence Combined Route, and h) KU Libraries Daily Delivery Route.

If utilizing comparison data, the file format should be the same as loading a custom profile with the addition of six new columns. The columns will now be in the following order:

Speed [mph] / Elevation [m] / Distance [mi] / SOC [%] / Voltage [V] / Current [A] / Power [kw] / Energy [kWh]

For example, the first few rows should look similar to Figure 5. However, all data from the vehicle may not be available or of interest. If this is the case, the user may fill the columns with any arbitrary values (for instance filling the voltage column with the nominal pack voltage). It is important that all columns contain data and be of the same length.

In addition, the simulation tool contains eight selectable route profiles. These profiles consist of six standard driving cycles and two real world driving cycles developed through data collection in University of Kansas vehicles (Figure 6). The standardized routes are chosen from the most widely used cycles available from the Environmental Protection Agency (EPA) [6]:

- NEDCL (New-European Driving Cycle)
- UDDS (Urban Dynamometer Driving Schedule)
- FTP75(Federal Urban Driving Scheule)
- SFUDS (Simplified Federal Urban Driving Schedule)
- CSC (City Suburban Cycle)
- NYCC (New York City Cycle)

A combined route consisting of both urban and highway driving around Lawrence, Kansas offers a standard, relatively repeatable driving cycle for comparison within the model. Development of the Lawrence Combined Cycle provides a local route around 20 miles that utilizes an equal distance split between urban and rural driving. Efforts in driving the route seven times while collecting data resulted in a median velocity profile

implemented into the numerical tool. Implementation of an option for the University of Kansas Library Daily Usage route allows for determination of the feasibility of designing an electric vehicle for delivery purposes. This included collecting over two weeks of data with the results indicating a highly repeatable route. The specific route chosen is the route with the best average GPS signal since it resulted in the cleanest data set. Table 1 indicates a summary of all the default routes in the GUI.

Table 1: Route statistics for default simulation routes.

Route	Distance [mi]	Average Velocity [mph]	Total Elevation Change [m]	% of Distance over 40 MPH
NEDCL	6.84	20.0	-	19.1 %
UDDS	7.50	19.6	-	8.1 %
FTP75	11.0	21.2	-	11.8 %
SFUDS	1.92	19.2	-	20.8 %
CSC	6.68	14.5	-	2.2 %
NYCC	1.18	7.1	-	0 %
Lawrence Combined	21.2	25.3	721.8	23.3 %
KU Libraries	20.9	10.3	1,087	2.7 %

The other components in this GUI include:

- A second dropdown menu in the *Vehicle Route* section determines the load profile for the entire route. Chapter 4 outlines the available selections and calculation methods.
- The *Simulation Termination* selection governs the stopping condition for the simulation. Two options are available: State of Charge limit and number of cycles limit.
    - *State of Charge Limit* – Utilization of this option will allow the simulation to run the selected cycle until a predetermined limit. This option determines the absolute range of a vehicle.

- *Route Cycles Limit* – Selection of this option will allow the simulation to run the selected cycle a predetermined finite number of times. This option will terminate the simulation at 10% State of Charge even if the model has yet to reach the set number of cycles.

- The *Distance Recovery Option* ensures that the distance of the input file and simulation match at the end of the simulation. For instance, if the current limit of the vehicle prevents the simulation from maintaining the same speed as the input file, there will be a difference between the two distances. Chapter 4 describes this algorithm in more detail.
- The *Top Speed Limit* function limits the top speed of the input route. If the limit is set higher than any points in the input file, the route will run according to the input file. If the limit is set lower, these points will be set to the limit.

3.3 Motor Information

The *Motor Information* section defines the parameters required for motor calculations. This includes input and output current limits defined by the motor controller (Figure 7).

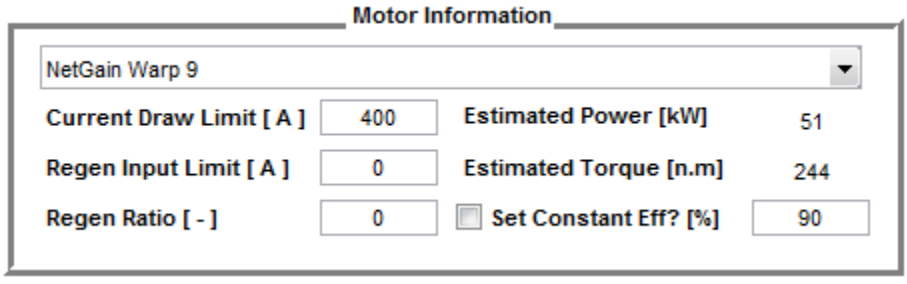

Figure 7: GUI motor information section.

- The *Current Draw* field specifies the maximum allowable current draw from the battery pack. The model uses this value as a hard cutoff, as opposed to

progressively increasing the current limit after a certain amount of time. Theoretically, there is no limit to the amount of time the model allows the battery pack to draw this value. In addition, this value includes the accessory draw current. For example, if the current draw limit is set to 250A and the accessories are drawing 10A, only 240A is available for motor current.

- The *Current Input* field inputs the maximum allowable current allowed for regenerative braking. This is also a hard cutoff value and is the maximum value after accounting for all associated drivetrain, resistances, and cell impedance efficiencies.
- The *Regen Ratio* field provides the percentage of this braking force available for regenerative braking. Chapter 4 outlines the method for calculating this regenerative braking energy value.
- Two motor maps are included for selection in the *Motor Selection* field :
    - NetGain Warp 9
    - Azure Dynamics AC55

These are the motors associated with the 1974 Volkswagen Super Beetle series hybrid and the 1997 GMC Jimmy battery electric vehicle, respectively. The selection from this drop down menu calls the respective motor efficiency map, as well as the necessary torque curve.

- The *Estimated Power* and *Estimated Torque* fields automatically calculate the maximum available motor performance based on the values currently configured in the GUI.

- The *Constant Efficiency* field allows the user to set a false and simplistic motor efficiency value as opposed to using an actual map. This allows the user to study the effects of motor efficiency on vehicle performance.

3.4 Auxiliary Draws

The *Auxiliary Draws* field defines all of the auxiliary components of the vehicle (Figure 8).

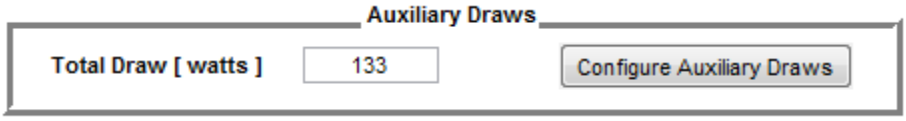

Figure 8: GUI auxiliary draws section.

- The *Total Draw* field provides a manual specification of the total accessory draw at each step of the vehicle route.
- Alternatively, using the *Configure Auxiliary Draws* routine, the GUI can calculate this value automatically based on the various component power draw and operational time as defined in Chapter 4 (Figure 9).

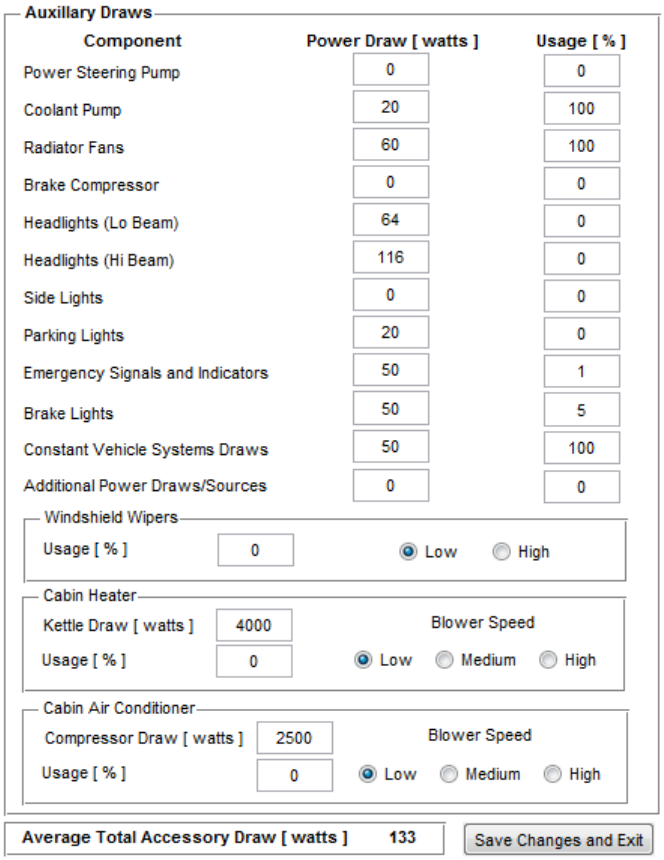

Figure 9: GUI individual auxiliary draw menu.

Each time the user edits any of the individual power draws or duty cycle values, the GUI will automatically calculate the total power draw for the route as outlined in Chapter 4. Once the user is finished, clicking *Save Changes and Exit* will save the work and update the value on the front GUI window. Each time the user saves the values, they are stored in a state matrix available for recall. Reopening the window will recall all of the previously set values. After closing the entire GUI, this state matrix reverts to the default values. If the user wishes to discard the changes, closing the window will return the values to their previous state.

3.5 Drivetrain Information

The *Drivetrain Information* section contains the parameters required for power transmission between the motor and the rear wheels. This includes the reduction/transmission gears (if equipped), number of speeds, and rear differential (Figure 10). Selecting a single-speed gear reduction prevents input of shift points and presents only one gear ratio for the transmission selection. The shift points indicated are the upper level for the transmission gear. This value represents the associated rotational motor velocity at which the transmission will shift into the next highest gear (if available). In the event of deceleration, the transmission model will follow the algorithm presented in Chapter 4. The *Rear Differential Ratio* field provides the size of gear reduction for the rear differential.

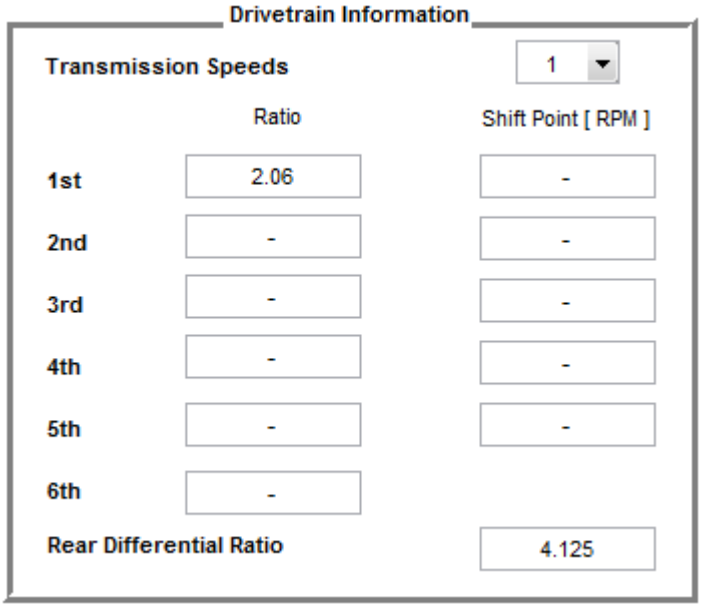

Figure 10: GUI drivetrain information.

3.6 Battery Information

The *Battery Information* section contains all the inputs required for modeling the performance of the battery pack (Figure 11).

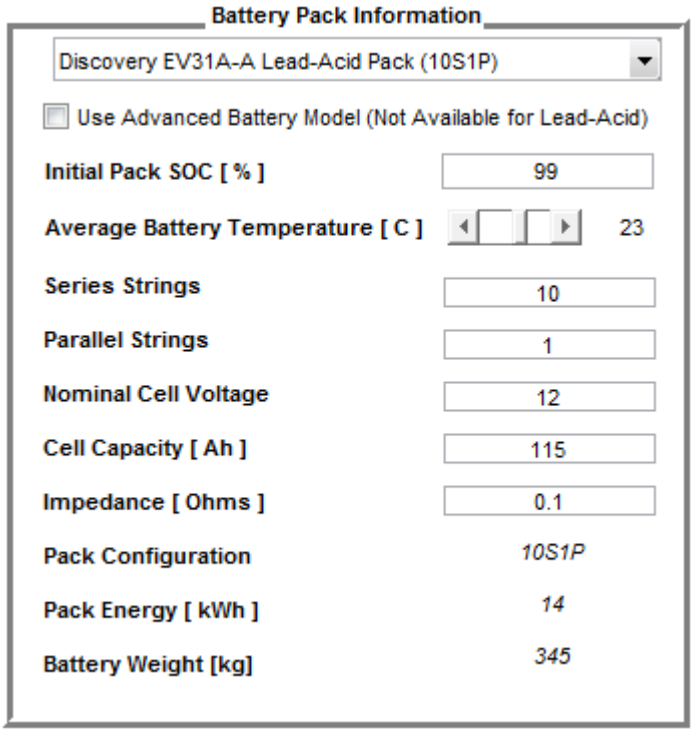

Figure 11: GUI battery pack information section.

This GUI contains the following items:

- The *battery chemistry selection* drop down menu includes six selections:
    - Discover EV31A-A Lead-Acid Pack (10S1P)
    - Kokam SLPB255255 LiPo Pack (38S2)
    - CALB 100Ah LiFe Pack (104S1P)
    - Generalized Lead-Acid Pack
    - Generalized LiPo Pack
    - Generalized LiFe Pack

This dropdown menu allows the GUI to call the correct battery draw map, select the default values (if necessary) while determining the specific energy of the chosen batteries necessary for computing total battery pack weight. Chapter 4 describes all of these procedures.

- Implementation of the advanced battery model described in Chapter 3 occurs by selecting the *Used Advanced Battery Model* option. It is worth noting that this option is only available for the lithium-based cells, as it does not apply to lead-acid batteries.
- The *Initial Pack SOC* field allows the user to begin the simulation of a battery pack at any initial State of Charge.
- The *Series and Parallel Strings* fields define the configuration of the battery pack. The *Series Strings* field represents the number of cells wired in series in each parallel string. The *Parallel Strings* field describes the number of these strings in parallel. In the event that these values are changed, the *Pack Configuration* field will update to indicate the format of the battery pack.
- The *Nominal Cell Voltage* field provides the total voltage of a single cell. This value should coincide with the number of cells input in the *Series Strings* field.
- The *Cell Capacity* field indicates the capacity of the cell defined as the capacity of each series string. Typically, one uses the 20-hr capacity when the cell specification sheet indicates more than one capacity.
- Both the *Pack Energy* and *Battery Weight* fields are calculated automatically each time any of the battery menu parameters are changed.

3.7 Charging

The *Charge Station* field defines the three parameters associated with charge time calculation presented in Chapter 4 (Figure 12).

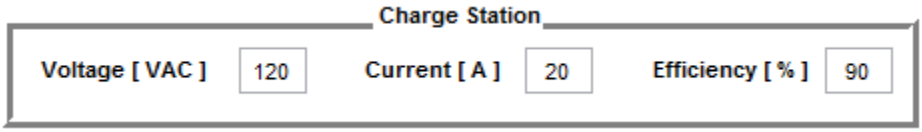

Figure 12: GUI charge station section.

- The *Charger Voltage* field defines the VAC line voltage supplied to the charger.
- The *Charger Current* field is the alternating current applied at the charger.
- The *Charger Efficiency* field estimates the charger efficiency and line efficiency.

3.8 Running Simulations

Once all criteria are input, the user can start the simulation by pressing the *Run Simulation* button. After beginning, a "*Simulation Running..*" dialog box will appear with a progress bar indicating that the simulation is in fact progressing (Figure 13). This progress bar is a function of the actual time steps during the route. The bar will not progress during the variable initiation phase (at the beginning of the simulation) and throughout the acceleration model calculation (at the end of the simulation). After completion, a "*Simulation Complete"* dialog box will appear. In addition, this dialog box will indicate the amount of time the simulation ran and the user can close this box by pressing the "*OK*" button.

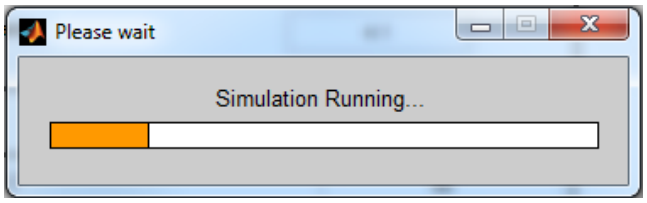

Figure 13: GUI simulation running alert.

3.9 Results

After completing the simulation, the *Route Simulation Results* and *Vehicle Performance Results* GUIs will populate with data from the simulation (Figure 14). The program allows for plotting of many of the calculated variables during the simulation. The dropdown menu provides the user with those typically used for vehicle performance:

- Velocity vs. Distance
- SOC vs. Time
- SOC vs. Distance
- Energy Used vs. Time
- Energy Used vs. Distance
- Power vs. Time
- Power vs. Distance
- Elevation vs. Time
- Elevation vs. Distance
- Pack Voltage vs. Time
- Pack Current vs. Time
- Motor Efficiency vs. Time
- Motor Torque vs. Time
- Motor RPM vs. Time
- Motor Torque/Speed Profile
- Individual Efficiency Losses vs. Time
- Total Efficiency Loss vs. Time
- Efficiency Losses Pie Chart
- Transmission Gear vs. Time
- Acceleration Profiles
- Velocity and Elevation
- Compare Against Input File

Selection of these plots occurs using the drop down menu with subsequent graphing using the *"Plot"* button. Plotting will only be available after a completed simulation and will only display the most recent results. When running a new simulation, the architecture of the software suspends plotting until generation of new results. If simulation comparison data is present, the "*Compare Against Input File*" option will

provide a comparison plot. If no comparison data is available, this feature will not be functional.

Using the "*Print Screen Loadout*" and "*Output Results*" buttons provides more flexibility for data analysis beyond that available within the GUI. The "*Print Screen Loadout*" button will capture a picture of the current GUI window with all variables indicated. This is useful for keeping a visual log of simulations performed. The *Output Results* button will output the results and variable data into a standardized Excel file. Naming of both of these files includes the current time and date in the following format: YYYYMMDD_HHMMSS. For example, 20120701_220846 corresponds to July 1, 2012 at 10:08:46 pm. Storage of both of these files occurs within the working directory of the simulation tool. If route comparison data is available, this data will also be output in a separate worksheet in the Excel file. The data save and export feature can occasionally take a significant amount of time; therefore, a file write progress bar is available to monitor the progress.

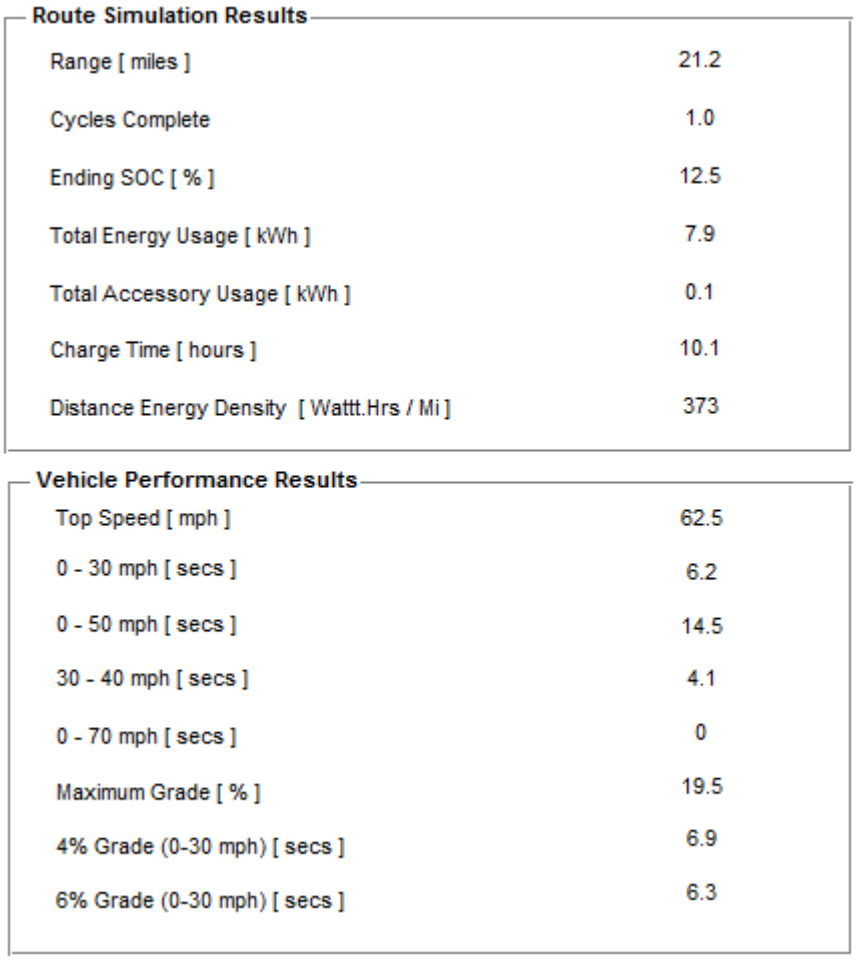

Figure 14: GUI simulation results section.

The "*Output Comparison File*" button will create a file in the exact format needed for comparison data in the file input section. This effectively allows running simulations back to back for assessment between options. For example, comparing configuration A to configuration B involves:

- Run A
- Output comparison file for A
- Load comparison file for A
- Make changes to loadout to represent B (for example change final drive ratio)
- Run simulation

- Compare runs

The input file will use the velocity and elevation profiles from A to run B. For example to perform current limiting studies, run the higher current limit configurations first. If the lower current configurations occur first, the resulting route will be easier to complete and the subsequent higher current values are unnecessary for route completion. The same principle applies to other limiting factors as well (e.g. RPM, mass, voltage, etc.).

4. Compiling a MATLAB GUI

While retaining the ability to edit the GUI script and customize the algorithms has its benefits, some users may not have access to MATLAB. In order to overcome this, MATLAB allows for compilation of the code into an executable format. One can then install this executable file on other computers similar to other software programs. MATLAB accomplishes this through the MATLAB *Compiler*.

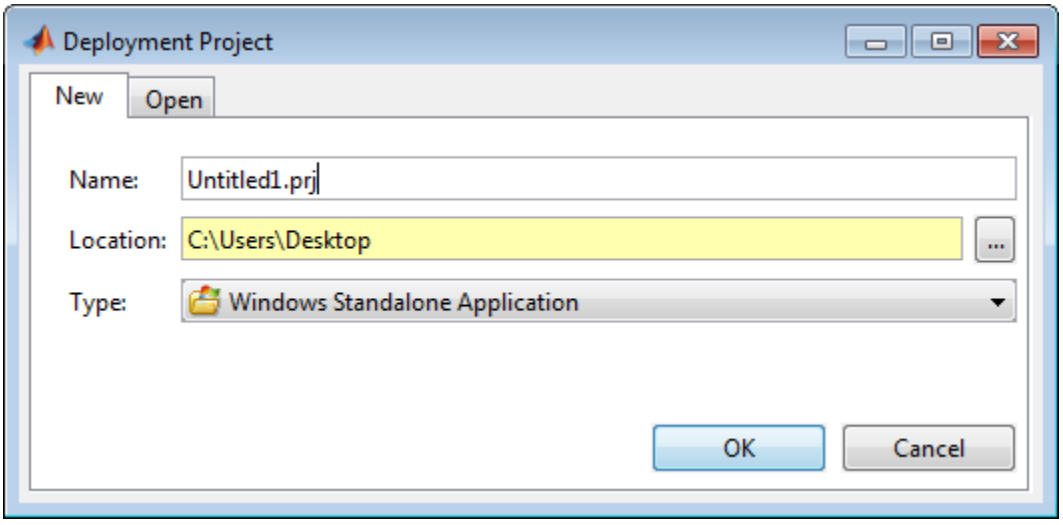

Figure 15: MATLAB Compiler opening menu.

To deploy a GUI using the MATLAB *Compiler*, the developer enters the "*deploytool*" command in the MATLAB command window that opens the GUI for the compiler (Figure 15). From this window, one can name the project, the storage location chosen, and the type of application chosen. It is important to select the *Windows Standalone Application* option when intending to install the GUI on another Windows-based machine. The *Console Application* option allows for inclusion of a command window in the installed program.

After starting the compiler, the GUI will ask for the main file, as well as any supporting files. The main file should be the figure file associated with the main GUI window. Then, the developer needs to choose any other files required to run the program using the supporting files list. This includes all MATLAB codes, functions, and data files required by the main program. After selecting all files, the user picks the *Build Package* button in order to generate a package with all files encompassed. In order to ensure full functionality within a single executable, MATLAB provides an option for testing this package. All testing should occur at this level before the final compiling takes places. After approval of the package, the user should select the *Build Executable* option. Once selected, a prompt will appear with respect to choice of an option to embed the MATLAB *Compiler Runtime* (MCR). The MCR is required for an executable built in MATLAB to run on a computer without MATLAB installed. Previous experience indicates the developer should always add the MCR to the compiler package. After initiation, the compiler will generate a self-installing executable in the working directory presented as a single icon. When opened, extraction of the contents will commence and the Windows installation process for the GUI will initialize. It is

worth noting that code compiled using a 64-bit version of MATLAB will only run on a 64-bit version of Windows. Use of 32-bit version of MATLAB allows the resulting package to run on either version of Windows.

5. Conclusions

Although the use of MATLAB script files can aid in the development and flexibility of mathematical modeling, the use command line inputs and subsequent finding all of the necessary variables for changes can be difficult. The use of a graphical user interface provides a means for simplifying the underlying code and easing the overall usage of a program. While actually designing a useful GUI may be difficult, MATLAB has created the GUI *Development Editor* to aid in the implementation of the GUI.

Using GUIDE and the MATLAB *Compiler*, this chapter documents the development of a standalone console application useful for interfacing with the vehicle dynamics model described in the previous three chapters. This application breaks down each section of the model into individual sections with appropriately named variables while allowing customization of all of the frequently used variables. The display of the results to the user in text and graphical format along with the ability to export the entire dataset for analysis outside of the GUI aids in efficient post-processing of model results.

References

1. Depcik, C. and D.N. Assanis, *Graphical user interfaces in an engineering educational environment.* Computer Applications in Engineering Education, 2005. **13**(1): p. 48-59.
2. Marchand, P. and O.T. Holland, *Graphics and GUIs with MATLAB*2003: Chapman & Hall.
3. *Creating Graphical User Interfaces in MATLAB*. MATLAB GUI 2012; Available from: http://www.mathworks.com/discovery/matlab-gui.html.
4. Smith, S.T., *MATLAB: advanced GUI development*2006: Dog Ear Publishing.
5. *Matlab: Getting Started Guide*, 2011, Version.
6. *Dynamometer Driver's Aid*. 2010; Available from: http://www.epa.gov/nvfel/testing/dynamometer.htm#vehcycles.